

Christian Röthel

X-ray Diffraction of Organic Thin Films: Crystalline Texture in Uniplanar Systems

DISSERTATION

zur Erlangung des akademischen Grades
Doktor der technischen Wissenschaften

Doktoratsstudium der Technischen Wissenschaften
Technische Physik



TECHNISCHE UNIVERSITÄT GRAZ

Betreuer:

Ao.Univ.-Prof. Dipl.-Ing. Dr.techn. Roland Resel
Institut für Festkörperphysik
Technische Universität Graz

Graz, Oktober 2017

To my Friends
and Family

EIDESSTATTLICHE ERKLÄRUNG

Ich erkläre an Eides statt, dass ich die vorliegende Arbeit selbstständig verfasst, andere als die angegebenen Quellen/Hilfsmittel nicht benutzt, und die den benutzten Quellen wörtlich und inhaltlich entnommenen Stellen als solche kenntlich gemacht habe. Das in TUGRAZonline hochgeladene Textdokument ist mit der vorliegenden Dissertation identisch.

Datum

Unterschrift

Abstract

In this thesis, an approach to perform X-ray diffraction on weakly textured crystalline films is presented. Due to lack of a proper 2D powder statistics introduced by a weak azimuthal crystal texture, standard X-ray diffraction methods such as grazing incidence X-ray diffraction are not suitable to obtain complete reciprocal space maps. Hence, crystallographic and structural properties, which are crucial for technical applications, cannot be determined reliably. Also, methods applied for strongly textured crystalline films, such as the pole figure technique for biaxially aligned thin films, are rather time consuming and become quickly unfeasible if experimental time is limited. The approach developed in this thesis is split into two parts: the experimental data collection and the sample type specific data evaluation in reciprocal space. Firstly, it uses the advantage of fast X-ray area detectors to probe extensive regions of reciprocal space using a standard grazing incidence scattering geometry. Secondly, having transformed the recorded diffraction data into reciprocal space allows for convenient data evaluation based on the sample texture, i.e. pole figures, reciprocal space maps, powder plots. Thus, this method is applicable to weakly as well as strongly textured thin films. While standard pole figure measurements require specific measurements for each netplane, this approach allows for the calculation of pole figures for arbitrary netplane distances, making it possible to efficiently screen samples with unknown crystalline forms or to detect pseudo-polymorph formation. The aforementioned methods are applied in the study of various crystalline thin film samples showing different crystallographic properties. Firstly, X-ray pole figure measurements were used to study the epitaxial growth of biaxially aligned caffeine crystallites on single crystalline surfaces of sodium chloride, potassium chloride and muscovite mica. Secondly, weakly textured thin films containing mixed crystals of phenothiazine and iminostilbene were investigated using grazing incidence X-ray diffraction and allowed for the determination of a crystal lattice shift due to the intermixing of the molecules. Finally, a study on the directed growth of carbamazepine on iminostilbene using reconstructed pole figures is presented.

Kurzfassung

Diese Arbeit stellt eine Methode zur Messung von schwach texturierten kristallinen Filmen dar. Durch das Fehlen einer vollständigen 2D Pulverstatistik, verursacht durch die Präsenz einer schwachen azimutalen Textur der einzelnen Kristallite, sind Standardverfahren wie Röntgenbeugung unter streifenden Einfall oder Polfigurenmessungen, nur bedingt geeignet um solche Proben zu charakterisieren. Methoden zur Messung von biaxial ausgerichteten Proben könnten prinzipiell eingesetzt werden, sind jedoch aufgrund ihrer im Vergleich langen Messzeiten praktisch nur von limitierten Nutzen. Die Methode zur Messung solcher schwach texturierten Filme ist in zwei Abschnitte unterteilt. Der erste Teil besteht aus dem Einsatz von Röntgenflächendetektoren zur effizienten Messung des reziproken Raumes in einer herkömmlichen Messgeometrie wie sie für Röntgenbeugung unter schleifenden Einfall benutzt wird, jedoch erweitert um eine azimutale Drehung der Probe während der Messung. Der zweite Teil beschäftigt sich mit der Berechnung und Darstellung von Polfiguren und Reciprocal Space Maps aus den aufgenommenen Streubildern. Der allgemeine Ansatz der Messung erlaubt eine probenunabhängige Datenerfassung. Daher können unabhängig von der kristallinen Textur Proben mit demselben experimentellen Aufbau vermessen werden. Die texturspezifischen Charakteristika der einzelnen Proben werden erst während der Datenauswertung relevant. Ein wesentlicher Vorteil dieser Methode ist, dass Polfiguren für beliebige kristalline Netzebenen aus einer allgemeinen aufgenommenen Messreihe rekonstruiert werden können. Dies bedeutet, dass Proben mit unbekanntem kristallinen Phasen oder Pseudopolymorphie vermessen werden können, was mit herkömmlichen Polfiguren nur unter enormen Zeitaufwand möglich ist. Abschließend werden die vorgestellten Methoden an unterschiedlichen kristallinen Proben mit verschiedenen Eigenschaften demonstriert. Als erstes Beispiel dienen biaxial gewachsene Koffeinkristalle auf kristallinen Oberflächen von Natriumchlorid, Kaliumchlorid und Muskovit Mica, welche mit herkömmlichen Polfiguren vermessen wurden um das epitaktische Wachstum zu bestimmen.

Als zweites Beispiel werden schwach texturierte Filme bestehend aus Mischkristallen von Phenothiazine und Iminostilbene angeführt. Mit Hilfe von Röntgenbeugung unter schleifenden Einfall könnte eine Verschiebung der Gitterkonstanten aufgrund der Zusammensetzung der Mischkristalle nachgewiesen werden. Als letztes Beispiel ist das gerichtete Wachstum von Carbamazepine auf Iminostilbene angeführt. Mit Hilfe von rekonstruierten Polefiguren konnte die epitaktische Beziehung zwischen den beiden Kristalltypen ermittelt werden.

Acknowledgment

Firstly, I would like to thank my PhD advisor Roland Resel for his continuous support throughout the last years and for introducing me to Oliver Werzer, who gave me the opportunity to carry out my PhD as part of his FWF project. I would like to thank Oliver for guiding me through the experimental challenges I faced during my PhD and for always finding time to help me with my problems. His unbridled enthusiasm for science was absolutely inspiring. I also appreciated our countless discussions about our scientific work and many other fascinating topics.

My sincere thanks also go to Clemens Simbrunner from Johannes Kepler University Linz. Clemens provided us with intriguing samples for many years and shared his immense knowledge about pole figures and crystal growth with us on many occasions. I thank Ingo Salzmann for inviting me to join him for several synchrotron beamtimes at ESRF and BESSY, which have always been a pleasure.

One of the most fascinating parts of my PhD were the numerous experiments at synchrotron facilities all over Europe. While the opportunity to work at such facilities is already an absolutely brilliant experience from a scientific point of view, the most precious moments are probably the countless hours spent with my colleges and friends trying to unravel the great mysteries of nature during the night shifts i.e. aligning samples properly. I am looking back especially fondly to our stay at the DIAMOND light source, where we not only gained a considerable amount of scientific knowledge but also the infamous synchrotron pounds.

I would like to particularly thank Armin Moser for one of the most important remarks during my PhD, which inspired me to tackle the problem of reciprocal space transformation. I am sure, he is not even aware of how important this casual conversation has been for me.

Stefan Pachmajer and Benedikt Schrode is thanked for developing the excellent *GIDVis* software package, which probably saved most of my (undocumented) MATLAB scripts from being absolutely terrible to use.

Andrew Jones is thanked, first of all, for introducing me to the excellent British and Belgian cuisine and secondly, for years of successful scientific collaboration. Our joint trips to summer schools, workshops and synchrotrons have been absolutely *wicked*.

Special thanks go to my colleague and dear friend Paul Christian, with whom I had the pleasure of writing many lab reports and eventually even publishing in scientific journals. I truly enjoyed our years of fruitful collaboration and discussions about physics and life. I am looking forward to many more.

Zuletzt möchte ich mich bei meinen Eltern für die bedingungslose Unterstützung während meines Studiums bedanken. Ich danke euch dafür, dass ihr mir die Möglichkeit gegeben habt meine Interessen frei verfolgen zu dürfen.

Contents

1	Introduction	1
2	Fundamentals	5
2.1	Crystalline materials	5
2.2	X-ray diffraction	7
2.3	Crystal alignment on substrate surfaces	10
2.4	Crystalline samples in reciprocal space	12
2.4.1	Single crystals	12
2.4.2	Powder samples	13
2.4.3	Fiber textured 2D powders	14
2.4.4	Biaxially and partially aligned samples	15
2.5	X-ray detectors in reciprocal space	17
2.5.1	Point detectors	17
2.5.2	Area detectors	19
2.6	Diffraction patterns and data visualization	22
2.6.1	Powder samples	23
2.6.2	Fiber textured 2D powders	23
2.6.3	Single crystals and azimuthally textured samples	29
3	Methods	33
3.1	Pole figure analysis	33
3.2	Pole figure reconstruction	35
3.3	Reciprocal space conversion	39
3.3.1	Coordinate systems and rotations	40
3.3.2	Scattering vector calculation	42
3.4	Area detector calibration	45
3.4.1	Simulated annealing	47
3.4.2	Powder sample reference	48
3.4.3	Primary beam reference	52

4	Results	53
4.1	Complex behaviour of caffeine crystallites on muscovite mica surfaces ²⁰	53
4.1.1	Preface	53
4.1.2	Abstract	54
4.1.3	Introduction	54
4.1.4	Experimental Methods	56
4.1.5	Results	57
4.1.6	Discussion	63
4.1.7	Conclusion	69
4.1.8	Acknowledgments	70
4.1.9	Supplementary Information	70
4.2	Crystal alignment of caffeine deposited onto single crystal surfaces via hot-wall epitaxy ⁶³	75
4.2.1	Preface	75
4.2.2	Abstract	75
4.2.3	Introduction	76
4.2.4	Experimental section	79
4.2.5	Results	80
4.2.6	Discussion	86
4.2.7	Conclusion	94
4.2.8	Acknowledgements	94
4.2.9	Supplementary Information	95
4.3	Continuous crystal lattice tuning by non-stoichiometric intermixing of small organic molecules	99
4.3.1	Preface	99
4.3.2	Abstract	99
4.3.3	Introduction	100
4.3.4	Methods	102
4.3.5	Results	104
4.3.6	Discussion	112
4.3.7	Conclusion	118
4.3.8	Acknowledgement	119
4.4	Single step processing for epitaxial growth of a drug on an organic template: Example of carbamazepine on iminostilbene .	120
4.4.1	Preface	120

4.4.2	Introduction	120
4.4.3	Methods	121
4.4.4	Results and Discussion	122
4.4.5	Conclusion	126

5	Conclusion	127
----------	-------------------	------------

1 Introduction

Crystallization is the process of atoms or molecules arranging in an periodic fashion to form a solid structure. It is an essential step in the fabrication of solid materials and is still often considered a mystery due to its complexity. Classically, crystallization is started by dissolving a compound in a solvent. Subsequently, by changing temperature, concentration or other suitable process parameters, the solution is driven into supersaturation which triggers the formation of small crystalline nuclei or clusters which in turn allow for crystal growth.^{1,2} Such bulk crystallization approaches are often exploited in large industrial crystallization applications such as pharmaceuticals.^{3,4} Such crystallization techniques may yield single crystals but mostly crystalline powders which are used in further applications like tableting. However, for many technical applications, for example in organic electronics devices, crystalline materials are applied as thin film.^{5,6} Thus, it is necessary to carry out crystallization or grow crystalline films directly on top of a solid substrate. Interestingly, crystallization in the vicinity of surfaces can lead to remarkably different crystallization behavior. Often the occurrence of surface induced or mediated crystalline polymorphs is observed which cannot be obtained from bulk crystallization.⁷ Moreover, various surfaces can have a tremendous impact on the crystalline orientation and alignment, meaning the crystal morphology is altered by the substrate surface which can be exploited to satisfy technological demands.^{8,9}

While aligned crystalline films are highly interesting for technical applications, they also provide an experimental challenge in material characterization. First of all, thin crystalline films require experimental setup optimized for surface diffraction due to the low thickness of the crystalline layers, often in grazing incidence geometry.¹⁰ Secondly, the analysis of crystalline texture often demands special experimental geometries depending on the type of crystal alignment. This means, that standard laboratory setup as used for powder diffraction are only of limited use in the characterization of textured thin films. Moreover,

structural investigations of organic thin films are often limited to synchrotron facilities due to low scattering ability of organic molecules. While laboratory X-ray setups can be adapted to work in grazing incidence geometry, the accessible reciprocal space is often too limited to allow for a complete determination of the crystalline structure.¹¹ Also, due to the low flux of X-ray tubes, data collection times might exceed easily several days. These limitations can be overcome by carrying out experiments at synchrotron facilities, which allow for fast data acquisition, typically in the range of several seconds or minutes, depending on the beamline type (bending magnet, undulators) and detector dimensions. In combination with computational modeling it was possible to solve the full structure of several surface mediated polymorphs.^{12,13} However, for structure solution of thin films the sample quality is absolutely crucial in order to derive reliable crystallographic information. The ideal case are highly polycrystalline fiber-textured samples which feature a 2D powder statistic.¹⁴ Unfortunately, often this prerequisite is not fulfilled because of sample specific constraints such as preparation route or crystal habit among others. Hence, the resultant diffraction data is incomplete making reliable determination of structural properties impossible.

This thesis is focused on overcoming the experimental challenges in X-ray diffraction presented by such partially aligned or weakly textured organic thin film samples. The term *weakly* is chosen with regard to the azimuthal texture of the crystallites since the out-of-plane order (parallel to the substrate surface) is still well-defined by a single contact plane but the azimuthal alignment shows clearly preferred directions to some extent. Thus, such crystalline films can be considered an indeterminate case sharing characteristics of biaxially (strongly textured) and uniaxially (no texture) aligned films.

Already the presence of a weak texture renders standard grazing incidence X-ray measurements as employed for uniaxially samples useless since the diffraction condition is most likely not fulfilled for arbitrary azimuthal alignments. On the other hand, experimental methods suited for biaxially aligned samples which would be able to detect net planes regardless of their azimuthal alignment, are extremely time consuming and often not feasible due to limited beam time or the number of samples under investigation. Thus, a general and fast method for studying crystalline films regardless of the crystalline alignment is presented. It is based on mapping large regions of reciprocal space using X-ray

area detectors. Furthermore, the presented approach lowers the requirements on the experimental setups and shifts the main task towards data evaluation in reciprocal space rather than using individual experimental geometries for different diffraction measurements such as pole figures or reciprocal space maps. In order to illustrate the principle of this approach, various crystalline sample types and area detectors will be discussed, especially their representation in reciprocal space. Using the reciprocal space representation, the challenges of weakly textured samples will be elucidated and how area detector can be utilized to overcome these issues. Also, the benefits of carrying out data analysis in reciprocal space rather than in angular space will be addressed in detail. Moreover, data conversion from detector pixel data into reciprocal space which requires a reliable calibration routine will be elucidated.

Chapter Results contains manuscripts of already published studies and excerpts of studies still being in preparation for publication. The contributions of the individual authors for the individual studies and other remarks are given in a brief preface in the respective section. The first publication deals with the biaxially crystal alignment of caffeine at solid surfaces. The crystalline alignment is investigated using standard pole figure techniques and the epitaxial relations and crystallographic indexation of caffeine on muscovite mica is discussed in detail. This work was extended in order to study the growth of caffeine on alkali halide surfaces and the effect of temperature on crystal growth and is presented in the second publication. In contrast, the third work on non-stoichiometric substitutional mixed crystals of phenothiazine and iminostilbene, deals with the challenging case of weakly textured uniaxially crystalline samples, which could be successfully investigated by applying the insights obtained by studying area detectors and samples in reciprocal space. This allowed for the determination of crystallographic lattice shifts due to the intermixing. The last example of epitaxially grown carbamazepine on top of iminostilbene demonstrates the capabilities of 2D reciprocal space mapping and showcases the advantages of reconstructing pole figures from large reciprocal data sets rather than measuring individual pole figures directly.

2 Fundamentals

The following sections will introduce crystalline materials and X-ray diffraction. Since these topics are quite extensive on its own, only key concepts which are necessary to understand X-ray diffraction in the sense of the Laue condition are discussed. A general and comprehensive introduction into crystalline solids and X-ray diffraction can be found elsewhere.^{15,16}

2.1 Crystalline materials

Crystals or crystalline materials consist of a highly regular periodic arrangement of atoms. The smallest repetitive unit, the unit cell, hosts in the case of metals single atoms such as copper or iron or even multiple molecules as for example in organic molecular crystals. The microscopic unit cell extends in all spatial directions forming the crystal lattice or macroscopic crystal. The dimension of the unit cell is defined by six crystal lattice constants: a, b, c being the length of the unit cell edges and α, β, γ being the angles between the edges as shown in Figure 2.1. Using the crystal lattice constants, the lattice vectors $\mathbf{a}_1, \mathbf{a}_2, \mathbf{a}_3$ can be constructed to describe the unit cell. Using the lattice vectors, a point \mathbf{R} on the crystal lattice can be easily described by using a linear combination of the lattice vectors with \mathbf{R} being:

$$\mathbf{R} = u\mathbf{a}_1 + v\mathbf{a}_2 + w\mathbf{a}_3 \quad u, v, w \in \mathbb{Z} \quad (2.1)$$

Furthermore, the basis contains the relative positions of atoms or molecules with regard to a lattice point. Thus, by adding the basis to each lattice point a complete crystal structure can be obtained.

Often it is beneficial, especially with regard to X-ray diffraction, to consider the crystal lattice in reciprocal space rather than real space. Briefly, the reciprocal space is the Fourier transform of the real space crystal lattice. Thus, switching

to reciprocal space requires the Fourier transformation of the real space lattice vectors which yields the reciprocal lattice vectors \mathbf{b}_1 , \mathbf{b}_2 , \mathbf{b}_3 according to following equations:

$$\mathbf{b}_1 = 2\pi \frac{\mathbf{a}_2 \times \mathbf{a}_3}{\mathbf{a}_1 \cdot (\mathbf{a}_2 \times \mathbf{a}_3)} \quad (2.2)$$

$$\mathbf{b}_2 = 2\pi \frac{\mathbf{a}_3 \times \mathbf{a}_1}{\mathbf{a}_2 \cdot (\mathbf{a}_3 \times \mathbf{a}_1)} \quad (2.3)$$

$$\mathbf{b}_3 = 2\pi \frac{\mathbf{a}_1 \times \mathbf{a}_2}{\mathbf{a}_3 \cdot (\mathbf{a}_1 \times \mathbf{a}_2)} \quad (2.4)$$

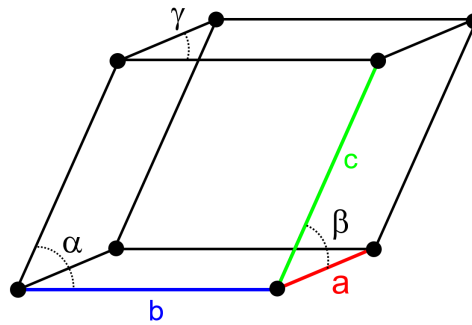


Figure 2.1: Crystalline unit cell (triclinic) with lattice constants a , b , c and angles α , β , γ .

Another useful concept to understand crystalline materials which is closely related to the lattice vectors are crystal net planes or lattice planes. Net planes repeat periodically over the whole crystal (or crystal lattice) and parallel net planes are separated by the interplanar distance (or net plane distance) d as depicted in Figure 2.2. Crystalline net planes are identified by Miller indices h , k , l , usually denoted as a triplet (hkl) . At this point the formalism of reciprocal lattice vectors becomes very handy, since net planes can be expressed as a vector \mathbf{G} , being a linear combination of the reciprocal lattice vectors, with the Miller indices h , k , l being the coefficients. Thus, a net plane is defined by:

$$\mathbf{G}_{hkl} = h\mathbf{b}_1 + k\mathbf{b}_2 + l\mathbf{b}_3 \quad h, k, l \in \mathbb{Z} \quad (2.5)$$

Moreover, the interplanar distance d for a specific net plane can be easily calculated since $d_{hkl} = 2\pi/|\mathbf{G}_{hkl}|$, meaning the magnitude of \mathbf{G} is connected to the net plane distance. Moreover, the direction of \mathbf{G} is perpendicular to respective the net plane as illustrated in Figure 2.2.

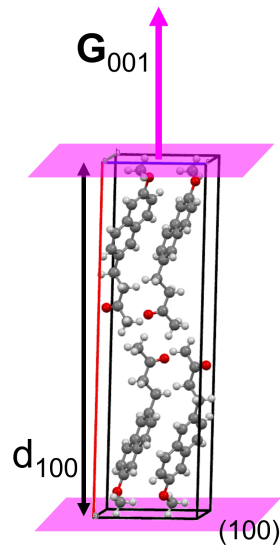


Figure 2.2: Example of (001) crystal net planes with the corresponding reciprocal lattice vector G_{001} and the interplanar distance d_{001} .

2.2 X-ray diffraction

X-rays are electromagnetic waves but with a particular short wavelength (or high energy), which is typically in the region of 0.1 nm. In contrast, visible light shows wavelengths roughly in the region of 200 to 800 nm, thus three orders of magnitude larger. Due to the large difference in wavelength, the interaction of X-rays with matter is remarkably different to visible light. Such as all types of waves, also electromagnetic waves are subject to diffraction effects caused by apertures such as pinholes or gratings. However, diffraction becomes only noticeable if the size of the aperture is similar to the wavelength of electromagnetic wave itself. Thus, for optical light diffraction occurs already using macroscopic pinholes as used in the famous double slit experiment to demonstrate the wave-like character of light. However, since X-rays are three orders of magnitude shorter, macroscopic objects will not cause any diffraction effects. However, the typical distance between the regularly arranged atoms in solids are in the region of several Ångström, thus forming a complex 3D dimensional diffraction grating for X-rays.

The first X-ray diffraction experiments were described by Max von Laue in 1912 by deriving a simple yet elegant condition for observing X-ray diffraction. In his famous Laue condition as given in Eq. 2.6 he connected the recip-

reciprocal lattice vectors \mathbf{G} , which are used to describe the crystallographic lattice of solids, to the real space momentum transfer or scattering vector \mathbf{q} , which describes the change in direction of an X-ray beam due to diffraction.

$$\mathbf{G} = \mathbf{q} \quad (2.6)$$

$$\mathbf{q} = \mathbf{k}_{\text{out}} - \mathbf{k}_{\text{in}} \quad (2.7)$$

Thus, \mathbf{q} is simply the difference of the outgoing and incoming wave vector \mathbf{k}_{out} and \mathbf{k}_{in} , respectively (see Figure 2.3). Constructive interference or diffraction occurs consequently, if a scattering vector \mathbf{q} equals a reciprocal lattice vector \mathbf{G} . Since both quantities are vectors, obviously the magnitude and direction of the vectors must be equal to fulfill the Laue condition. Since X-ray scattering is considered as an elastic scattering process (no energy is transferred) the magnitude of the scattering vector is defined solely by the wavelength of the X-ray source and does not change during the scattering event. The direction of the observed scattering vector \mathbf{q} depends therefore on the direction of the incoming and outgoing wave vector and is typically experimentally set by the position of the X-ray detector and source.

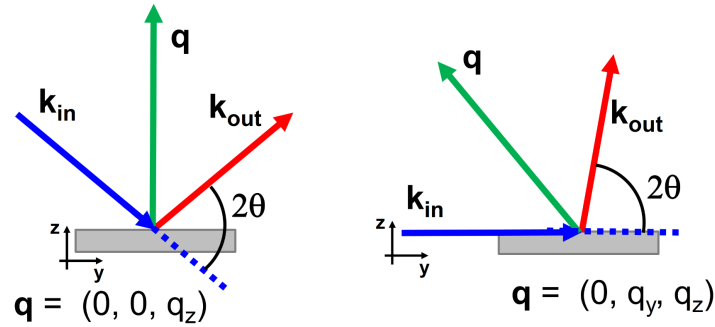


Figure 2.3: Different scattering geometries with identical scattering angle 2θ . \mathbf{k}_{in} and \mathbf{k}_{out} denote the incoming and outgoing wave vector, respectively, and \mathbf{q} the scattering vector (in sample coordinates). The grey rectangle indicates the sample orientation.

An alternative approach to X-ray diffraction is offered by the Bragg equation (which can be easily derived from the Laue condition). The Bragg equation is less abstract in its formulation and closer related to experimental setup since it is based on the experimentally measured scattering angle 2θ , the crystallographic lattice spacing d_{hkl} and the X-ray wavelength λ :

$$\lambda = 2d_{hkl} \sin \theta \quad (2.8)$$

However, this simplicity has its shortcomings. For example, the experimental setups depicted in Figure 2.3 have identical scattering angle 2θ , while the scattering vector \mathbf{q} as used in the Laue condition is clearly different. Thus, the use of the Bragg equation is mostly limited to powder diffraction where the sample orientation has no influence on the experiment. The Laue formalism is, despite being not as intuitive in its application, a more versatile and unambiguous method to evaluate X-ray diffraction, regardless of the experimental setup.

Regardless of the description used to interpret the results of X-ray diffraction, the underlying physical effect is explained by electromagnetic waves getting scattered by electrons within matter. If an incoming electromagnetic wave hits an atom it produces a secondary spherical wave. Due to the periodic structure of crystalline solids, these individual spherical waves are able to interfere and generate a characteristic diffraction pattern which is defined by the regular arrangement of the atoms. The scattered intensity for a specific net plane (hkl) can be described by using the structure factor F_{hkl} , which takes the chemical elements as well as the spatial arrangement of the atoms into account:

$$F_{hkl} = \sum_{j=1}^n f_j(\mathbf{q}_{hkl}) e^{-2\pi i(hx_j^f + ky_j^f + lz_j^f)} \quad (2.9)$$

The structure factor is the sum over all atoms j within the unit cell, with x_j^f, y_j^f, z_j^f being the fractional coordinates of the atoms and $f_j(\mathbf{q}_{hkl})$ being the atomic form factor which considers the chemical element of the atom. \mathbf{q}_{hkl} is the corresponding scattering vector for a specific crystal net plane (hkl) . The actual detected intensity $I \propto |F(hkl)|^2$. Hence, the idea for crystal structure solution is to use the intensity information to derive the atomic positions within solids. However, the accessible information measured in diffraction experiments is limited to the magnitude of the complex structure factor $F(hkl)$ and the important phase factor is not directly accessible. The lack of the phase information makes solving crystal structures based on diffraction experiments a challenging problem. Various methods exist to solve the phase problem, most prominently implemented in the software package SHELX. Since these structure solution

algorithms rely on statistical methods, they require large data sets containing several thousand Bragg reflections to provide reliable solutions. Hence, this particular route for structure solution is limited to single crystalline samples.

2.3 Crystal alignment on substrate surfaces

Often crystals appear in a regular pattern on solid surfaces. Such crystal growth is known as epitaxial or directed crystal growth and is governed by the underlying substrate surface. Surfaces of solid substrates can be divided into two groups based on the atomic order at the surface. Isotropic surfaces, which show no particular order of atoms at the surface and generally facilitate crystal growth with no particular azimuthal alignment. Such surfaces are found for example on glass (silica) or polymer substrates. In contrast, anisotropic surfaces, show a certain degree of order at the surface. This can be introduced by mechanical treatments like rubbing polymer surfaces or occur naturally as in the case of outer surfaces of single crystals. The latter are of particular interest since single crystalline surfaces are highly defined and can be easily accessed by cleaving single crystals as in the case of muscovite mica and alkali halide (NaCl, KCl) surfaces. The particular crystallographic properties of single crystalline surfaces are explained elsewhere.¹⁷ This section will briefly introduce the concept of surface directions and the determination of the crystallographic relation between the surface and the crystalline material on top.

Figure 2.4 illustrates the difference between an isotropically grown film and epitaxial growth. On the left, the individual crystallites show no preferred alignment with respect to the surface, hence a 2D powder or fiber-textured film is obtained (see Section 2.4, p. 12). In contrast, on the right image the individual crystals clearly favor two directions. The epitaxial relation is expressed in terms of crystallographic directions of the substrate and adsorbed crystals. The tool of choice to identify these directions is pole figure analysis as described in Section 3.1 (p. 33). Having established the crystallographic directions allows for studying the underlying alignment mechanism on an atomic level.

In Figure 2.5 an exemplary unit cell hosting two rod-like molecules is illustrated. Also, the substrate is now drawn on an atomic level, which in this case is a prototypical surface as encountered for alkali halide surfaces. Assuming that

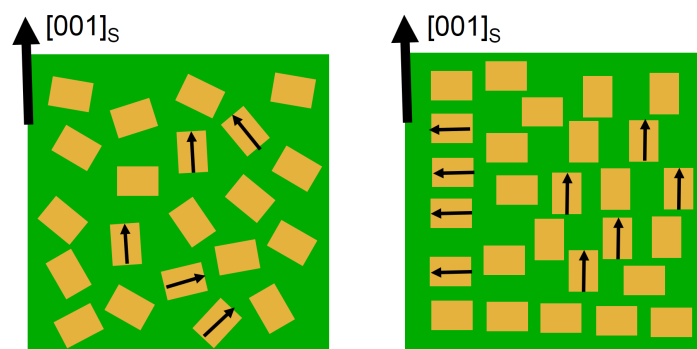


Figure 2.4: Different types of crystal growth on surfaces. The substrate is shown in green and the crystallites in yellow. Left: Isotropic crystal growth on a surface. Right: Epitaxial or directed crystal growth. Large and small black arrow indicate crystallographic directions of the surface and crystallite, respectively.

the pole figure measurements revealed an alignment of the $[010]_C$ axis of the adsorbed crystal with the $[001]_S$ and $[010]_S$ direction, the molecular alignment can be easily deduced. Symmetries play a rather important role for epitaxial growth since they are reflected in the crystal alignment. Looking at the atomic structure of the surface in Figure 2.5, a 4-fold symmetry is evident. Thus it is less surprising, that two (or four if the inverted case is also considered) crystal alignments are present on such a sample. However, on inspection of the underlying alignment mechanism it becomes clear, that actual interaction between the molecule and surface is identical for each case. However one should note, that only the molecular alignment with regard to the surface can be deduced. The actual or absolute position on the surface remains unclear. Nevertheless, the knowledge of the relative azimuthal alignment is an important input parameter for further computational studies which are often capable of determining the absolute adsorption geometry (and energy) with respect to the surface.

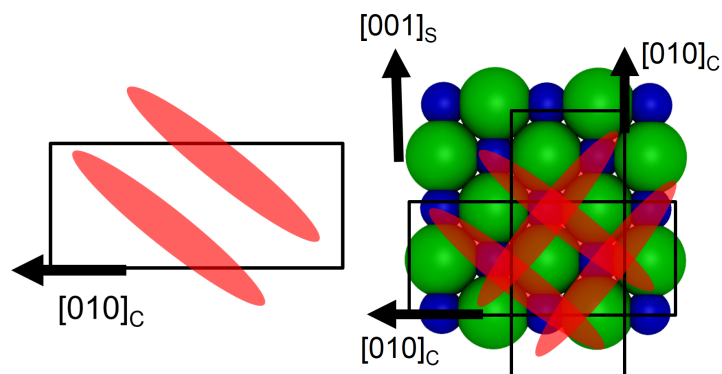


Figure 2.5: Left: Unit cell of an exemplary crystal with molecules indicated in red: Right: Alignment of the unit cell along substrate directions and resultant molecular alignment on top of the surface. Crystallographic directions are indicated by black arrows, indices C and S denote the crystal and substrate, respectively.

2.4 Crystalline samples in reciprocal space

In the following sections, various crystalline sample types based on the crystalline order will be elucidated. The main focus lies on effect of certain crystalline properties on the sample representation in reciprocal space. Thus, instead of using real space crystal net planes, the samples types are characterized by their reciprocal lattice vectors \mathbf{G} .

2.4.1 Single crystals

As briefly mentioned in Section 2.1, a perfect single crystal might simply consist of a single atomic species for example in metals or might be comprised of complex molecules as in the case of organic molecular crystals such as protein crystals. However, the crystal packing is considered to be absolutely regular and crystal imperfections such as misalignments or multiple domains are not present. In this ideal case, the crystalline net planes are precisely oriented in space, meaning the reciprocal lattice vectors \mathbf{G} are only a point in reciprocal space as illustrated in Figure 2.6. The left image shows a real space illustration of a sodium chloride crystal structure with different crystal net planes drawn in purple. On the right, the same information is presented in reciprocal space, thus the net planes are represented by reciprocal lattice vectors \mathbf{G}_{hkl} . Any kind

of crystal imperfections or polycrystallinity would lead to deviations of this point-like characteristic.

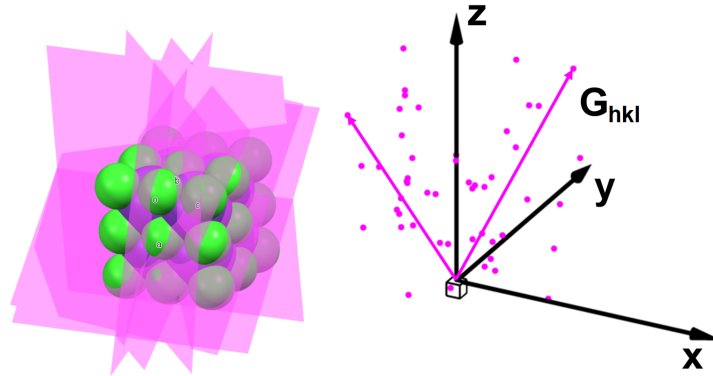


Figure 2.6: Illustration of real space representation (right) of various net planes and reciprocal space representation (left) of single crystals. Each dot corresponds to a crystalline net plane represented by a reciprocal lattice vector \mathbf{G}_{hkl} .

One should note that for crystals grown on top of a solid surface, only the upper hemisphere of the crystal is accessible during the experiment. The lower hemisphere is not accessible due to presence of the solid substrate. Obviously for free mounted single crystals, for example on top of a needle or powder samples in a capillary, the upper and lower hemisphere are accessible for data collection.

2.4.2 Powder samples

In contrast to single crystals with a highly defined spatial orientation, crystalline powders are characterized by the lack thereof. First of all, as the name already suggests powders are highly polycrystalline materials, thus they consist of many individual single crystals with dimension typically in the micrometer range. In perfect crystalline powders, the orientation of the individual crystals is completely random, thus no preferred orientation or texture is present. This causes the crystalline net planes to be randomly distributed in the sample, meaning a distinct orientation of reciprocal lattice vector \mathbf{G} is not given anymore. The end points of the reciprocal lattice vectors are therefore located on spherical shells, with the radius being defined by the magnitude of \mathbf{G} (see Figure 2.7). Thus, instead of a single point, each individual net plane is represented by a spherical shell in reciprocal space. Since the actual orientation of a net plane

can be neglected the vector based Laue equation is simplified to $|\mathbf{G}| = |\mathbf{q}|$, thus only the length of the scattering vector has to be taken into account for X-ray measurements.

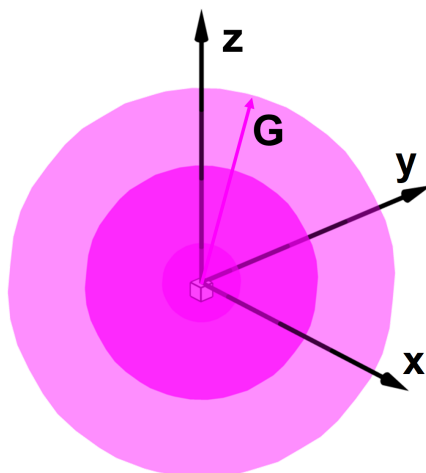


Figure 2.7: Reciprocal space illustration of a crystalline powder sample. Concentric spherical shells (shown in transparent purple) indicate the random spatial distribution of crystalline net planes represented by reciprocal lattice vectors \mathbf{G} . Please note, the inner spherical shells appear darker in color due the transparency.

Powder samples are encountered regularly in material characterization and are considered a standard X-ray measurement performed regularly on X-ray powder diffractometers using a specular geometry. In such an experimental setup, the scattering vector \mathbf{q} is kept perpendicular to the sample surface and only the length of \mathbf{q} is changed to probe for various net plane distances d in the sample. Obviously, such powder scans can be conducted rather easily since time consuming matching of the actual scattering vector \mathbf{q} and reciprocal lattice vector \mathbf{G} , as for single crystalline samples, is not necessary.

2.4.3 Fiber textured 2D powders

Fiber textured (or uniaxially aligned) samples are prototypical for organic thin films. Such samples show characteristics of single crystalline as well as powder samples, hence they are often referred to as 2D powders. Firstly, such samples are in the ideal case highly polycrystalline. However, in contrast to a 3D powder, the crystallites are only randomly distributed around one spatial axis, hence uniaxial. The crystallites contact the substrate surface with a defined net plane,

namely the contact plane. While the crystalline orientation parallel to the substrate surface is well-defined by identifying the contact plane (often called the out-of-plane order), the crystals show no particular azimuthal order (in-plane order) with respect to the surface. This means, the crystallites are randomly distributed with regard to the substrate surface normal (fiber texture axis). Hence, such films behave like powders with regard to the azimuthal or in-plane direction. This means that reciprocal lattice vectors \mathbf{G} show characteristics in between of single crystalline and powder-like samples. Since crystallites in all azimuthal directions are present, the reciprocal lattice vector \mathbf{G} is rotated around the fiber texture axis, usually the substrate surface normal. Thus, the point-like reciprocal spots of individual net planes of a single crystal transform into rings for fiber textured films as illustrated in Figure 2.8. Considering the illustration in Figure 2.8, it becomes clear that the separation into an out-of-plane (projection onto z-axis) and in-plane (projection onto x-y plane) component of the scattering vector \mathbf{q} is often used to characterize such fiber textured films. Since all azimuthal directions are equally likely, rotations around the surface normal during measurements are not required to obtain the complete crystallographic information as necessary for structural investigations.

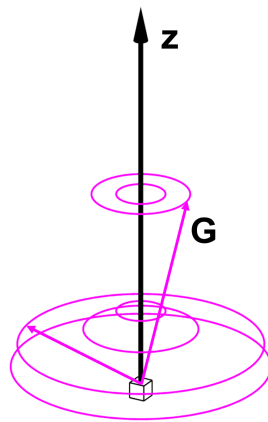


Figure 2.8: Reciprocal representation of a fiber textured 2D powder sample. Rings indicate the random azimuthal distribution of net planes (or reciprocal lattice points) represented by a reciprocal lattice vectors \mathbf{G} .

2.4.4 Biaxially and partially aligned samples

Biaxially aligned samples can be considered as strongly textured polycrystalline sample, meaning the crystalline film is comprised of multiple individual sin-

gle crystals showing a distinct crystal alignment with respect to the substrate surface as well as azimuthal order to some degree. Such crystal growth, often denoted as directed or epitaxial growth, is usually only observed on substrate surfaces with an anisotropic surface as provided naturally by single crystals. In a sense, these samples are quite similar to fiber textured films, which usually grow on isotropic surfaces like glass. The crystals have a defined contact plane but additionally have defined azimuthal alignment, thus biaxially aligned. Due to the crystal alignment along distinct azimuthal directions, the continuous rings as obtained for fiber textured 2D powders, show only intensity at specific azimuthal angles for biaxially aligned samples. Moreover, a fiber textured sample with weak statistics (or weak texture), meaning the crystallites are not evenly distributed or might even lack some azimuthal alignments, will result in rings with multiple gaps along the azimuthal direction (see Figure 2.9). In the case of highly defined biaxially aligned samples, the remaining ring-like features are reduced to point-like features. Thus, the additional order makes biaxially aligned samples or weak 2D powders basically identical to single crystals with regard to experimental demands. The difference to an individual single crystal is just that multiple alignments of the crystals might be present. This type of sample is usually investigated using the X-ray pole figure technique or require at least rotations around the azimuthal direction during grazing incidence diffraction measurements.

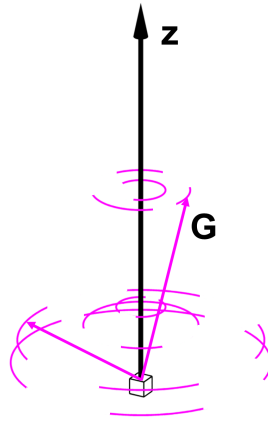


Figure 2.9: Reciprocal representation of a partially aligned fiber textured sample with weak statistics. Rings for the individual reciprocal lattice vectors G show gaps due to the weak crystal statistics. In the case of biaxially aligned films the remaining purple ring fragments are reduced to points.

2.5 X-ray detectors in reciprocal space

The aim of reciprocal space mapping is to sample points in reciprocal by experimentally selecting different scattering vectors \mathbf{q} and to record the corresponding diffracted X-ray intensities. In the previous sections the reciprocal representation of various crystalline samples types was already illustrated. Basically, depending on the sample type, material and the crystallographic information at hand, a set of reciprocal lattice vector \mathbf{G} can be constructed. Thus, the reciprocal space mapping will focus on regions in space where reciprocal lattice vector are expected. Unfortunately, often the lattice constants and therefore the actual position of the reciprocal lattice vectors \mathbf{G} are unknown. Hence, it is necessary to systematically sample extensive regions of reciprocal space to collect sufficient data for structural investigations. Depending on the sample type (single crystal, powders, fiber texture) and detector type (point detector, area detector) different data collection strategies can be employed to collect the necessary information in a reasonable time frame.

The principle of reciprocal space mapping as employed during this work using a point detector (pole figure measurements) and area detectors (grazing incidence diffraction) will be discussed in the following sections. The focus lies on the advantages of treating data independently of the experimental setup which eventually allows for exploiting the fast data acquisition times of area detectors to reconstruct arbitrary pole figures or reciprocal space maps from a large set of reciprocal scattering vectors which cannot be achieved with conventional point detector measurements.

2.5.1 Point detectors

Point detectors are most commonly found in laboratory setups since they are relatively cheap compared to line (1D) or area (2D) detectors. Another advantage is the high resolution, which can be achieved in combination with an optical slit system. As the name already suggests, a point detector measures a single point in space, thus a movable goniometer and sample stage is necessary to probe extensive regions of reciprocal space. While such detectors are often used for simple $\theta/2\theta$ powder scans, the following explanation will focus on the

purpose of data collection with regard to X-ray pole figure measurements since it can be easily extended to probe arbitrary regions of reciprocal space.

Figure 2.10 shows the spatial orientation of the $\{111\}$ net planes in the case of an exemplary sodium chloride single crystal used to illustrate the principle of reciprocal space mapping. Due the crystal symmetry four (in the upper hemisphere) equivalent net planes exists. Figure 2.11 depicts the same real space information translated into reciprocal space. It becomes obvious that for an arbitrary orientation of the sample and the X-ray setup it is very unlikely to match the Laue condition. In order to fulfill the Laue condition, firstly the length of the scattering vector \mathbf{q} must be chosen accordingly (defined by interplanar distance d_{111}). Since the orientation of the single crystal is usually not known, a systematic scan of the reciprocal space is conducted as depicted in Figure 2.11 right. This is achieved either by rotating the sample and thereby the reciprocal lattice vectors \mathbf{G} or by rotating the scattering vector \mathbf{q} , i.e. the source and detector. For experimental reasons, it is easier to perform sample rotations around two axes, the azimuthal axis φ (the surface normal) and the inclination axis ψ (parallel to the surface) rather than rotating the X-ray source and detector.

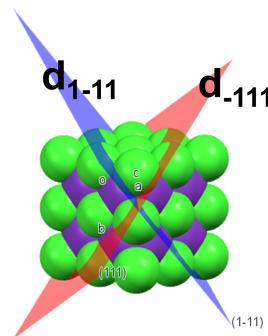


Figure 2.10: Illustration of a sodium chloride single crystal with the exemplary (1-11) and (-111) net plane (other equivalent net planes not shown)

This means, the scattering vector \mathbf{q} remains actually fixed in space in the laboratory system and the reciprocal lattice vectors \mathbf{G} is aligned with the scattering vector during the experiment. However, data analysis is much easier to conduct in the sample coordinate system (see Section 3.3.1, p. 40), since this representation is independent of the actual scattering geometry. Therefore, the illustrations such as in Figure 2.11 will be shown from the sample's point of view (sample coordinates). From this perspective, the sample is obviously fixed in space and the experimental setup appears to rotate around the sam-

ple. Regardless of the data representation, such a mapping strategy will probe only a spherical shell of reciprocal space (green dots in Figure 2.11), since the magnitude of \mathbf{q} is fixed. Typically step sizes of 1° in φ and 2° to 3° in ψ are necessary to achieve reasonable resolution in reciprocal space but these values depend in general on the divergence of the primary beam and optical slit system. Assuming count times of approximately five seconds per step (which is typical for weak scattering materials such as organic films) amounts to total data collection time of roughly 24 hours for one net plane distance. One can easily imagine that sampling extensive amounts of reciprocal space i.e. carrying out similar measurements for different d -spacings or scattering vectors \mathbf{q} , becomes quickly unfeasible due the extensive data collection time. Nevertheless, it is basically possible to probe large regions of reciprocal space as necessary for the calculation of reciprocal space maps if data acquisition times of multiple days and beam damage is not an issue. Fortunately, for typical pole figure measurements, the crystallographic unit cell of the material under investigation is usually available, making it possible to selectively probe the orientation space for individual net plane.

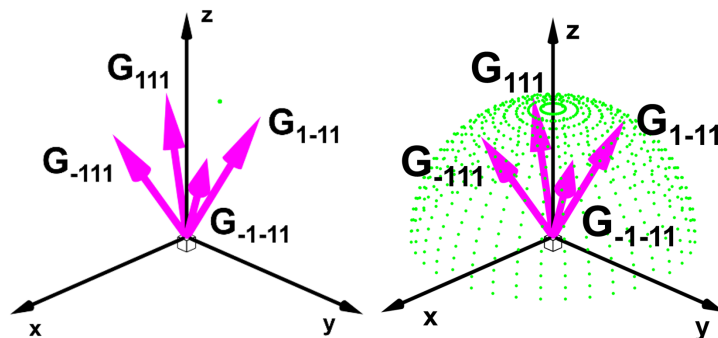


Figure 2.11: Reciprocal space representation of the (111) net plane family for a sodium chloride single crystal in the upper hemisphere. Arrows indicate the reciprocal lattice vectors \mathbf{G} for the corresponding crystal net planes. Left: Single green dot (end point of scattering vector \mathbf{q}) represents the reciprocal point sampled by a point detector which is fixed in space. Right: Set of points (green) collected during reciprocal space mapping for a typical X-ray pole figure measurement.

2.5.2 Area detectors

The use of area detectors is mostly limited to synchrotron beamlines due to their cost and complexity. The available sizes differ considerably, starting with

small 255×255 pixel detectors up to large two mega pixel detectors such as the Dectris Pilatus 2M. Since they cover an area and not a single point in space, a extensive regions of reciprocal space can be probed in one shot. Thus, in particular for large area detectors like the Pilatus 2M it is not necessary to perform detector movements to probe sufficient regions of reciprocal space. However, often smaller area detector (Dectris Pilatus 300K, Bruker Vântec 2000) can be mounted to a goniometer arm to combine the advantage of mapping larger regions of reciprocal space in one shot with the flexibility of a goniometer. This section deals with the representation of area detectors in reciprocal space and the opportunities offered with regard to various sample types as discussed on the previous sections.

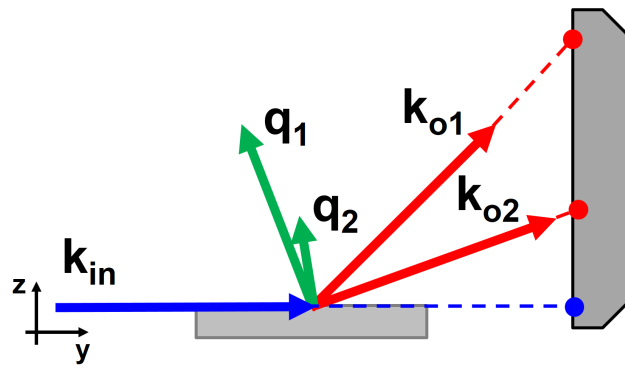


Figure 2.12: illustration of an area X-ray detector. The incoming wave vector is denoted as k_{in} , outgoing wave vectors for different detector pixels are k_{o1} and k_{o2} with corresponding scattering vectors q_1 and q_2 .

A typical area detector setup as used for thin film or surface diffraction is provided in Figure 2.12. The incoming beam represented by the wave vector k_{in} is usually fixed due to experimental limitation (ring plane of synchrotron). While in the case of a point detector setup each scattering vector is individually measured, each pixel in an area detector can be considered a separate point detector. For each pixel an outgoing wave vector k_{oi} can be constructed, if the pixel dimension and detector position is known (calibration and reciprocal space transformation of area detectors is covered in detail in Section 3.3, p. 39). Having k_{in} and k_{out} established allows for the calculation of corresponding scattering vector q for each individual pixel.

An important consequence of this particular scattering geometry is, that for each pixel the magnitude and direction of the q is different. In contrast, the

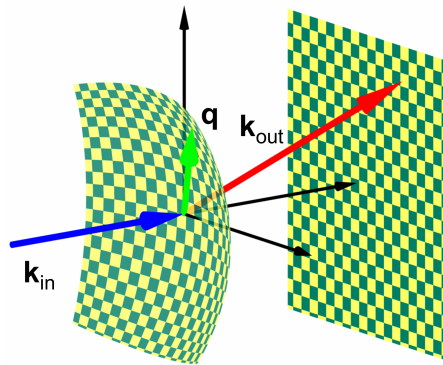


Figure 2.13: Reciprocal space representation of an area X-ray detector. The flat surface on the right with yellow/green boxes illustrates the pixels of an area detector in real space. The curved surface on the left illustrates the scattering vectors corresponding to the flat area detector in reciprocal space.

point detector setup described in the previous section used a scattering vector of constant magnitude and only the direction was changed during the measurement. (For the sake of completeness, in specular scan as used in powder scans, the direction of \mathbf{q} is kept perpendicular to the surface and only the magnitude of \mathbf{q} is changed.) Moreover, this behavior leads to an interesting problem of visualizing the scattering vectors. The raw data collected by an area detector is simply an image where each pixel contains intensity information but the corresponding scattering vector \mathbf{q} must be calculated separately. Having found the corresponding \mathbf{q} for each pixel allows then for the correct mapping of the measured intensity into the reciprocal space i.e. assign each \mathbf{q} the corresponding intensity. While the pixels on an area detector are distributed on a regular flat grid, the scattering vectors are located on a curved surface, the \mathbf{q} -surface for short, as illustrated in Figure 2.13. Thus, a true representation of the scattering data requires a 3D plot. However, depending on the information deduced from the scattering data, alternative representation like reciprocal space maps (RSM), powder plots or even pole figures can be used.

Going back to the example of the (111) sodium chloride as used in the previous section, the advantages (and drawbacks) of area detectors will become apparent as illustrated in Figure 2.14. First of all, the same problem, that the Laue condition is most likely not satisfied for an arbitrary sample/detector position, still persists. However, since an area detector already samples a surface in reciprocal space (instead of a single point) an azimuthal rotation of the sample will resolve this issue.

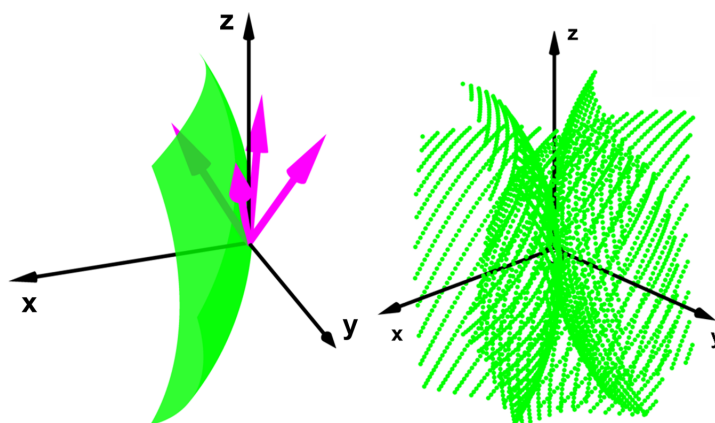


Figure 2.14: Left: Reciprocal space illustration of four lattice vectors \mathbf{G} (purple arrows) and the scattering vectors probed by an area detector (green surface). Right: Reciprocal space covered by performing azimuthal rotations of the detector surface leading to a cylindrical volume being probed. For the sake of clarity, only three of usually 360 azimuthal positions of the detector surface are shown. Lattice vectors \mathbf{G} are not shown.

This azimuthal rotation means that instead of only a surface, a large region (or volume) of reciprocal space can be probed very efficiently. The drawback of such an approach is obviously that large amounts of scattering data have to be collected. Furthermore, the experimental information is not directly available as in the case of point detector measurement, where the φ and ψ values were set during the experiment and could be directly related to crystallographic properties as in the case of pole figures. Thus, a certain amount of non-trivial data processing is necessary to derive crystallographic information as expected from pole figures or reciprocal space maps.

2.6 Diffraction patterns and data visualization

In this section, the insights gained by studying different sample types as well as including the characteristics of area X-ray detectors in reciprocal space will be used to explain the observed diffraction patterns on area detectors. Since sample and detector are represented by sets of scattering vectors and reciprocal lattice vectors, the obtained diffraction pattern is merely a consequence of the intersection of these sets since the Laue condition demands $\mathbf{G} = \mathbf{q}$ for diffraction.

2.6.1 Powder samples

Powder samples are characterized by its random orientation of crystallites, thus the reciprocal lattice vectors \mathbf{G} for individual net planes located on concentric spheres. Furthermore, the scattering vectors \mathbf{q} provided by an area detectors are located on a curved surface. Thus, applying the Laue condition $\mathbf{G} = \mathbf{q}$ means that diffraction is observed where the scattering vector surface cuts through the spheres of the reciprocal lattice vectors. This leads the observation of the famous Debye-Scherrer (DS) rings as illustrated in Figure 2.15. Each DS-ring belongs to a specific net plane and thus the scattering vectors \mathbf{q} are of equal magnitude, meaning $|\mathbf{q}|$ is constant along DS-rings while the direction of \mathbf{q} changes continuously. One should note that the Debye-Scherrer rings might appear as flat rings on an area detector, however, in reciprocal space, these rings are not contained in a plane, since the green detector surface shows a distinct curvature. Moreover, this means that crystallites with different orientations contribute to the formation of one diffraction ring. Hence, if Debye-Scherrer rings show gaps or fluctuations in intensity, it is a strong indication that the assumption of a perfect powder is not satisfied, meaning not all crystal orientation are present equally.

Typically, powder data is presented in a line plot (see Figure 2.16), with the x -axis being the magnitude of \mathbf{q} (or the wavelength dependent scattering angle 2θ and the y -axis the integrated intensity which is obtained by integrating all pixel which map onto the same scattering angle or $|\mathbf{q}|$. Obviously, all information about the powder texture or preferred orientations of the powder are lost due the integration process. Alternatively, reciprocal space maps are able to provide information about the powder texture.

2.6.2 Fiber textured 2D powders

Due the random alignment of the individual crystals around the fiber axis (usually the substrate surface normal), the reciprocal lattice vectors \mathbf{G} are located on rings. Keeping in mind that the area detector is represented by a surface in reciprocal space, it becomes clear that the Laue condition is only satisfied for single points where the \mathbf{G} -rings cut though the \mathbf{q} -surface as shown in Figure 2.17. Thus, the ideal diffraction pattern of fiber textured films consists of single spots, regardless of the azimuthal alignment of the sample. The appearance

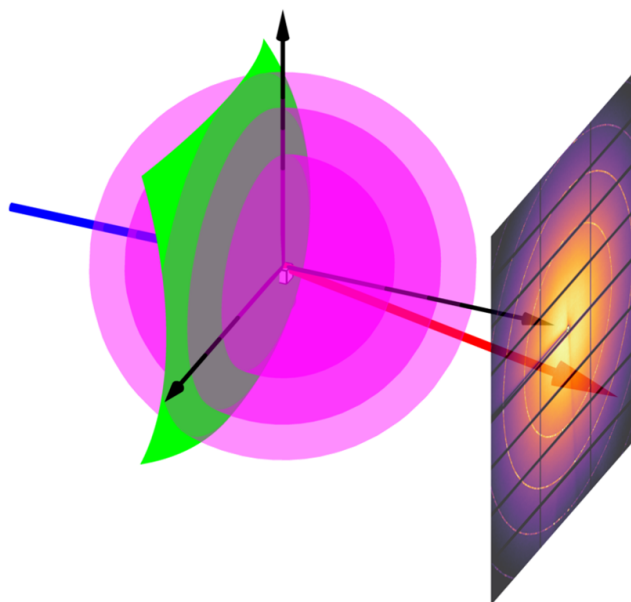


Figure 2.15: Diffraction pattern of polycrystalline random orientated (3D) powder on an area detector. Purple spherical shells indicate the reciprocal lattice vectors G of crystal lattice planes. Green surface illustrates the scattering vectors q detected by an area detector. Blue arrow indicates the incoming X-ray beam and red an exemplary scattered X-ray beam.

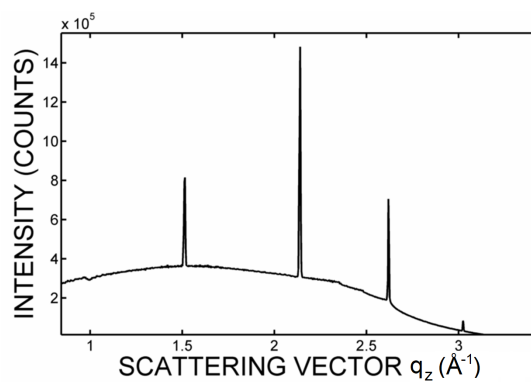


Figure 2.16: Integrated powder plot of LaB₆.

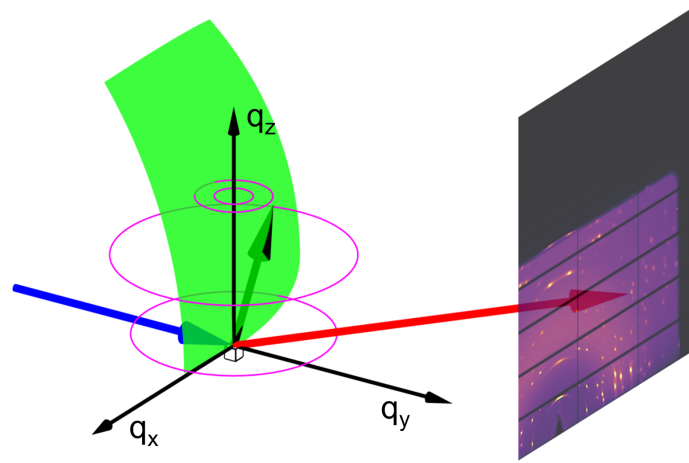


Figure 2.17: Diffraction pattern of fiber textured films on area detectors (right). Green surface represents the scattering vectors \mathbf{q} provided by the detector. Purple rings show selected reciprocal lattice vectors \mathbf{G} of a fiber textured sample.

of Debye Scherrer ring-like features in the diffraction pattern is an indication of mosaicity being present, meaning the crystallites show a certain degree of misalignment with regard to the contact plane.

One immediate consequence of the curved \mathbf{q} -surface is that certain parts of the reciprocal space are not accessible, especially along the specular direction q_z (blind area). As seen in Figure 2.17, depending on the position of the \mathbf{G} -rings it might be possible that they do not intersect with the \mathbf{q} -surface since it bends away from the specular direction. These net planes are not detected during the experiment. This effect becomes even more pronounced at higher q_z values. Hence, this approach is mostly used to study in-plane order of thin films, since the reciprocal space is easily accessible in this region.

Usually the diffraction data is visualized using reciprocal space maps. A reciprocal space maps is a 2D representation of the 3D scattering vectors, thus some information is again lost. Since each azimuthal direction for fiber textured samples is identical, it stands to reason to define the in-plane component of scattering vector $\mathbf{q} = (q_x, q_y, q_z)$ as:

$$q_{xy} = \sqrt{q_x^2 + q_y^2} \quad (2.10)$$

Therefore, the in-plane part is the projection onto the x - y plane, which is inde-

pendent of the azimuthal direction. In a reciprocal space map, it is plotted on the x -axis and the remaining out-of-plane component q_z is plotted along the y -axis. Thereby the 3D scattering vectors are reduced to a 2D data set which can be visualized more easily. While this operation seems harmless at first glance it causes a rather annoying problem. So far, there was a unique relation between each individual detector pixel, scattering vector and corresponding intensity value. However, due to the calculation of the in-plane scattering component q_{xy} this is not the case anymore. In contrast to the rectangular array of pixels on the area detector, the values obtained for q_{xy} and q_z are irregularly spaced, meaning they deviate from a rectangular shape and the size in reciprocal space varies for individual pixels. An exemplary reciprocal space map is shown in Figure 2.18, which illustrates the distortion introduced by the conversion into a reciprocal space map, especially apparent for values at high q_z and low q_{xy} . Another typical feature of reciprocal space maps are the gaps close the specular direction along q_z . While this gap is somewhat difficult to understand using only a reciprocal space map representation, it should be easy to see that this blind area is simply caused by the curvature of the \mathbf{q} -surface.

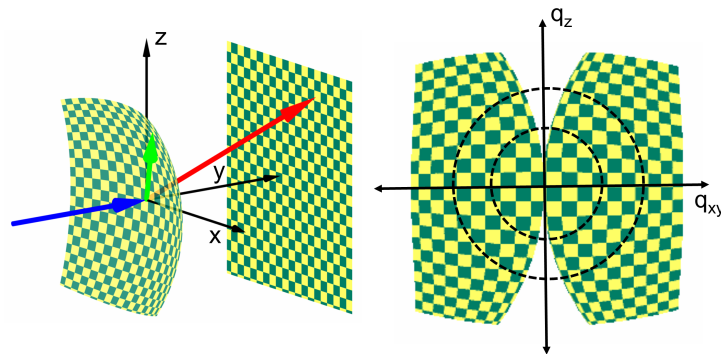


Figure 2.18: Left: Area detector with its scattering vectors in reciprocal space located on a curved surface. Right: Conversion of the scattering vectors into a reciprocal space map. Black rings indicate regions of constant q . Please note that the blurriness of the yellow/green boxes is due to the regridding process involved in the calculation of reciprocal space maps and not due to poor image processing.

The limits of the blind area can be obtained by a simple geometric consideration as depicted in Figure 2.19. The accessible space in a surface diffraction experiment is limited by the conservation of energy of the incoming beam $\mathbf{k}_{\text{in}} = 2\pi/\lambda$, leading to maximal length of $4\pi/\lambda$ for the scattering vectors (blue circle). Depending on the scattering geometry different areas are accessi-

ble. In the case of a grazing incidence geometry, the accessible space is limited to the purple half spheres centered at $C_1 = (\frac{2\pi}{\lambda}/0)$ with an radius of $2\pi/\lambda$. Deybe-Scherrer rings of constant $|\mathbf{q}|$ (green dashed line) can also be expressed as circles but with the center at $C_0 = (0/0)$ and a radius of $|\mathbf{q}|$. With increasing $|\mathbf{q}|$ the limit of the accessible space in grazing incidence geometry clearly shift along the purple circle. In order to obtain the exact limits in terms of q_{xy} and q_z one needs to solve for the intersection point of the green and purple circle (black \times in Figure 2.19 top). Unfortunately, an analytical expression for the corresponding q_{xy} and q_z is rather large and impractical but numerical solutions can be easily obtained.

Another route for establishing the limits in angular space is illustrated in Figure 2.19 bottom. The orange arrows illustrates a specular measurement with scattering vector \mathbf{q}_1 and corresponding scattering angle 2θ . In order to find the limit, one can rotate the incoming beam by θ . At this point the beam is parallel to the substrate surface, yielding scattering vector \mathbf{q}_2 (yellow). For further rotations, the incoming beam would be blocked by the substrate surface. This means that in the limiting case the scattering vector \mathbf{q}_2 is inclined by the angle θ with respect to surface normal. The value of θ can be obtained by the Bragg equation. Establishing these limits will help to understand the blind area during the pole figure reconstructions as discussed later in Section 3.2 (p. 35).

While the actual detector image and the reciprocal space map might look similar in their appearance, they are by no means interchangeable. This should become clear if the gap along the specular direction is considered. Only the correct representation in a reciprocal space map takes the lack of information about crystallites orientated towards the specular direction into account. Moreover, a reciprocal space map is only representative if the sample under investigations satisfies the requirements of 2D powders (no azimuthal dependence), since each scattering vector \mathbf{q} probes the intensity of crystallites with different azimuthal alignments. Samples which do not fulfill these condition like weakly (in-plane or azimuthally) textured samples, require careful experimental treatment and data analysis to obtain reliable diffraction results and will be discussed in Section 2.6.3.

Regarding the issue of the irregular data grids, different approaches are able to solve this issue. Of course, it is possible to plot each pixel with it corresponding size and shape (rectangular pixels mapped into reciprocal space maps become

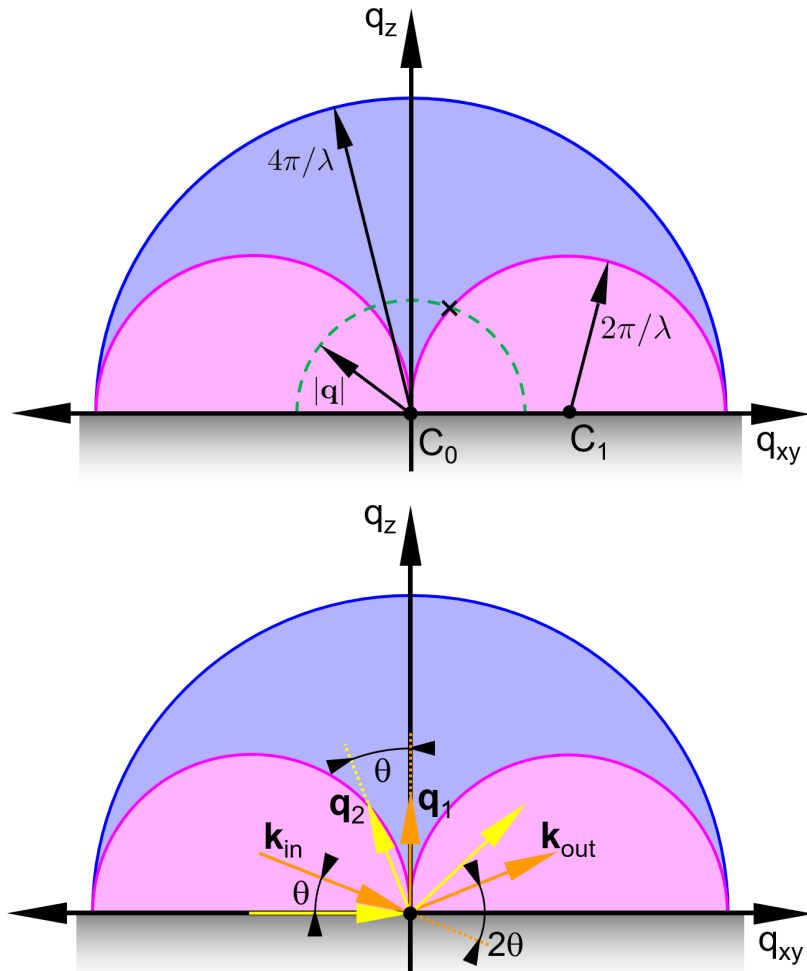


Figure 2.19: Accessible reciprocal space for surface diffraction limited by conservation of energy (blue circle). Purple half spheres are accessible for grazing incidence diffraction, remaining blue area can be accessed using specular scans and rocking curve measurements. Top: Green dashed line illustrates a Debye-Scherrer (DS) ring with constant $|q|$. Black \times marks the intersection of the DS-ring with the outer limit of the accessible reciprocal space in grazing incidence geometry. Bottom: Orange arrows illustrate a specular measurement with scattering vector q_1 and the corresponding 2θ angle. Yellow arrows illustrate the experimental limit for rocking curve measurements resulting in q_2 being rotated by θ .

trapezoid shaped) but firstly, this is very inefficient from a computational point of view and secondly, often data analysis is performed along constant values of q_{xy} or q_z . Hence, the data must be redistributed or recalculated on a regular grid with evenly spaced q_{xy} and q_z . One solution is simply to define a new regular grid and interpolate the existing data points onto this grid. While this provides an easy solution, the computational cost of interpolating a large 2D data sets is quite high and not an option for efficient data treatment. Another approach is based on redistributing the existing data on a regular grid, casually referred to as regridding. In contrast to interpolation, which recalculates the intensity data for each grid point, a regridding only redistributes the data points on a new regular grid. If multiple data points are assigned the same box, the average intensity is calculated. Obviously, the resultant quality of the regridded data depends on the resolution of the chosen grid and should therefore be obviously as close as possible to the original resolution.

2.6.3 Single crystals and azimuthally textured samples

So far mostly perfect or ideal samples were discussed. Unfortunately, often samples show characteristics of different film types which requires a thorough understanding of the individual features as described in the previous sections. While powders (3D and 2D) show continuous surfaces or rings of reciprocal lattice vectors \mathbf{G} , a single crystal is characterized by single point-like \mathbf{G} , meaning only one defined azimuthal direction is present and even using an area detector will usually not detect diffracted intensities since the Laue condition is most likely not be met. Therefore, an azimuthal rotation of the sample is performed, which will eventually rotate the reciprocal lattice points through the detector \mathbf{q} -surface. Figure 2.20 illustrates the situation for a static single crystalline sample and the effect of an 360° azimuthal rotation. On the upper half of the detector basically only the broad amorphous ring of the silica surface is visible, the lower detector half is blocked by the sample surface. Comparing the situation in Figure 2.20 for the rotated situation to the case of a fiber textured film as seen in Figure 2.8, the similarity of the ring-like \mathbf{G} distribution stands out immediately. Thus, by performing an azimuthal rotation of a single crystal a virtual fiber textured film is generated.

While this makes little sense for actual single crystals, since all the important azimuthal information is lost, it is essential for weakly textured film. Such

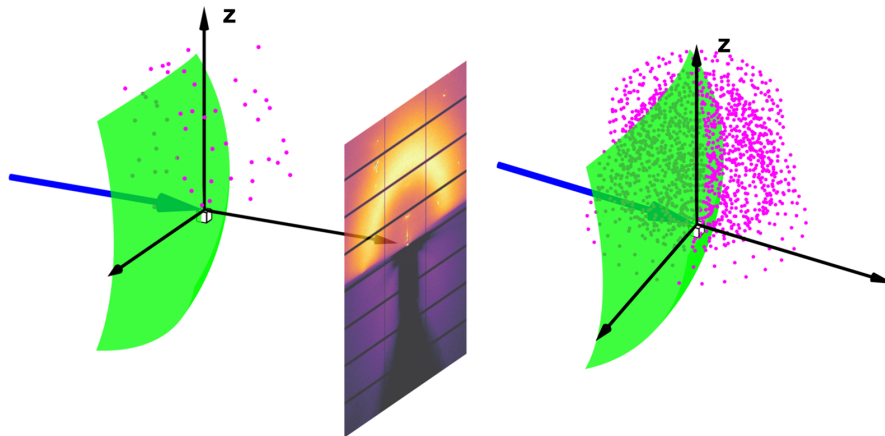


Figure 2.20: Left: Diffraction pattern of a single crystal on an area detector. Lower detector half is blocked by the sample surface. Reciprocal lattice vectors G of a single crystal and the area detector surface in reciprocal space are depicted as purple dots and as a green surface, respectively. Right: Reciprocal lattice vectors G forming rings after rotating the sample by 360° around the z -axis. Corresponding diffractions patterns are given in Figure 2.21.

films are expected to show uniaxially character, however the crystallites are not evenly azimuthally distributed. Instead of featuring continuous rings in reciprocal space, they show gaps of various sizes along the rings. While the collected single diffraction images usually contain considerably more information compared to a single crystal, large amounts of diffraction data might be missing, since for a particular azimuthal direction no crystallites met the Laue condition. In this case, an azimuthal rotation will be able to fill the gaps to obtain the remaining diffraction data. Depending on the purpose, it can be beneficial to collect individual images for each azimuthal step or to integrate a complete 360° turn into one single image. While the first option allows for a detailed texture analysis (pole figures), the azimuthal information is obviously lost in the latter. As an aside, data collection and rotations must be carried out continuously in any case, because using step-wise rotations could easily jump over certain lattice vectors and therefore some lattice planes might be undetected despite rotating by 360° .

The drastic effect on the obtained data quality of weakly textured films can be seen in Figure 2.21 as an example on a drop casted phenothiazine film. While the left image, obtained only by measuring a single azimuthal alignment contains virtually no useful information about the sample, the right reciprocal space

map looks like a typical result of a fiber textured film and show cases the importance of the azimuthal rotation for weakly textured films.

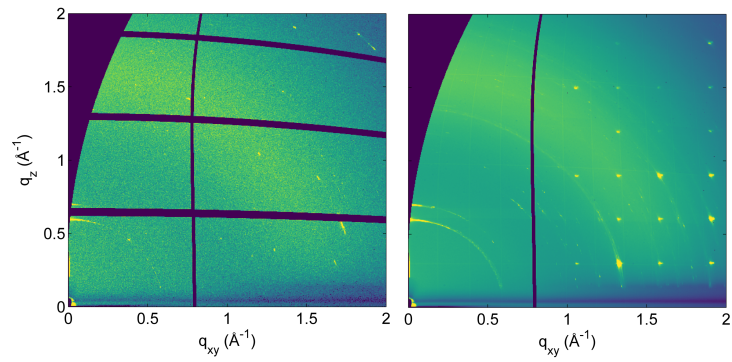


Figure 2.21: Left: Reciprocal space map of weakly textured phenothiazine film using a single azimuthal measurement. Right: Complete reciprocal space map obtained by 360° azimuthal sample rotation. Gaps in the images are due to the blind areas of the Pilatus 2M detector.

3 Methods

In this chapter the theoretical and experimental methods are presented to carry out the measurements and data analysis as used in this work. First, classic pole figure measurements and analysis based on reciprocal space mapping using a point detector (0D) will be discussed. In a next step this approach is extended to 2D reciprocal space mapping using area detectors in order to reconstruct arbitrary pole figures from a large set of scattering vectors. (The dimensionality of the reciprocal space mapping is chosen with regard to the detector in use.) Finally, the essential backbone of these methods, the conversion of detector pixel data into scattering vectors and area detector calibration, is covered in this chapter.

3.1 Pole figure analysis

In Section 2.5.1 (p. 17) a strategy for the reciprocal space mapping for pole figures as used in laboratory setups was introduced. During the measurement, the intensity in dependence of two orientation parameters φ (azimuthal angle) and ψ (tilt angle) is recorded. Typically pole figures are visualized in a polar plot using a stereographic projection. The orientation of the net plane normal is defined by the angles φ and ψ . This net plane normal can be considered as the radius of sphere. The stereographic projection onto the x - y plane is obtained by connecting the endpoint of the surface normal to the south pole of this very sphere as shown in Figure 3.1. The x - y plane is defined by the substrate surface. In general, a stereographic projection maps the surface of a sphere onto a plane using polar coordinates. The radius corresponds to the tilt angle ψ and the azimuthal angle corresponds to φ .

For the example of the NaCl(001) crystal (see Section 2.5.1 p. 17) with a (001) contact plane, the resultant pole figure shows four $\{111\}$ peaks at an inclination of $\psi = 55^\circ$. Due to 4-fold symmetry of the NaCl crystal, the poles appear every

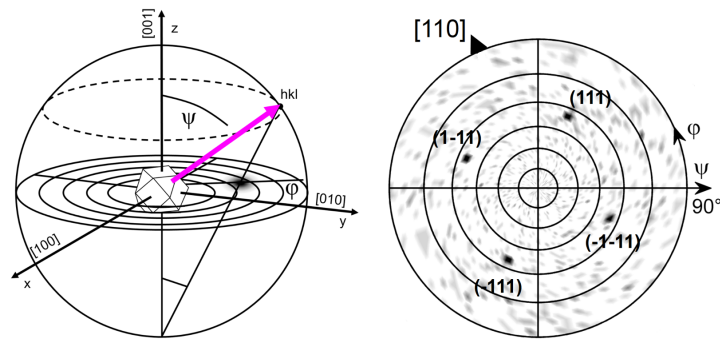


Figure 3.1: Left: Stereographic projection onto the x - y plane as used in pole figure visualization of crystal net planes.¹⁸ Purple arrows indicates the surface normal on a crystal net plane. Black dot in the x - y plane indicates the projected position. Right: Pole figure of NaCl showing the (111) peaks. Black arrow indicates the unit cell alignment.

90° along the azimuthal direction. Having knowledge of the contact plane and the crystal structure allows for the calculation of the tilt angles ψ and indexation of the poles with the corresponding Miller indices. The remaining unknown angle φ is simply obtained by matching the azimuthal peak positions with the measurement. For convenience, the obtained crystal alignment is expressed by using the real space crystal direction which are in-plane with the contact plane, such as the [110] in the case of NaCl(001). The crystallographic relation between two crystals is then expressed by the relative azimuthal shift between such real space directions as depicted in Figure 3.2 (relative azimuthal shift between the red and blue triangles which indicate the in-plane crystal alignments). The exemplary pole figure shows in total eight peaks, due to two individual crystals with different azimuthal alignment (marked as red and blue). One should note that pole figures are usually recorded for specific net plane d -spacings and thus only contain information about one particular net plane. This means that for each individual crystal separate pole figures need to be recorded to deduce an epitaxial relation.

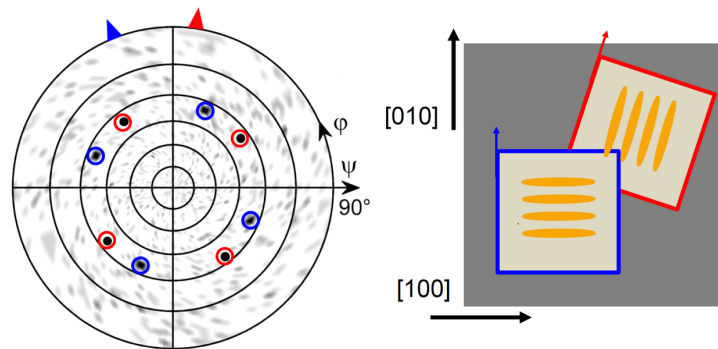


Figure 3.2: Left: Pole figure showing poles of two crystals (red and blue circles) with different azimuthal alignment indicated by colored triangles (red and blue). Right: Illustration of the corresponding unit cell alignment with respect to the substrate. Molecules within the unit cell are indicated as orange ellipses.

3.2 Pole figure reconstruction

While in Section 2.5.1 the typical data collection as used in laboratory setups with point detectors is described, this section will present a fast and efficient method for the indirect measurement of pole figures utilizing the full potential of area detectors.

Rather than performing a single measurement and integrating the collected intensities into a single diffraction image, as it is sensible for weakly textured films, individual diffraction images are saved for each azimuthal step. Usually 180 or 360 individual images are required to achieve a reasonable resolution in the azimuthal direction. Pole figures are typically visualized using the angles φ (azimuth) and ψ (inclination) which are used to describe the orientation of the scattering vector \mathbf{q} with respect to the sample surface (see Figure 3.3).

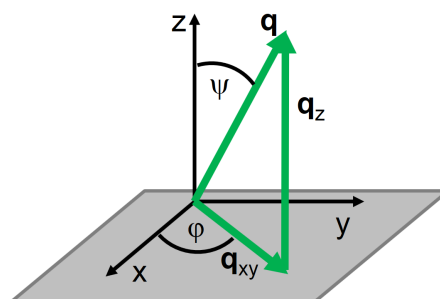


Figure 3.3: Angles φ (azimuthal angle) and ψ (inclination angle) define the orientation of the scattering vector \mathbf{q} with respect to the sample surface (grey).

Following the definition in Figure 3.3 these angles can be easily calculated as given in Eq. (3.1) with q_{xy} being the in-plane part of the scattering vector $\mathbf{q} = (q_x, q_y, q_z)$.

$$\varphi = \arctan \frac{q_x}{q_y} \quad \psi = \arctan \frac{q_{xy}}{q_z} \quad (3.1)$$

Having the azimuthal and inclination angles established, it is just a matter of selecting the correct scattering vectors \mathbf{q} based on their magnitude to match the net plane distance under investigation. An example using muscovite mica sample is given in Figure 3.4. Scattering vectors along the white circle of equal magnitude are selected for the pole figure reconstruction. Depending on the azimuthal position of the measurement, the Laue condition for the particular net plane is met (Figure 3.4 right) and diffracted X-rays are detected or not (Figure 3.4 left).

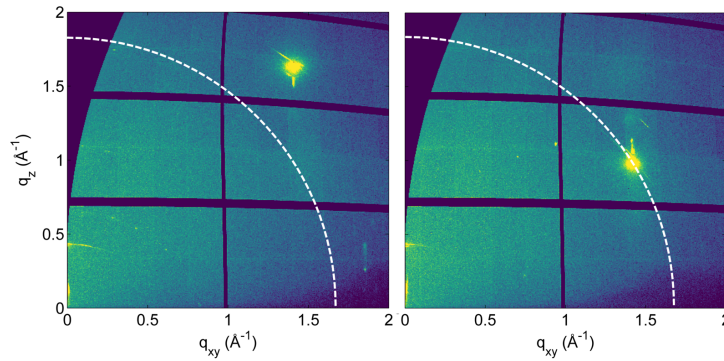


Figure 3.4: Two reciprocal space maps for different azimuthal sample positions of muscovite mica. The white circle indicates scattering vectors \mathbf{q} with equal magnitude as required for pole figure reconstruction.

The data collection strategy using a point detector directly measures scattering vectors by experimentally setting the azimuthal angle φ and inclination ψ and therefore provides equally spaced data points. However, using an area detector yields an irregular set of φ and ψ angles. Figure 3.5 illustrates the distribution of the selected scattering vectors in a pole figure in stereographic projection. A few interesting aspects concerning the pole figures reconstruction itself but also about the nature of reciprocal space maps can be deduced from this representation. The red lines represent the data extracted from a single azimuthal sample orientation (see Figure 3.5).

Firstly, the inclination angle ψ increases steadily along Debye-Scherrer rings,

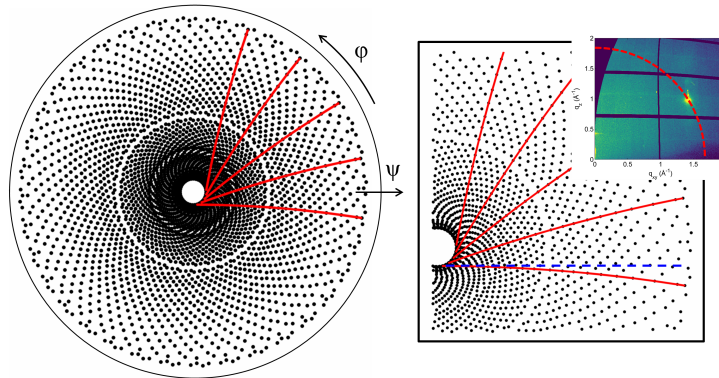


Figure 3.5: Left: Reconstructed pole figure plot showing the position of the single scattering vectors as obtained from 360 individual azimuthal measurements. Red lines indicate the location of data points extracted from single azimuthal images. Left: Detail of the pole figure showing the relative change in the azimuthal angle, blue dashed line is a guide to the eye. For clarity, only a fraction of the actual data is plotted.

which is evident, since the change from the out-of-plane to the in-plane direction takes place. However, the azimuthal angle φ of the crystallites changes too. Please note, the angle φ is related to the actual crystallite orientation and must not be confused with the azimuthal angle of the sample itself, as set during the experiment. The change of φ along a Debye-Scherrer ring is simply a consequence of the curved area detector surface in reciprocal space, which causes an azimuthal rotation. While the extracted red lines appear only slightly curved, it is important to note that they do not run through the center of the pole figure, hence the change in the azimuthal angle φ is approximately 80° along the ring as seen in Figure 3.6.

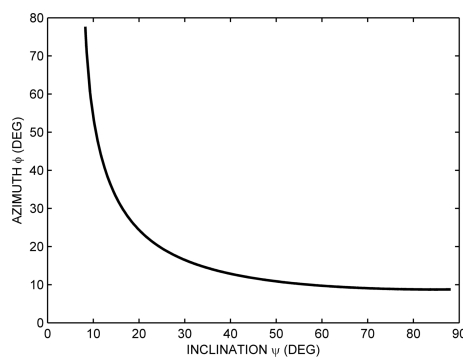


Figure 3.6: Change of the relative azimuthal angle φ depending on the inclination angle ψ along a Debye-Scherrer ring.

Nevertheless, this offers an interesting insight into the composition of recipro-

cal space maps too, thereby highlighting the importance of a proper 2D powder statistics since individual data points in reciprocal space maps are connected to specific crystal orientation. Another striking feature is the empty space or blind area in the center of the pole figure. The center of a pole figure features inclination angles ψ close to 0° , meaning the scattering vectors are approximately perpendicular to the substrate surface, hence orientated in the specular direction, which is not accessible in grazing incidence geometry. But as already seen by the gaps in the reciprocal space maps and also in Figure 3.6, a lower limit of ψ is evident. Finding the limits of the blind region in terms of q_{xy} and q_z for the correct \mathbf{q} (see Section 2.6.2, p. 23) as defined by the netplane distance for a particular pole figure allows for the determination of the limiting value of ψ for the blind area in the center by using Eq. 3.1. In terms of the angular space, the limiting ψ can be expressed as the Bragg angle θ as obtained from the Bragg equation by:

$$\theta = \arcsin \frac{\lambda |\mathbf{q}|}{4\pi} \quad (3.2)$$

Using typical values for the wavelength $\lambda = 1.4 \text{ \AA}$ and $|\mathbf{q}| = 0.5 \text{ \AA}^{-1}$ to 2.5 \AA^{-1} yields limiting ψ values of 3° to 16° , respectively. Thus, only information close to the specular direction is inaccessible, which is usually of little interest in pole figure evaluation due to the limited azimuthal information available at small inclination values of ψ .

The final step to obtain an actual pole figure is simply mapping the intensities onto the corresponding scattering vectors. So far, a strict correlation between each data point in the pole figure and a detector pixel still exists. However, reminiscent of the issues with reciprocal space maps, some sort of regridding or interpolation has to be conducted for further efficient data treatment. While regridding is the method of choice for reciprocal space maps, data interpolation on a regular grid has proven more useful regarding the data quality in this case.

The remarkable difference to a classic pole figure measurement using a point detector is the versatility of this approach. While a point detector samples the reciprocal space on a spherical shell defined by a specific net plane distance, the 2D reciprocal space mapping acquires large regions of reciprocal space, thus the measurement is not limited to a certain net plane distance, which allows for

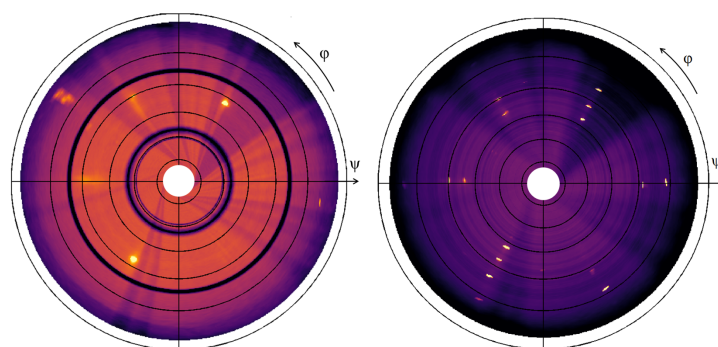


Figure 3.7: Left: Reconstructed pole figure for muscovite mica (023) net planes using an area detector for reciprocal space mapping. Right: Integrated pole figure over the region $0.9 \text{ \AA}^{-1} < |\mathbf{q}| < 1.9 \text{ \AA}^{-1}$.

the calculation of pole figures for arbitrary net plane distances. Total data acquisition times are typically as short as 15 minutes if experiments are conducted at synchrotron beamlines and data processing for individual pole figures is only a matter of second on modern personal computers. Hence, literally thousands of pole figures (step size of $|\mathbf{q}| = 0.001 \text{ \AA}^{-1}$) can be calculated in minutes, which allows for a virtually continuous exploration of the complete reciprocal space. While the classic pole figures method is limited to the knowledge of the exact position of net planes and therefore the crystallographic unit cell, this approach allows for the investigation of material without any crystallographic knowledge beforehand. Furthermore, unexpected behavior, like phase transformation or hydrate/solvent formation, will be covered by this approach. Such pseudo polymorph formation will be overlooked by classic pole figure measurements if not specifically taken into consideration. Another possible application is the calculation of integrated pole figures. Instead of limiting the data selection on a specific net plane, a range of net plane distances is selected and integrated into a single pole figure demonstrating the versatility this method.

An successful application of this method is presented in Section 4.4 (p. 120) using the example of epitaxially grown carbamazepine on iminostilbene.

3.3 Reciprocal space conversion

This technical section covers the conversion of individual detector pixel positions into scattering vectors \mathbf{q} . This step is essential for any further data analy-

sis. The accuracy of the conversion relies on the knowledge of the exact position and orientation of the sample and detector, which is obtained by a calibration routine.

3.3.1 Coordinate systems and rotations

In order to start any kind of calculation the coordinate systems and convention regarding the sample, detector and experimental setup must be defined. The chosen coordinate for this work is depicted in Figure 3.8. The main coordinate system (laboratory system) is chosen, so that the x - y plane is parallel to experimental hutch floor with the origin located in the center of rotation of the goniometer, the point where the scattering is considered to take place or more casually, where the beam hits the sample. In the neutral position (all angles are set to 0°) this means that the sample surface is also parallel to the x - y plane and the area detector plane will be oriented perpendicular, hence parallel to the z - x plane. The incoming beam is along the y -direction. If a detector is mounted on a goniometer arm, the δ -rotation is performed around the x -axis (up/down) and the γ -rotation is around the z -axis (azimuthal). All goniometer rotations are performed around the point of origin (ideally this matches the point of scattering).

In this work, only goniometer geometries with the δ -arm mounted on top of the γ -arm will be discussed. Thus, a γ -rotation changes the position of the δ -arm, which makes it imperative to consider the correct order of rotation. Deviating geometries, like the κ -geometry are not covered, however the general approach to data conversion remains unchanged, but the corresponding rotation matrices must be adapted to reflect the κ -geometry. Furthermore, sample rotations are denoted as α (around the x -axis), which sets the incidence angle of the beam with respect to the sample surface and χ (around the y -axis), which should usually be 0° after proper sample alignment. Lastly, the azimuthal alignment of the sample is set by φ -rotations around z -axis. Again, the order of rotations is decisive for the actual combined rotation. Since the experimental setup should allow for easy azimuthal scans, the φ rotation must be applied after the α and χ rotation. Moreover, φ -rotation axis must be set perpendicular to the sample surface to avoid a wobbling motion whilst rotating.

Furthermore, the detector itself might not be mounted perfectly perpendicular

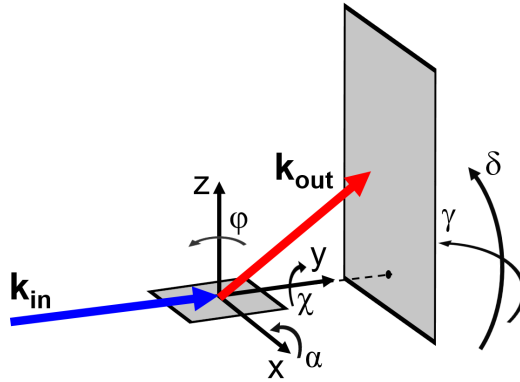


Figure 3.8: Coordinates used for the description of the experimental diffraction setup. Arrows indicate the incoming (blue) and outgoing (red) wave vector. Dashed lines indicate the center pixel on the detector, α , χ and φ denote the sample rotations around the sample axes, δ and γ indicate the detector rotations around x and z -axis, respectively.

to the goniometer arm or in the case of a static detector not being positioned on a perfectly flat surface. Thus, rotation around all three axes x , y and z of the detector have to be considered. However, these rotations need to be performed in the detector plane coordinate system.

Finally, the most important coordinate system is the sample coordinate system. Since the reciprocal lattice vectors \mathbf{G} are calculated naturally in this reference frame the scattering vectors are only meaningful in this particular coordinate system. The primary reason for the mismatch of the laboratory and sample system is the necessary non-zero incidence angle of the X-ray beam for scattering experiments. Since the incoming wave vector is fixed by the orientation of the synchrotron beam, the sample needs to be rotated around α . This leads to the situation as shown in the image of Figure 3.9. The scattering vectors \mathbf{q} are calculated using the incoming and outgoing wave vectors. Since these wave vectors are defined in the laboratory system, also the scattering vectors \mathbf{q}_L are obtained within this reference frame. This means, for example, the scattering vector \mathbf{q}_2 is not specular in the laboratory system as indicated by the non-zero q_y component. However, the transformation into the sample system leads to the scattering vectors \mathbf{q}_S . Due to the applied rotation during the transformation, only the q_z component of \mathbf{q}_2 remains. Hence \mathbf{q}_2 is specular in the sample coordinate system. This means that diffracted intensity for specular net planes will be observed. One should note that scattering would obviously occur in any case, since \mathbf{q}_2 and \mathbf{G} fulfill the Laue condition regardless of the chosen

coordinate system. However, if the scattering vectors are not presented in the sample coordinate system, the deduced physical information, would be incorrect since the wrong \mathbf{q} and \mathbf{G} vector would be matched i.e. one would assume non-specular net planes. In general, the transformation from the laboratory to the sample system consists of rotations around α , χ and φ in the correct order as defined by the stacking of the motors on the sample stage.

$$\mathbf{q}_{L,2} = (0, q_y, q_z)$$

$$\mathbf{q}_{S,2} = (0, 0, q_z)$$

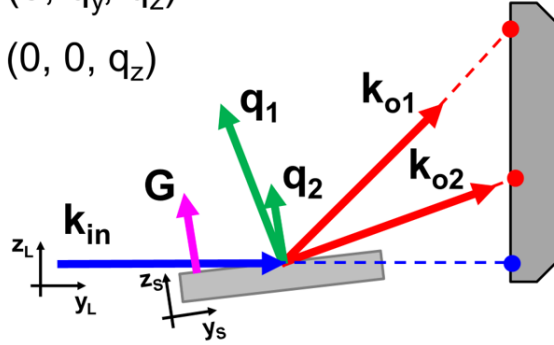


Figure 3.9: Scattering experiment in laboratory and sample coordinate system. Incoming and outgoing waves are indicated in blue and red, respectively. Scattering and reciprocal lattice vectors are shown in green and purple, respectively. Subscript L and S denote the laboratory and sample coordinate system.

3.3.2 Scattering vector calculation

Having established the basis of diffraction and defined the necessary coordinate systems in the previous sections, the actual calculation of the scattering vectors can be carried out. For the sake of simplicity, detector misalignments or goniometer rotations are not considered at first and will be discussed after the concept of basic scattering vector calculations is introduced. A scattering event is simply the momentum transfer or in the case of elastic scattering only the change in direction of an incoming X-ray beam. Hence, it follows:

$$\mathbf{q} = \mathbf{k}_{out} - \mathbf{k}_{in} \quad (3.3)$$

\mathbf{k}_{out} and \mathbf{k}_{in} are incoming and scattered outgoing wave vectors, with the magnitude being defined by $2\pi/\lambda$, with λ being the X-ray wavelength. For simplifying the calculation, the magnitude of the wave vectors is omitted since

it only acts as a constant factor during the calculations. Thus, the wave vector is basically an unit vector pointing in the direction of the traveling wave. The incoming beam $\mathbf{k}_{\text{in}} = (0, 1, 0)$ is defined by the experiment and assumed parallel to the y -direction as it usually the case at synchrotron facilities. Therefore, \mathbf{k}_{in} is already defined and only \mathbf{k}_{out} , or more precise the direction of \mathbf{k}_{out} needs to be found to obtain the scattering vectors.

Pixel positions on the area detector are calculated relative to the center pixel located at the pixel coordinates x_{cp} and z_{cp} , which is the position of the primary beam at the detector. The exact position of a pixel \mathbf{p} on the detector plane with pixel coordinates (x, z) is simply obtained by using the pixel sizes s_z, s_x and the sample-detector distance (or center of rotation – center pixel distance to be precise) d_{SD} :

$$\mathbf{p} = \begin{pmatrix} (x - x_{\text{cp}})s_x \\ d_{\text{SD}} \\ (z_{\text{cp}} - z)s_z \end{pmatrix} \quad (3.4)$$

Normalizing \mathbf{p} will yield the outgoing wave vector \mathbf{k}_{out} which points in the direction of the corresponding pixel, allowing for the calculation of \mathbf{q}_L by subtracting \mathbf{k}_{in} .

Since the scattering vectors are obtained in laboratory coordinates, the vectors need to be transformed into the sample system (\mathbf{q}_S) by applying the transformation matrix \mathbf{T} which is composed generally of the individual rotations χ, α and φ . In the simplest case of $\chi = \varphi = 0$ and with α being the incidence angle, \mathbf{T} reduces to the rotation matrix around the x -axis.

$$\mathbf{q}_S = \mathbf{T}\mathbf{q}_L \quad (3.5)$$

$$\mathbf{q}_s = \begin{pmatrix} 1 & 0 & 0 \\ 0 & \cos \alpha & -\sin \alpha \\ 0 & \sin \alpha & \cos \alpha \end{pmatrix} \mathbf{q}_L \quad (3.6)$$

Finally, since the pre-factor of the wave vector was neglected so far, \mathbf{q} needs to be multiplied by $2\pi/\lambda$ to obtain the correct length of \mathbf{q} . The advantage or peculiarity of this approach for calculating scattering vectors is that the vectors are obtained directly without the occurrence or need of wavelength dependent

quantities such as the scattering angles.

So far, the detector was assumed to be perfectly perpendicular to the incoming beam, meaning the goniometer arm angles δ and γ are zero and it is mounted without any tilt onto the goniometer. To take goniometer rotations and detector misalignments into account additional rotations at different steps in the calculation of \mathbf{p} are required. Firstly, the tilt of the detector with respect to goniometer at $\delta = \gamma = 0$ is considered. This situation is equal to a large detector simply put on laboratory rack or table as it is often the case. These rotations are performed in the detector plane coordinate system. Instead of adding the sample-detector distance d_{SD} to the pixel position vector \mathbf{p} , the y -component is set to zero. This allows for the rotation around all three directions in the detector plane. Around z and x the tilt of the detector is set. Rotating around y allows for the rotation around the beam axis, leading to the following expression for a pixel position \mathbf{p} with \mathbf{R} being rotational matrices:

$$\mathbf{p} = \mathbf{R}_x \mathbf{R}_y \mathbf{R}_z \begin{pmatrix} (x - x_{cp})s_x \\ 0 \\ (z_{cp} - z)s_z \end{pmatrix} + \begin{pmatrix} 0 \\ d_{SD} \\ 0 \end{pmatrix} \quad (3.7)$$

After performing the rotations, the detector is moved to the according sample-detector distance by adding d_{SD} to the y -component of \mathbf{p} .

The position of the goniometer is also taken into account by two rotations. However, the difference is the center of rotation. While the detector orientation related rotations were performed in the detector plane, the goniometer arm rotations are with respect to the laboratory coordinate origin. Thus, \mathbf{p} is rotated by the angles δ and γ around their respective axes with \mathbf{R}_δ and \mathbf{R}_γ being the rotational matrices yields:

$$\mathbf{p}' = \mathbf{R}_\gamma \mathbf{R}_\delta \mathbf{p} \quad (3.8)$$

While these rotations appear simple at first glance, they differ to the rotations as encountered in the detector tilt. While in the case of the detector, the order of rotations can be arbitrarily chosen but needs to be kept consistent throughout the calculation, the order for the goniometer rotations must be chosen to match the actual rotations of the experimental setup. Since the δ arm is mounted on top of the γ arm, any movement in γ will influence the movement of δ , thus

rotations are not commutative. While during the experiment γ moves first and is followed by the movement of δ , the actual order of rotations must be reversed to mimic this behavior. For more information about this particular confusing property of rotations, the reader is referred to the topic of extrinsic/intrinsic rotations. To summarize, for the specific case of the goniometer geometry in this example, it turns out that \mathbf{R}_δ is the rotation matrix \mathbf{R}_x and \mathbf{R}_γ will be \mathbf{R}_z . Lastly, an offset of the outer detector arm γ can be taken into account by simply adding an offset value to the position of γ . Such a correction considers, that the inner δ arm moves in a slightly different plane as expected thereby correcting experimental uncertainties of the setup. Additional information regarding area detector misalignments can be found elsewhere.¹⁹

Applying all these additional rotations for the detector and goniometer allows for the most general calculation of outgoing wavevector \mathbf{k}_{out} and eventually for the conversion of detector pixels into reciprocal space vectors.

3.4 Area detector calibration

This section covers the essential step of area detector calibration, meaning establishing the exact position and orientation of an area detector which is essential for accurate and reliable assignment of scattering vectors to individual detector pixels as described Section 3.3. Several parameters (parameter set) are necessary for determining the correct scattering vectors, whereby some are usually directly accessible such as

- X-ray wavelength
- Number of detector pixels (column, rows)
- Pixel size

The last two parameters are typically stated in the detector manual and the wavelength can be set extremely accurately using monochromators. However, if necessary, these parameters could also be obtained by a calibration routine. But obviously, the more information is available beforehand, the easier it gets to reliably determine the remaining parameters. The next parameters are usually not directly accessible and need to be found by using a calibration routine:

- Sample detector distance d_{SD}

- Center pixel x_{cp} and z_{cp} (position of primary beam)
- Detector misalignments (rotation of detector around x - y - z axis)
- Goniometer offset (only for non-static setups)

Depending on the experimental setup different approaches can be utilized for obtaining a detector calibration. In either case, the basic principle is to match a theoretically well-known data set of scattering vectors \mathbf{q}_{ref} to an experimentally obtained data set \mathbf{q}_t (trail scattering vectors) in reciprocal space. In the following section, the term set is used to describe a collection of individual scattering vectors with no particular order. This abstraction allows for an experimentally independent description and implementation of the calibration routine. In order to achieve agreement between the experimental data set \mathbf{q}_t and the theoretical data set \mathbf{q}_{ref} , the unknown detector parameters are varied. For each set of detector parameters, a new set of trail scattering vectors \mathbf{q}_t is then calculated. The goodness of the calibration is then judged by the difference of the theoretical data set to the experimental set. This difference will be referred to as the distance function E with $\mathbf{q}_{t,i}$ and $\mathbf{q}_{ref,i}$ being the individual trail and reference scattering vectors contained in the sets:

$$E(\mathbf{q}_{ref}, \mathbf{q}_t) = \sum_{i=1}^n |\mathbf{q}_{ref,i} - \mathbf{q}_{t,i}| \quad (3.9)$$

If the overall distance between experimental and theoretical data sets decreases the calibration is considered to be improved. Thus, obtaining the best calibration is an optimization problem of finding the global minimum of the distance function E . But since the relation between the input parameters and the distance function is quite complex and contains many local minima, standard optimization schemes such as gradient descent methods cannot be applied. Monte-Carlo based Heuristics like simulated annealing strategies are suited excellently to operate in such parameter spaces. While they are not guaranteed to find the global minimum, they are extremely efficient in finding solutions sufficiently close the global minimum, since their statistically nature allows them to escape local minima which would trap conventional gradient based optimization routines.

3.4.1 Simulated annealing

Briefly, simulated annealing uses a reasonable starting parameter set and randomly changes only one parameter like the sample-detector distance. Using this new set of parameters, the calibration measurement is converted in reciprocal space and a set of trail scattering vectors \mathbf{q}_t is obtained. Using the theoretical reference data set, the distance function E is evaluated. As an aside, in simulated annealing theory, E corresponds the energy of a system. Obviously, if the distance is decreased the new parameter set is accepted. However, in contrast to gradient based methods, even parameter set which yield higher distances can get accepted. However, only by a certain probability, as defined by the Metropolis-Hasting algorithm with r being a random number between 0 and 1 and ΔE being the difference in the distance function E between the best parameter set and the current trail set:

$$\text{accept if } r < e^{-\frac{\Delta E}{T(k)}} \quad (3.10)$$

$$\Delta E = E(\mathbf{q}_{\text{ref}}, \mathbf{q}_{\text{best}}) - E(\mathbf{q}_{\text{ref}}, \mathbf{q}_t) \quad (3.11)$$

This means, that with increasing ΔE a parameter set gets less likely to be accepted. $T(k)$ is a scaling factor, inspired by the temperature in analogy to real thermal annealing procedures. Higher temperatures make it more likely to accept worse parameter sets. Hence, at the start $k = 0$ the algorithm can easily overcome large barriers between local minima, thus exploring a large amount of the parameter space. However, over time the temperature T is decreasing, thereby confining the algorithm in hopefully reasonable areas of the parameter space until the algorithm converges.

The cooling strategy, thus $T(k)$, and the amount of necessary trail sets, depends mostly on the actual problem. In case of the detector calibration, a linear cooling strategy proved to be very efficient. Moreover, providing reasonable guesses for new parameters is crucial for the effectiveness of simulated annealing and needs to be tailored specifically to the problem. Reasonable parameter changes were only possible in small random increments obtained by a Gaussian distribution with a standard deviation of 1. Similar to the temperature, the standard deviation is decreasing linearly over time to maintain sensible changes to the parameters or otherwise most trail parameters sets will be rejected. Typically, an acceptance rate of 30% for the trail structures is recommended to guarantee

sufficient exploration of the parameter space and to ensure that the found solution is close to the actual global minimum. Often it is advisable to rerun the optimization with best-parameters of the first run to check for convergence.

In general, an arbitrary set of well-known reference data points could be used for detector calibration. However, for practical reason, it makes sense to use easy accessible calibration data such as provided by powder samples in the case of static detectors or the position of the primary beam for goniometer mounted setups. Depending on method (powder vs. primary beam), different pre-processing steps are required to obtain the necessary data sets for the calibration. Relying solely on data sets allows for a complete separation of the actual calibration logic and the experimental data acquisition.

3.4.2 Powder sample reference

Using a powder sample, a single detector image containing the powder diffraction rings is sufficient to obtain a trail scattering vector set \mathbf{q}_t . The reference data set \mathbf{q}_{ref} consists of the positions of the powder diffraction rings such for the NIST LaB₆ calibration standard SRM 660b. While the complete detector image could be used for the calibration it is usually not feasible from a computational point of view. Certain pre-processing steps are required to obtain a set \mathbf{q}_t of reasonable size.

A single detector image conversion into reciprocal, even for very large detector with approximately 2 megapixels, can be carried out typically in the range of 10 to 20 milliseconds. But during a calibration thousands of trail parameters sets are generated and all of which are used to transform the detector data in reciprocal space. Thus, the speed can be drastically enhanced by selecting only pixels with useful information i.e. pixel which are part of the diffraction rings. Furthermore, the background generated by air scattering or a glass capillary might interfere with calibration process. Firstly, due to the strong contrast in the appearance of the background (large diffuse rings) and the powder diffraction rings (sharp individual pixels), the background can be detected using an imaging opening operation. Image opening is used in digital image processing to remove noise or small object. In this case the actual diffraction data is removed, leaving only the background caused by diffuse air scattering. Subsequently, the background image is subtracted from the original image, to obtain

the undisturbed powder diffraction pattern (see Figure 3.10 left and middle). Due to the background removal, it is possible to select only pixel which are

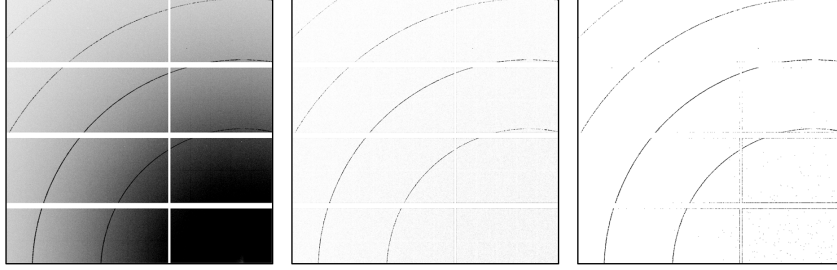


Figure 3.10: Individual processing steps applied to the calibration images. Left: Raw image with diffuse air scattering. Middle: Diffuse background removed. Right: Binary image after threshold filtering.

part of the diffraction rings by applying a threshold to the image based on the intensity. This threshold operation yields a binary image, containing 1s for pixels above the threshold, which will be located primarily on the diffraction rings (see Figure 3.10 right). Since the actual intensity of the diffraction rings is of little use for the calibration, it makes sense to use the binary diffraction image for the calibration itself. Unfortunately, pixels close to the edges of the individual panels of the detector show a similar intensity as the diffraction rings and are therefore selected by the threshold process. But these data points can be excluded easily in reciprocal space during the calibration by using a tolerance value. Usually, the initial guess for the detector parameters is sufficiently close the actual values that only trail scattering vectors within a reasonable distance to the theoretical positions ($\pm 0.1 \text{ \AA}^{-1}$) need to be considered (see Figure 3.12). Following the selection of the correct pixels using the threshold image and subsequent calculation of the trail scattering vector \mathbf{q}_t , the difference function can be calculated according to:

$$E(\mathbf{q}_{\text{ref}}, \mathbf{q}_t) = \sum_{i=1}^n ||\mathbf{q}_{\text{ref},i} - \mathbf{q}_{t,i}|| \quad (3.12)$$

Since the evaluation is based on powder data, it is sufficient to compare the magnitudes of $|\mathbf{q}_t|$ and $|\mathbf{q}_{\text{ref}}|$ during the calibration.

An exemplary LaB_6 powder calibration carried out at the ELETTRA synchrotron beamline XRD1 is presented in Figure 3.11 and shows the initial calibration run (top) and re-run for convergence check (bottom). The top two rows show the

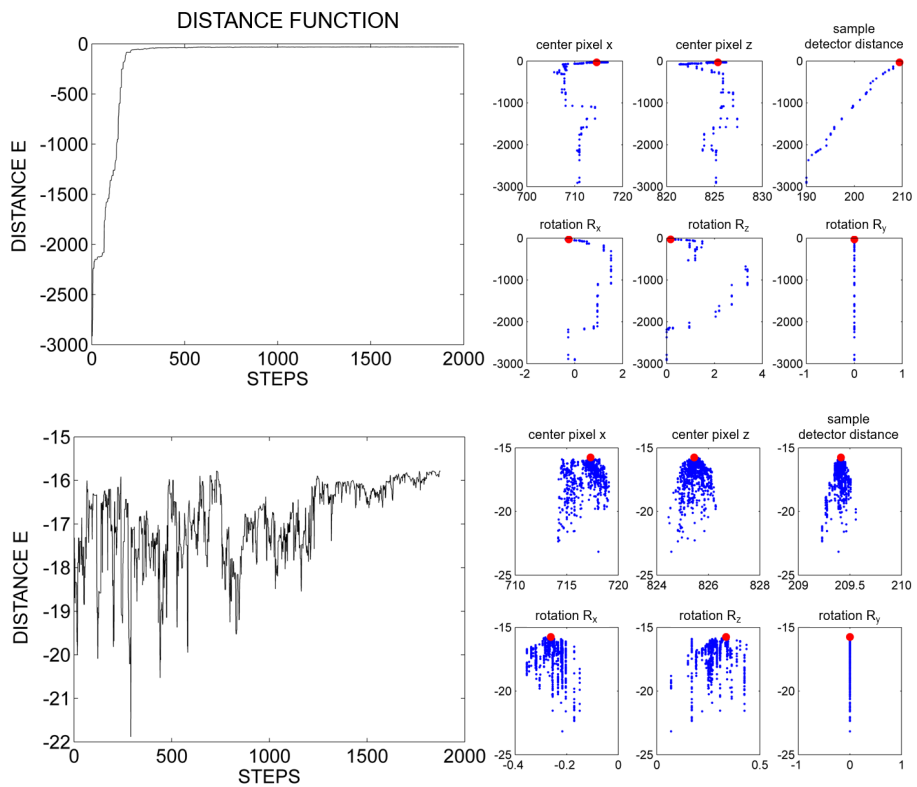


Figure 3.11: First (top) and second (bottom) run of a powder calibration. Left column shows the decreasing distance function E with processing optimization and right column shows the individual parameters probed by the simulated annealing algorithm. Red dots indicate the best parameter set with the lowest distance function value.

progression of the parameters during calibration and the bottom row the distance function E . For this example, rather bad initial conditions were chosen to illustrate the capabilities of the calibration process. The sample-detector-distance was set to 190 mm, roughly 20 mm off the correct position. As clearly seen in subplot SDD the algorithm improves mainly the sample-detector-distance d_{SD} , which closes in on the actual value of about 210 mm. This huge improvement causes a drastic decrease in the distance function E . Essentially, already after 5% of the total calibration steps a reasonable result is achieved, since the distance function has already converged. Another interesting aspect is the correlated movement of the center pixel position and the detector rotation as seen in subplot CPX (center pixel X) and RX (rotation around the x -axis). However, after trying various combinations the algorithm settles for the correct center pixel and only a minor rotation around the x -axis. The second run (right column) only confirms the convergence into a stable minimum, since the distance function E is basically only fluctuating, meaning new parameter sets are still explored but being similar or equal to the already obtained best parameter set. The rotation around the beam axis (RY) appears as a vertical line since it cannot be fitted with a powder sample and therefore is excluded from the calibration. Finally, the quality of the calibration is evaluated in reciprocal space, simply by plotting the theoretical Debye-Scherrer rings on top of the converted detector image as depicted in Figure 3.12, which should provide an excellent fit.

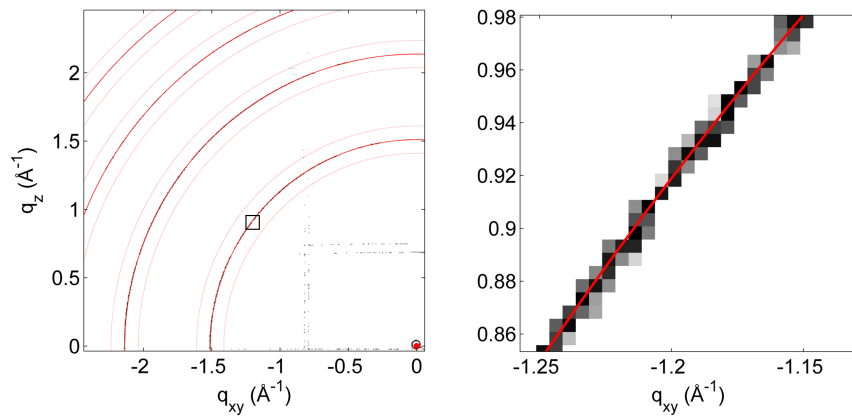


Figure 3.12: Result of a successful detector calibration using LaB_6 powder. Left: Thick Red lines indicate the theoretical position of LaB_6 powder rings. Thin lines indicate the tolerance level for the calibration (see main text). Red dot is

3.4.3 Primary beam reference

Using the primary beam for calibration follows the same idea as for powder-based calibration. The only difference is that the trail data set is generated by moving the goniometer arm to multiple ($n > 20$) positions δ and γ and the position of the primary beam is recorded on the detector. A similar approach based on the primary beam position is also published by Kriegner et al. and is available in the Python library *xrayutilites*.¹⁹ While the basic principle is similar, the actual detector parameter optimization is carried out differently.

Recording the primary beam means that each data point corresponds to $\mathbf{q} = 0$, thus this calibration approach does not depend on any reference material properties. The pixel position of the primary beam on each individual detector image can be easily determined using a peak fitting routine and pre-processing steps such as background removal and threshold filtering are not required. Subsequently these points are converted into reciprocal space taking the goniometer angles δ and γ into account and act as the trail scattering vectors \mathbf{q}_t allowing for the calculation of the distance function E according to:

$$E(\mathbf{q}_{\text{ref}}, \mathbf{q}_t) = \sum_{i=1}^n 0 - |\mathbf{q}_{t,i}| \quad (3.13)$$

Instead of optimizing the distance between theoretical and experimental Debye-Scherrer rings as for powders, only the distance to $\mathbf{q} = 0$ needs to be minimized.

One advantage of this method is that the detector rotation around the y -axis can be determined, which is impossible using powder calibration samples which are symmetrical with respect to this very axis. Moreover, the position of the primary beam can usually be determined with greater accuracy compared to powder rings. Also, the computational cost is reduced, since the amount of trail scattering vectors for each step is drastically reduced, which is beneficial since during a calibration thousands of trail parameters sets are generated. Nevertheless, in either case, efficient implementation allows for very fast calibration in the matter of seconds on contemporary personal computers.

In order to use these calibration routines efficiently, a MATLAB tool was developed capable of executing detector calibrations based on powder samples as well as the primary beam position.

4 Results

4.1 Complex behaviour of caffeine crystallites on muscovite mica surfaces²⁰



Complex Behavior of Caffeine Crystallites on Muscovite Mica Surfaces

Christian Röthel,^{*,†,§} Michal Radziown,[‡] Roland Resel,[§] Andreas Zimmer,[†] Clemens Simbrunner,^{‡,¶} and Oliver Werzer^{*,†}

[†]Institute of Pharmaceutical Sciences, Department of Pharmaceutical Technology, Karl-Franzens Universität Graz, Universitätsplatz 1, 8010 Graz, Austria

[§]Institute of Solid State Physics, Graz University of Technology, Petersgasse 16, 8010 Graz, Austria

[‡]Institute of Semiconductor and Solid State Physics, Johannes Kepler Universität Linz, Altenbergerstraße 69, 4040 Linz, Austria

[¶]Institute of Solid State Physics, University of Bremen, Otto-Hahn-Allee 1, 28359 Bremen, Germany

4.1.1 Preface

This work was conducted in close collaboration with Clemens Simbrunner and Michal Radziown who carried out the sample preparation. Structural X-ray investigations, atomic force and optical microscopy as well as data evaluation was performed by the first author. Data interpretation and the manuscript preparation was carried out by the first author as well with assistance of Oliver Werzer und Roland Resel. Andreas Zimmer advised on the pharmaceutical aspects and properties of caffeine. The provided text and illustrations are identical to the manuscript as submitted to *Crystal Growth & Design* and are reprinted with permission.

4.1.2 Abstract

Defined fabrication of organic thin films is highly desired in technological as well as pharmaceutical applications since morphology and crystal structure are directly linked to physical, electrical and optical properties. Within this work, the directed growth of caffeine deposited by hot wall epitaxy (HWE) on muscovite mica is studied. Optical and atomic force microscopy measurements reveal the presence of caffeine needles exhibiting a preferable alignment in the azimuthal directions with respect to the orientation of the defined mica surface. Specular X-ray diffraction and X-ray diffraction pole figure measurements give evidence that the β -polymorphic form of caffeine forms on the mica surface. All results consent that caffeine molecules have an edge-on conformation i.e. minimising their interaction area with the surface. Furthermore, the azimuthal alignment of the long caffeine needle axis takes place along the [1-10], [100], [110] real space directions of mica; needles are observed every 60° azimuthally. While mica has a complex surface structure with mirror planes and lowered oxygen rows, the slightly disturbed 3-fold symmetry dictates the crystal alignment. This is different to previous findings for solution cast caffeine growth on mica. For HWE the needles align along the mica main directions whereby solution cast needles result in a molecular alignment along certain directions.

4.1.3 Introduction

In recent years defined preparation of thin films has become highly desired since many technological applications or fundamental studies^{5,6,21,22} depend on the reliable and controlled fabrication of organic, inorganic or metallic thin films. The variation of process parameters such as temperature, pressure, deposition rate, and environment (e.g. solvent), allows engineering thin films with particular properties and morphologies.^{23,24} This in turn tunes for instance the optical^{25,26} and electrical properties.^{27,28} Especially the control of the solid state properties such as polymorphism^{29,30} or morphology are of outmost interest for pharmaceutical drug formulation since this is one of the decisive factors for drug release and resorption in living organisms (bioavailability).³¹

A well-established method for thin film preparation with high scientific but also industrial relevance³² is physical vapour deposition (PVD). Even though

PVD is especially appealing since the thin film preparation is carried out under specific environmental conditions, such as ultra-high vacuum or in inert gas atmosphere, it is hardly recognised in pharmaceutical science. Anyway, PVD as a solventless process allows for limiting the interaction during crystal growth to solely molecule-molecule and molecule-substrate interactions which helps to identify the underlying growth mechanisms. More importantly, contingent interactions for example with solvents or ambient atmosphere (especially with surface water), are mostly avoided during film formation easing the understanding of heterogeneous crystal growth. Despite the process parameters, the choice of substrate has a strong influence on film formation and crystal growth. During crystallisation, interactions of the organic molecules with the substrate surface due to van der Waals forces, H-bonding and/or electrostatics play a decisive role.³³ It was demonstrated previously, that crystallisation in proximity of solid surfaces is able to increase the crystal yield, aid the growth of certain polymorphs³⁴ and/or induce directional growth.³⁵ Moreover, surfaces are able to stabilise certain fragile polymorphs³⁶ for a prolonged timespan or induce/mediate new polymorphs which are not accessible by conventional bulk methods.³⁷ Typically substrates are classified based on their surface properties. Isotropic surfaces contain randomly arranged atoms at the solid–air interface without long-range order. Generally, such surfaces are only capable of selecting a preferred contact plane of a molecular crystal during a PVD process resulting in azimuthally randomly distributed crystals on the surface.¹⁰ In contrast, highly anisotropic surfaces are present, for instance, in rubbed polymer surface³⁸, or outer/cleaved surfaces of single crystal minerals, salts, inorganics, metals, or others. Some of the most prominent examples for such surfaces are mica, NaCl, silicon, or gold. The particular periodic arrangement at the surface depends on the chemical composition and their ability to rearrange. For instance different cutting direction of the crystal results in altered surface properties which in turn might facilitate the heterogeneous crystal growth.³⁹

Many PVD studies on thin film growth focus on synthetic, highly symmetric, conjugated organic molecules due to their importance for application in organic electronics.^{40–43} However, most drug molecules feature asymmetric chemical structures with quasi ambipolar character. This accounts on the one hand for aqueous solubility, on the other hand, dependent on its partition coefficient (log P), the ambipolarity allows for cell membrane penetration.⁴⁴ In order to study the growth of such asymmetric molecules on a solid surface, caffeine is an ideal

model candidate as it is widely used in pharmaceuticals as pure active pharmaceutical ingredient (API), as excipient in pain killers and as a co-crystallisation agent for various molecules.^{45–47} The purification of caffeine prior usage is typically obtained from recrystallisation via sublimation. Since low process control is required during purification, the knowledge of caffeine recrystallisation in a PVD process is rather limited.⁴⁸ Anyway, there are studies of caffeine on various surfaces deposited from solution, showing the growth of either needle-like morphology or plate-like hexagons with the surface having a decisive impact on the crystal alignment.^{49,50} Previous studies on solution cast samples show that caffeine deposited onto mica surfaces results in an alignment of caffeine with respect to the underlying mica surface.⁵¹

There are many PVD processes described in literature ranging from simple vacuum apparatus to very sophisticated ultra-high vacuum chamber assemblies.⁵² For organic thin films, a hot wall epitaxy setup (HWE)⁵³ is well suited since it works close to thermodynamic equilibrium and facilitates the growth of van der Waals bonded systems.⁵⁴ In the case of caffeine a reduction of the pressure is not required as heating of caffeine to 120 °C at ambient pressure results in excessive sublimation. Furthermore, having an inert gas along the heated deposition cone (hot wall) at ambient pressure is sufficient to achieve caffeine films of very high quality. Mica is used in this study as it is atomically flat and is furthermore capable of aligning molecules along specific directions as reported for various organic systems.^{35,51} The resulting thin films will be investigated by microscopy and X-ray based techniques allowing the caffeine crystallisation at the surface to be understood. Similarities or differences to caffeine crystal growth on mica by solution casting are elucidated.

4.1.4 Experimental Methods

Materials. Samples were prepared on muscovite mica (001) substrates (grade V-4) purchased from SPI Supplies (West Chester, USA). All substrate surfaces were cleaved freshly and immediately transferred into the HWE chamber. Caffeine (pharmaceutical grade) was purchased from Herba Chemosan-AG (Vienna, Austria) and used without further treatment.

Sample preparation. Prior deposition the mica substrates were preheated for 30 min at the desired substrate temperature of 65 °C to ensure thermal stability.

After preheating, a shutter was opened and the mica surfaces were exposed to the molecular flux for 5, 10, 15 and 20 minutes. Optimal temperature setting of 125 °C for the source and 130 °C for the wall have been obtained and kept constant for all depositions in this study. X-ray diffraction experiments. Specular X-ray diffraction (SXRD) measurements were performed on a PANalytical EMPYREAN reflectometer fitted with a Cu sealed tube ($\lambda = 1.54 \text{ \AA}$), a $1/32^\circ$ primary slit, a 10 mm beam mask and a multilayer mirror on the primary side. On the secondary side a slit system containing a 0.1 mm receiving slit and 0.02 rad Soller slits defined the diffracted beam. The intensities as function of the scattering angle were recorded using a 3D PANalytical PIXCel detector.

X-ray pole figures (XRPF) were performed on a Philips X'pert diffractometer using a chromium sealed tube and secondary graphite monochromator ($\lambda = 2.29 \text{ \AA}$). Pole figures were recorded for a fixed scattering vector $|\mathbf{q}|$ in Schultz reflective geometry.⁵⁵ Shortly, an X-ray diffraction pole figure contains information about the spatial distribution of specific net planes with respect to the substrate surface. During the measurement the sample is rotated around the Eulerian angles ψ (inclination of the surface normal) and φ (rotation around the surface normal). The intensity data is presented in polar contour plots with ψ being the polar radius and φ the polar angle. Spots with enhanced intensity (poles) correspond to Bragg reflections which are caused by net planes which fulfil the Laue condition, meaning the corresponding net planes are normal to pole direction. Experimental data was visualised and evaluated using the software STEREOPOLE.¹⁸ Morphological investigation. Optical microscope images were taken with an Axiovert 40 microscope (Zeiss, Germany) equipped with a high resolution digital camera. Atomic force microscopy (AFM) height measurements were performed using a FlexAFM and Easyscan 2 controller (Nanosurf, Switzerland) to gain knowledge on the topography of the samples. The images were taken in tapping mode using a Tap190 cantilever (Budget-sensors, Bulgaria) with a nominal frequency of 190 kHz. Subsequently, the recorded images were corrected for artefacts and visualised using the Gwyddion software.⁵⁶

4.1.5 Results

Morphology. Caffeine was deposited by means of HWE on freshly cleaved muscovite mica (001). Various samples were prepared whereby the process

conditions remained the same (substrate and wall temperature) except the molecular flux exposition time varying from 5 to 20 min. All samples reveal a very similar behaviour with elongated needle-like structures being present at the mica surface (see Figure 4.1 and 4.2). At a deposition time of 20 min 'broad' flat needles are present at the mica surface with extension of up to 100 μm along the long needle axes. The width of the structures has a strong variation from 10 μm down to approximately 1 μm . A closer inspection reveals that individual needles consists of smaller elongated structures packed closely together (see Figure 4.6). The needle height of approximately 100 nm is similar over the entire sample. Beside the broad structures thin needles of significantly higher extension exist on the sample surface (visible as brighter whitish needles). The amount of those in the selected sample is relatively low.

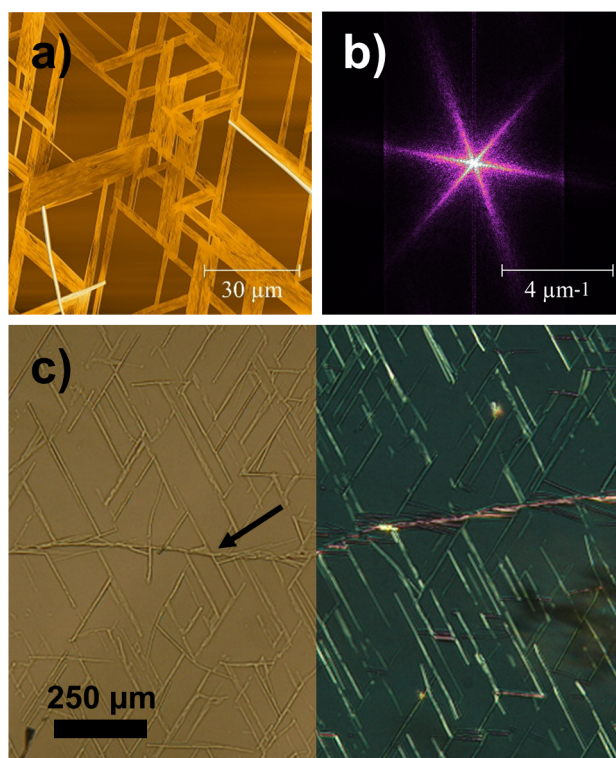


Figure 4.1: a) Atomic force microscopy (AFM) height image of caffeine crystallites on a single mica domain. b) Fourier transform of the AFM image. c) Optical micrograph without (left) and with crossed-polarisers (right) showing caffeine on two separate mica domains (black arrow indicates cleavage step).

Besides the needle morphology, the AFM image reveals that all needles at the surface align along defined directions with 60° or 120° inclination to each other.

This is further supported by a 2D-FFT of this image which shows six streaks, every 60° on a 360° turn (see Figure 4.1b). This means three directions (or six if the 180° is taken into account separately) are present on the mica surface which facilitate the alignment of the caffeine needles. As the mica surface may consist of two domains of 120° inclination⁴⁰ an additional optical micrograph (with and without crossed-polarisers) showing a cleavage step between such domains was taken (Figure 4.1c). Although crossed-polarisers enhance the contrast of crystalline species, they also select needles depending on their orientation cancelling certain directions in the image (compare Figure 4.1c, left and right side). Anyway, the images reveal that in each domain all six directions are present which shows that the 60° symmetry is a result of caffeine aligning within one mica domain in all these directions. While most of the needle structures align consistently with defined angles, some needles with mismatched directions are noted (for an example see Figure 4.1a, lower left corner and Figure 4.1c, middle). Such needles occur due to nucleation at cleavage steps or other defects in the surface inducing growth in a direction mismatching the pattern.

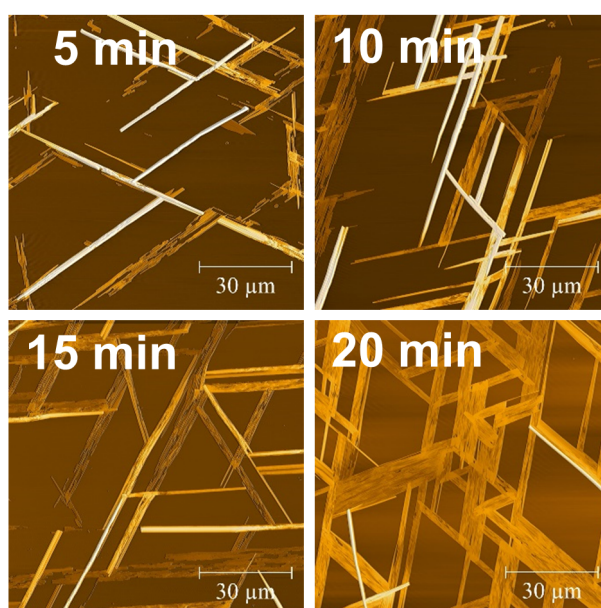


Figure 4.2: AFM images of caffeine crystallites on muscovite mica for various deposition times at 65 celsius substrate temperature.

On the change of deposition time the qualitative picture of caffeine on mica remains the same. At 5 min deposition time most of the caffeine assembles in

the thin needle morphology with a height of typically 200 nm. Flat structures are present but compared to the 20 min sample these structures are strongly fragmented. Doubling the deposition time reveals that the flat structures coalesce and more interconnection points appear. At 15 min the ratio of thin and flat needles decreases, meaning that the amount of both become similar. At 20 min, the flat structures are most common.

Specular X-ray diffraction experiments. To gain more insight into the crystallographic properties of caffeine on mica, X-ray based studies were performed. The specular X-ray diffraction pattern of the sample with 20 min deposition time is given in Figure 4.3. The region around 8.4 nm^{-1} is shown as this region corresponds to locations for which the most prominent net planes of caffeine are expected. The diffraction pattern of the sample shows two peaks located at $q_z = 8.34 \text{ nm}^{-1}$ and 8.49 nm^{-1} , respectively while other peaks are not noted. The experimentally observed peaks correspond to a d -spacing of 0.75 and 0.74 nm, respectively. Since caffeine may exist in two polymorphic forms, the stable β -phase⁵⁷ (CSD code: NIWFEE03) and the meta-stable α -phase⁵⁸ (NIWFEE02), the peaks were compared to both crystal structure solutions, revealing an excellent match with the (020) and (510) net planes of caffeine in β -conformation.

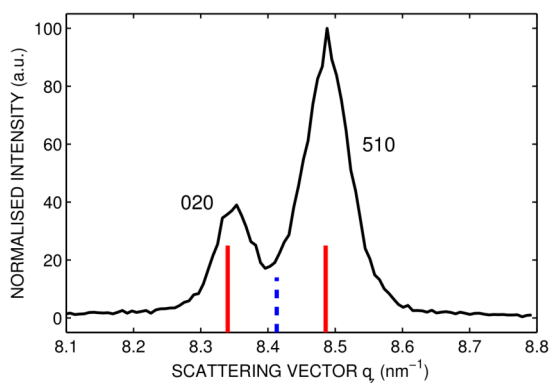


Figure 4.3: Specular X-ray diffraction scan of caffeine on mica. Calculated peak positions for the β (red, solid) and α (blue, dashed) polymorph are indicated.

Due to the experimental geometry, a specular X-ray diffraction scan is only able to measure inter planar spacings (d -spacings) of net planes parallel to the substrate surface, thus the two peaks show that the sample contains various types of crystallites which differ in their contact planes; one has a (020) and the other has a (510) contact plane (i.e. these net planes are parallel to the

surface).

The preparation of caffeine samples at elevated temperature might facilitate the formation of a less stable high temperature polymorph.^{59,60} A Bragg peak due to presence of the less stable α -form would be expected at $q_z = 8.41 \text{ nm}^{-1}$, between the β -phase peaks. Anyway this is not the case for samples prepared within this study (compare Figure 4.3), hence further explanations in this text are based on the β -polymorphic form and their behaviour.

A comparison of the specular X-ray diffraction data for samples prepared with different deposition times reveals very similar diffraction patterns for all. The roughly constant intensity ratio of the 020 and 510 peaks indicates that the deposition time has no significant influence either on the selection of the contact plane nor the polymorph (measurements are provided in the supplementary information). Despite the difference in the amount of thin and flat needles for the various samples, it cannot be concluded that each of the species has a different contact plane since the relative peak heights seem unaffected by this fact. Thus it seems to be equally likely that both planes, (020) and (510), have a certain probability to contact the surface.

X-ray pole figure experiments. The presence of the small number of Bragg peaks in the specular X-ray diffraction scans typically means that a preferred crystal alignment is present. This is further supported by microscopy investigations which even suggest that a bi-axially alignment could have taken place during crystal growth. For the crystallographic investigation of such samples the X-ray pole figure technique is best suited. Within such a pole figure measurement the scattering vector \mathbf{q} is fixed (thus a specific d -spacing and its corresponding net planes is selected) while the sample is rotated (φ) and/or tilted (ψ). High intensity (poles) occurs in this experiment for crystallites aligning in a proper direction fulfilling the Laue condition and consequently the intensity distribution allows for the integral crystallographic arrangement of crystals on the sample to be identified.

Pole figure measurements for two scattering vectors performed at the thickest sample (thus giving the most diffracted intensity) are shown in Figure 4.4. In Figure 4.4a the pole figure measured at $|\mathbf{q}| = 8.4 \text{ nm}^{-1}$, thus selecting net planes with inter planer spacings of approximately 0.75 nm , reveals seven poles, which considering the low resolution at this $|\mathbf{q}|$ -value must be a result of either the 020 or 510 Bragg reflections fulfilling the Laue condition. In the

centre of this pole figure ($\psi = 0^\circ$) the high intensity results from the net planes which are parallel to the substrate surface. According to the specular X-ray scans it needs to be the (020) or (510) plane. Away from the centre six other poles are present. All these poles are located at a common inclination ($\psi = 60^\circ$) to the surface normal. In the azimuthal direction poles are located at $\varphi = 30, 90, 150, 210, 270$ and 330° , meaning that each pole is rotated by 60° with respect to its adjacent. This is in excellent agreement with the Fourier transform (see Figure 4.1b) of the AFM image which also showed streaks with an azimuthal rotation of 60° . This suggests that the pole figure is a result of six needle growth directions.

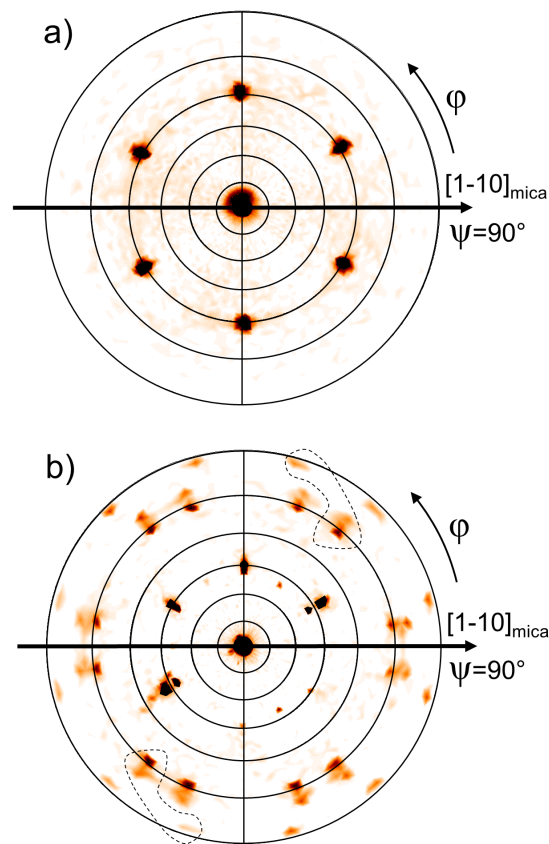


Figure 4.4: X-ray pole figures of caffeine on mica measured at a scattering vector $|\mathbf{q}| = 8.4 \text{ nm}^{-1}$ (a) and 19.0 nm^{-1} (b). Summarised poles within the dashed regions appear regularly due to crystallites of different azimuthal orientation. Solid black line indicates the mica mirror symmetry direction.

To gain further information about the sample an additional pole figure at $|\mathbf{q}| = 19.0 \text{ nm}^{-1}$ was recorded (Figure 4.4b). At this scattering angle inter planar

distances of about 0.33 nm will produce poles on the fulfillment of the Laue condition. A comparison with the crystal structure shows that net planes with $hkl = \{60-2\}$, $\{11-2\}$ (curly brackets indicate all permitted permutations of hkl) are measured. In the middle of the pole figure ($\psi = 0^\circ$) the peak corresponding to the mica (006) net plane is present. At inclination angles of $\psi = 45^\circ$ six poles are noted which are also a result of the substrate. The various peaks at $\psi = 75, 80$ and 88° correspond to caffeine and can be explained by one unique repetitive pattern (indicated by dashed region). This pattern is repeated every 60° in azimuthal direction which is again in well agreement with the observed needle directions which are also separated by 60° .

4.1.6 Discussion

The crystallisation of caffeine in solution results in needle type morphology in the β -phase. On heterogeneous crystallisation from solution two morphologies are typically evident, with long needles and the extended hexagonal structures.⁴⁹ The investigation of caffeine on mica surface prepared via HWE reveals similarly to bulk solutions solely needle type structures of caffeine in β -phase. Indication of another polymorph, especially the metastable α -phase was not noted, hence crystallisation on mica is similar to the bulk.

Muscovite mica has a rather complex crystalline structure.^{35,61} However it provides a highly ordered surface structure due to weakly bond aluminium-silica sheets. By cleaving along these sheets, relatively large areas of atomically flat and clean (001) surfaces can be obtained. Adjacent mica sheets are very much alike, but one (α -mica) is rotated by 120° with respect to the other sheet (β -mica). Typically, a sample of cleaved mica surface consists of several individual domains with each containing just α or β mica (see Figure 4.1c). The surface unit cell of the α -domain exhibits a mirror symmetry along the mica [110] direction and a slight corrugation due to slightly lower oxygen along the same direction (for the β -sheet everything is equivalent, but rotated by 120° with respect to the α -sheet).⁴⁰ Strictly speaking, a mica surface has only a mirror symmetry but allowing for some deviations one could easily identify a pseudo-3-fold symmetry arrangement of the oxygen atoms at the surface.⁶¹ From this simple consideration it follows that for directed growth along the oxygen grooves only one crystal direction should be present in a domain. For growth that is affected by the mirror symmetry two directions should be noted

while 3-fold symmetry means that most likely the nearly hexagonal oxygen arrangement in the surface is responsible for the molecular alignment. The AFM and optical measurements clearly show that six needle directions are present. Furthermore these six directions are present in their close vicinity (~couple of micrometer), meaning these six growth directions are present in one single mica domain. This is further supported by optical microscopy which clearly allows to separate the domains with each containing six caffeine directions. Thus the needle growth is a result of caffeine crystals aligning on the account of the slightly disturbed 3-fold 'oxygen symmetry' in the mica surface.

In order to obtain information on the crystallographic orientation of the caffeine needles with respect to the mica surface, each pole in Figure 4.4 is indexed i.e. each pole gets assigned a corresponding net plane (hkl). The poles observed in Figure 4.4a are limited to net planes of the {510} and {020} family due to the fixed scattering vector of $|\mathbf{q}| = 8.4 \text{ nm}^{-1}$. The centre peak ($\psi = 0^\circ$) in the pole figure, as already established by specular diffraction experiments, corresponds to the (510) and/or (020) net planes. Since crystallites with those contact planes have very similar *d*-spacings, 0.753 and 0.740 nm, respectively, it was not possible to separate both contribution due to the limited resolution of the setup in use. However, for the sake of simplicity it is assumed that only needles with a (510) contact plane are present. In the supporting information an alternative indexation using a (020) contact plane is provided.

In Figure 4.5b the inclinations (ψ in the pole figure) of the (5-10) and (020) net planes with respect to the (510) contact plane is illustrated. As clearly seen, the inclination angles of the (5-10) and (020) with respect to the contact plane are in the case of caffeine extremely similar (58.9° and 60.6° , respectively) and explains the common inclination of the poles of approximately 60° . While the inclinations are defined by the net planes within a crystallite, the azimuthal angle φ depends on the direction of the crystallite on the surface. Therefore to obtain a proper description of the pole figure, it is necessary to find the correct azimuthal orientation by rotating the crystallite around its contact plane normal until the calculated poles match the spots of enhanced intensities in the pole figure.

However using just one crystallite of a specific orientation gives only two poles, as indicated by different colours in Figure 4.5a. To get a complete description of the pole figure, at least two additional crystallites with different azimuthal

alignment need to be introduced (blue, green). Each crystallite is rotated azimuthally by 60° with respect to each other. These crystallites with distinct directions are in excellent agreement with six different needle directions as seen in optical and AFM micrographs (compare Figure 4.1). As mentioned earlier, a (020) contact plane would yield a similar result. This becomes quite obvious, if one considers a clockwise rotation of the crystal by 60° along the needle axis. The (020) plane would become the contact plane with the mica surface (parallel to the surface) and consequently the (510) is then 180° rotated in φ with respect of the (5-10) plane and both are found at a common inclination of 60° .

The pole figure taken at $|\mathbf{q}| = 8.4 \text{ nm}^{-1}$ can be understood in the crystals having a (020) or (510) contact plane with the surface. However the unit cell equivalent contact planes should exist with the hkl of, for instance (0-20) and (-510). While this cannot be proved at the measurement taken at $|\mathbf{q}| = 8.4 \text{ nm}^{-1}$ the pole figure taken at $|\mathbf{q}| = 19.0 \text{ nm}^{-1}$ allows for a clarification. At various ψ values larger than 70° twelve poles at defined φ values are present which can be paired to six groups. Each group is rotated by 60° of another. Within a group a splitting exists, for instance 18° at $\psi = 75^\circ$. This group splitting is a result of some caffeine having a (510) and some other having (5-10) contact plane. The monoclinic angle $\beta = 99^\circ$ of the caffeine unit cell accounts for such a splitting on inverting the crystal, thus proofing that more than two contact planes are required to understand the caffeine growth on mica. For sake of completeness, a more detailed description of the indexation is provided in the supplementary information.

Having the pole figure indexed, provides the opportunity to see the crystallographic relation of the caffeine unit cell with the mica surface. In the caffeine unit cell the disk-like molecules stack onto each other along the a and b -axis in an edge-on conformation while a parallel stacking similar to a π - π stacking is formed along the c -axis. The latter, so the c -axis, is also identical to the morphological needle axis of caffeine. From the pole figure it follows that the c -axis of caffeine points towards $\varphi = 0^\circ, 60^\circ, 120^\circ$ as well as $180^\circ, 240^\circ$ and 300° , giving basically six crystallographic growth directions. However, only three morphological directions are observable within the AFM; needles which are inclined by 180° cannot be distinguished. Furthermore, for all azimuthal directions the c -axis points towards $\psi = 90^\circ$, meaning the c -axis is parallel to

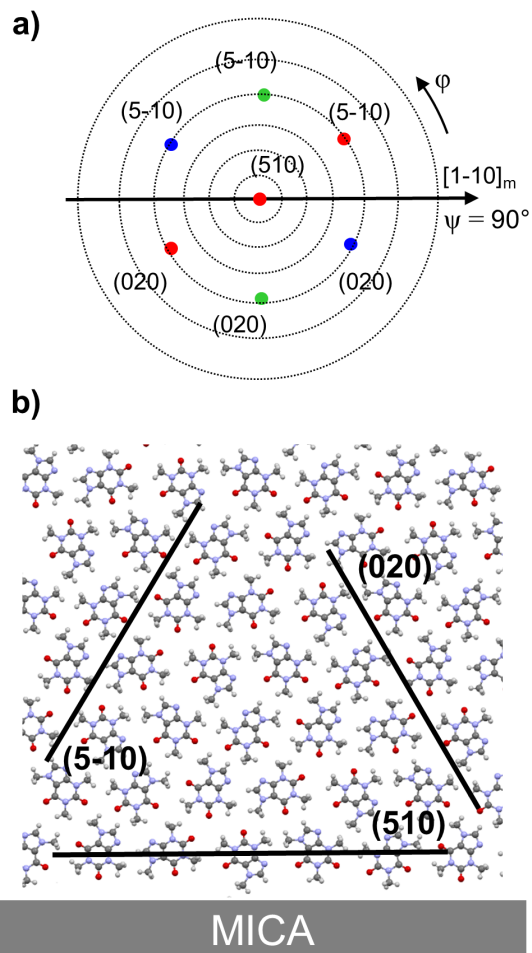


Figure 4.5: a) Simulated pole distribution for poles observed at $|q| = 8.4 \text{ nm}^{-1}$ using three crystals (red, green, blue) with (510) contact planes. b) View of a caffeine crystallite along the c -axis (long needle axis) with (510) contact plane. Black lines illustrate the projection of the (510), (5-10) and (020) net planes.

the surface. A comparison of these directions with the main directions of a mica surface, i.e. [1-10], [100], [110] shows that the long needle axis (*c*-axis) coincides with this main directions supporting the fact that the pseudo 3-fold symmetry of the mica surface dictates the caffeine crystal growth (see Figure 4.6). This is in agreement with the previous assumption derived from the morphological investigation, but now with the interpretation of the pole figure also the crystallographic information is accessible.

The *a*-axis of caffeine is also in-plane as long as the contact plane is a (020). However a common azimuthal direction with the underlying mica substrate is not observed. For the (510) contact plane the *a* and *b*-axis do not coincide with any mica main direction. Regardless of the contact plane, the *c*-axis remains unaffected, meaning that the azimuth of the needle axis is well aligned while there is some freedom for the contact plane to be chosen. On a closer inspection of the molecular arrangement within the unit cell shows that (020) and a (510) plane have a very much alike caffeine assembling with the surface; 'edge-on' with slightly rotated adjacent molecules. This also suggests that the energy for both situations is very similar, meaning no preferential growth of either (020) or (510) crystallites takes place.

The heterogeneous nucleation and crystallisation at a solid surface is a complex process. Typically an individual molecule adsorbs on the surface most likely such that the caffeine molecule is lying flat. From simple energetic considerations a single flat-lying molecule should be energetically favoured as the Van der Waals interactions allow to minimise the energy more effectively. As time progresses more molecules accommodate in the vicinity. Anisotropic molecular diffusion along the surface allows for nucleus formation and further crystal growth. In the case of caffeine, the crystals have an edge-on conformation of upright standing molecules, thus limiting their interaction with surface to the terminal methyl groups and/or oxygen atoms. It seems that the increased energetic cost of several upright standing molecules is outweighed by an overall smaller energy of the well aligned crystals.⁶² Furthermore, the investigation show that the molecules align perpendicular to the mica main directions. At this stage it is not clear if the nucleation and crystal growth takes place already in that very confinement or if a rearrangement of the nucleus or crystal takes place. Anyway, there are many theoretical consideration trying to explain such a situation like lattice match or density functional theory calculations. Typi-

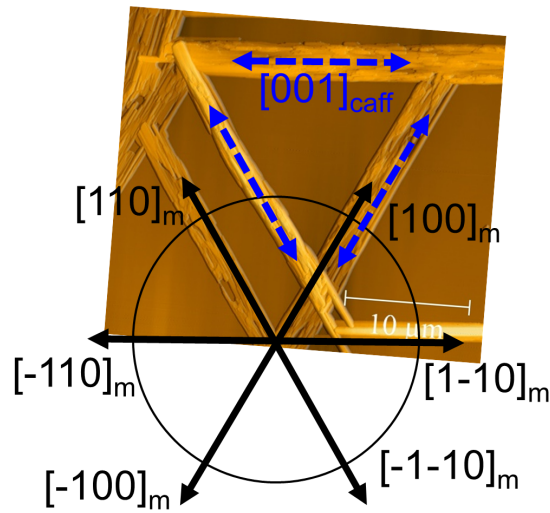


Figure 4.6: Atomic force microscopy image showing the relation between the azimuthal alignment of caffeine crystallites (blue arrows indicate c -axis) and the mica real space directions (black arrows).

cally, many pre-assumptions have to be taken into account for such a theoretical approach which makes a possible explanation of caffeine on mica via such tools challenging.

Surprisingly, the growth of mica on caffeine via HWE reveals a distinct crystal alignment obtained from solution cast films. Firstly, HWE facilities predominantly the growth of crystallites with $\{510\}$ and $\{020\}$ contact planes, while solution processing shows additional $\{110\}$, $\{520\}$ and $\{530\}$ contact planes. This means the solution cast crystallites have some rotational freedom along the c -axis, i.e. allows for rotation of those. Other than the (510) and (020) contact planes which provide "flat crystal cuts" (compare Figure 4.5) these additional contact planes might develop facets. The second surprising difference is the alignment of the caffeine crystal axes with respect to mica. In the case of HWE the c -axis, which defines the long needles axis, is aligned along the mica main axes regardless of the contact plane. The solution processing lead to an alignment of the a -axis, thus the c -axis does not coincide with any mica main direction. On one hand this means that caffeine deposited via HWE only shows six growth direction while solution cast have another six which are inclined by 18° to the others. On the other hand this also means the disk-like caffeine molecules stand perpendicular to the mica main axes for the HWE sample whereas the molecules stand parallel in the case the solution cast. The

reasons for the appearance of these differences could be manifold. The preparation route seems to play an important role, since the different alignments were observed exclusively on either type of sample. The main difference between these preparation techniques might be the solvent during the adsorption, nucleation and subsequent crystal growth. It might cause other sticking/adsorption sites at the mica surface to be facilitated. However, also other factors might account for this deviation such as the elevated substrate temperature during HWE, which changes the diffusion/sticking behaviour of molecules on surfaces. Furthermore the time scale of crystal growth differs drastically. In the case of HWE the caffeine deposition takes up to 20 minutes and is carried out very close to thermodynamic equilibrium. In contrast, deposition from solution, using especially a fast evaporating solvent such as tetrahydrofuran, is approximately one to two orders of magnitude faster. It is well established that kinetics have a decisive impact on crystal growth and might even prevail free energy minimisation.

4.1.7 Conclusion

Depositing anhydrous caffeine on muscovite mica using hot wall epitaxy (HWE) facilitates the growth of the typical needle-like caffeine crystals along six azimuthal directions with respect to the surface. The needles show an inclination of 120° with respect to each other which is attributed to the slightly disturbed 3-fold symmetry of the underlying mica surface. While this is obvious from simple microscopy images, pole figure measurements reveal a more detailed picture. The long needle axis, defined by the crystallographic *c*-axis, aligns along the [1-10], [100], [110] real space directions of mica. This means, the disk-like molecules are oriented upright standing ('edge-on') with respect to the surface and perpendicular to the aforementioned mica directions. Such directed crystal growth along preferred directions means that the interaction of the regular mica surface and the periodic structure provided by the molecules within the caffeine crystallites is most likely energetically favoured along these directions.

The aspect of *c*-axis alignment is of particular interest when compared to a previous study on solution cast caffeine on mica since an alignment of the *a*-axis was achieved by this preparation route. The difference in alignment has an immediate impact on the observed needle directions. For HWE processed

needles the long needle axis always points in the same directions as the aligned *c*-axis independent of the crystal orientation (e.g. flipping a crystal), while an *a*-axis alignment gives additional needles directions since the *a* and *c*-axis are inclined by approximately 9° due to the monoclinic unit cell of caffeine. Whereas both methods, HWE and solution casting, yield similar needle-like morphologies, the actual molecular interaction and arrangement with respect to the surface is surprisingly different, showing that further studies regarding the process parameters such as solvent, surface and temperature are essential to gain further understanding of the complex behaviour of asymmetric molecules on solid surfaces.

4.1.8 Acknowledgments

The work was funded by the Austrian Science Fund (FWF): P25541-N19 and P25154-N20. The authors gratefully acknowledge support from NAWI Graz.

4.1.9 Supplementary Information

Influence of deposition time on crystal properties of caffeine films

The scattering power of organic thin films is compared to extended single crystals extremely small which makes diffraction experiments on thin films such as X-ray pole figure measurements challenging. In order to obtain a sufficient signal to noise ratio one can increase the integration time of the detectors and/or increase the scattering volume e.g. deposit more material onto the surface. Increasing the integration time might be simple but can make pole figure measurements too time consuming. Hence, films should provide a certain scattering volume for reliable and efficient pole figure measurement which in general is easily possible.

However, many organic systems, most prominently pentacene, exhibit a different polymorphic behaviour in proximity of a substrate surface. Often, the formation of a surface induced phase (SIP) is observed which gradually changes into the thermodynamically stable bulk phase with increasing film thickness limiting the scattering volume of the interface region again.³⁷ This thickness

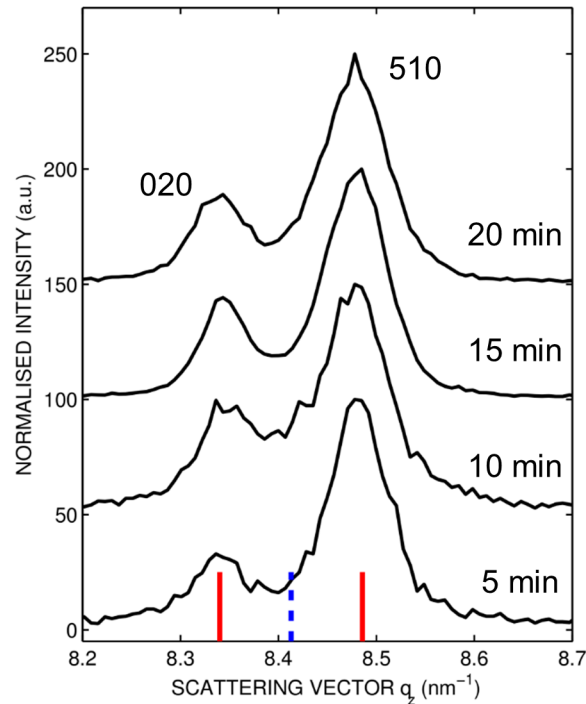


Figure 4.7: Specular X-ray diffraction scans of caffeine on muscovite mica for various deposition times at 65 °C substrate temperature. Calculated peak positions for the β (red, solid) and α (blue, dashed) polymorph are indicated by corresponding lines. Curves are normalised and shifted for clarity.

dependent polymorphism makes it necessary to carefully evaluate film characteristics (polymorphic phase, contact planes ...) as a function of thickness to be able to identify all scattering contributions from the interface. Figure 4.7 shows specular X-ray diffraction patterns of caffeine deposited by hot wall epitaxy (HWE) on muscovite mica for 5, 10, 15 and 20 min at 65 °C substrate temperature.

As the amount of material is increased the scattering volume enhances thus the peak height increases as function of deposition time. However, to make the measurements comparable each curve is normalised and slightly shifted. This pattern shows that with increasing deposition time the peak shapes get smoother which corresponds to an improved signal to noise ratio due to the increased diffraction power of thicker films. The peak positions show that both peaks corresponds to caffeine β -form⁵⁷, with the 020 peak at $q_z = 8.34 \text{ nm}^{-1}$ and the 510 at $q_z = 8.49 \text{ nm}^{-1}$. A formation of the high-temperature caffeine α -phase was not observed. Furthermore, the ratio of the 020 and 510 peak

is independent of the deposition time, meaning crystallites with both contact planes form equally over time at the mica surface. Considering all this facts, shows that increasing the deposition time changes only the amount of caffeine but does not influence the texture, polymorphic behaviour or other film characteristics at the tested samples. This shows that it is sufficient to use either of this samples as each should provide similar crystallographic information.

Alternative indexation of the pole figure at $|q| = 8.4 \text{ nm}^{-1}$

As mentioned in the main text, it is not possible to distinguish between a contact plane of the $\{020\}$ and $\{510\}$ net plane family due to their similar inclination angles and the limited resolution of the X-ray diffractometer in use. In the main text a (510) contact plane is assumed allowing all spots to be explained. Anyway, in Figure 4.8 an alternative indexation using a (020) contact plane is provided. Due to the change of contact plane, the corresponding poles at $\phi = 60^\circ$ are indexed as the (-510) and (510) net planes. Despite having different contact planes belonging to the $\{510\}$ and $\{020\}$ family, also an additional azimuthal rotation by 180° of the crystallites, meaning the (510) and (-510) pole would switch their positions, also generates a valid indexation. However, all indexations are morphological similar, i.e. the arrangement of the molecules and the caffeine needles are unaffected by these other indexations.

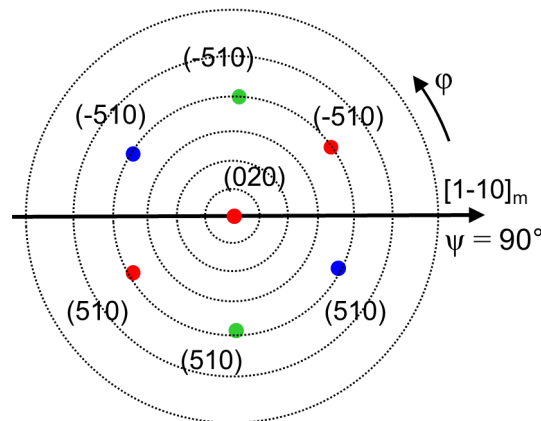


Figure 4.8: Pole indexation at $|q| = 8.4 \text{ nm}^{-1}$ using three crystallites (red, green, blue) with (020) contact planes.

Indexation of the pole figure at $|\mathbf{q}| = 19.0 \text{ nm}^{-1}$

The pole figure taken at $|\mathbf{q}| = 19.0 \text{ nm}^{-1}$ is more complex compared to the previous one with poles distributed at $\psi > 75^\circ$ at various φ angles (see Figure 4.4a). In order to index this pole figure one has to consider several aspects. Firstly, the pole figure at $|\mathbf{q}| = 19.0 \text{ nm}^{-1}$ is sensitive to Bragg reflections caused by net plane families of $\{-602\}$ and $\{-112\}$. Secondly, crystallites with multiple contact planes belonging to the $\{020\}$ and $\{510\}$ net plane family are present. Since the pole figure at $|\mathbf{q}| = 8.4 \text{ nm}^{-1}$ and the microscopy images already identified six azimuthal crystal directions, a complete description of this pole figure will again require the consideration of all directions.

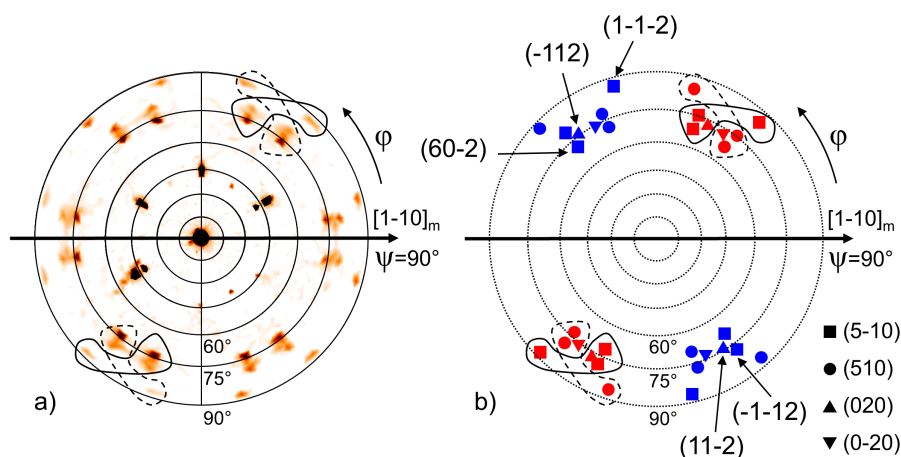


Figure 4.9: a) X-ray pole figure recorded at $|\mathbf{q}| = 19.0 \text{ nm}^{-1}$. b) Corresponding pole figure indexation. Markers indicate different contact planes, colours represent azimuthal directions (third direction omitted for clarity). The solid black line indicates the mica surface mirror symmetry.

Obviously, the complete crystallographic information is already contained in a single azimuthal direction i.e. the position of the Bragg reflections from all aligned crystals, is already contained in a single azimuthal direction. Hence other directions can be obtained by rotating the established pattern by 120° and 240° . Figure 4.9 shows the pole figure measurement and the corresponding indexation for two azimuthal directions (red and blue). For the sake of clarity the third direction is omitted. The most striking feature of the pole figure is the repetitive pattern as indicated by the dashed/solid edging. The pattern inside this edging is a results of caffeine having either a (5-10) (squares) or a (020) (triangle) contact plane aligning the $\{-602\}$ and $\{-1-12\}$ net planes into this

region. The poles in the dashed area are similarly a result of caffeine crystals, but now having (510) or a (0-20) contact plane. By rotating these two areas by 120° or 240° all other Bragg reflections in the pole figure can be explained.

4.2 Crystal alignment of caffeine deposited onto single crystal surfaces via hot-wall epitaxy⁶³

CrystEngComm



PAPER

[View Article Online](#)
[View Journal](#)

Crystal alignment of caffeine deposited onto single crystal surfaces via hot-wall epitaxy†‡

Christian Röthel,^{†*ab} Michal Radziown,^{†c} Roland Resel,^{†de} Andreas Grois,^b Clemens Simbrunner^{bd} and Oliver Werzer^{*ae}

^a Institute of Pharmaceutical Sciences, Department of Pharmaceutical Technology, Karl-Franzens Universität Graz, Universitätsplatz 1, 8010 Graz, Austria.

E-mail: christian.roethel@uni-graz.at, oliver.werzer@uni-graz.at

^b Institute of Solid State Physics, Graz University of Technology, Petersgasse 16, 8010 Graz, Austria

^c Institute of Semiconductor and Solid State Physics, Johannes Kepler Universität Linz, Altenbergerstraße 69, 4040 Linz, Austria

^d Institute of Solid State Physics, University of Bremen, Otto-Hahn-Allee 1, 28359 Bremen, Germany

^e BioTechMed – Graz, Austria

4.2.1 Preface

Based on the insights of the first caffeine growth studies on muscovite mica, the investigations were extended to cover different surface structures and the effect of temperature on caffeine growth. Samples were provided by Clemens Simbrunner, Michal Radziown and Andreas Grois from the Johannes Kepler University Linz. Structural X-ray investigations, atomic force and optical microscopy were carried out by the first author at TU Graz and University of Graz. Data interpretation and the manuscript preparation was carried out by the first author with assistance of Oliver Werzer und Roland Resel. The provided text and illustrations are identical to the manuscript as submitted to *CrystEngComm* and are reprinted with permission.

4.2.2 Abstract

Defined crystal growth is highly demanded for technological applications but also fundamental research. Within this work, the crystal growth of the asymmetric molecule caffeine was studied on single crystalline surfaces of mus-

covite mica, sodium chloride and potassium chloride. While elongated 'needle-like' crystals grow on muscovite mica and sodium chloride, smaller individual 'bird-like' structures were observed on potassium chloride. Depending on the surface type and temperature, the disk-shaped caffeine molecules prefer either an edge-on or flat-on orientation with respect to the surface, but in each case, a defined crystallographic relation between the surface and caffeine crystallites was determined by using the X-ray pole figure technique. On muscovite mica and sodium chloride, needle-like crystallites with edge-on oriented molecules aligned mainly with the unit cell *c*-axis (which coincides with the long needle axis) along the $[1-10]_{\text{mica}}$, $[100]_{\text{mica}}$, $[110]_{\text{mica}}$ and $[110]_{\text{NaCl}}$, $[1-10]_{\text{NaCl}}$ directions, respectively. Crystals consisting of flat-on oriented molecules on KCl showed also defined alignments with respect to the substrate, but due to the altered molecule-substrate contact, the *b*-axis aligned along $[110]_{\text{KCl}}$ and $[1-10]_{\text{KCl}}$. Growth at elevated temperatures enabled changes in the crystal growth whereby more defined structures formed on NaCl. On KCl, the bird-like structures remained very similar, while caffeine on the mica surface at elevated temperatures resulted in even additional texture forming with the caffeine molecules now also favoring a flat-on orientation with respect to the surface. The systematic variation of various system parameters demonstrates how sensitive the growth behavior of caffeine on this variety of substrates is.

4.2.3 Introduction

Controlled and specific crystal growth of organic materials is of high technological and fundamental interest as it promises reliable and, more importantly, reproducible properties demanded by research and applications.^{9,64,65} While often bulk solution processes are favored for their ease of use, for many technical applications crystallization directly on solid surfaces simplifies production. But the crystallization behavior in the vicinity of surfaces might be strongly influenced or altered compared to those in the bulk.^{40,66} As a simple example, the glass wall in a vessel already provides sufficient disturbance facilitating nucleation, and crystals grow more rapidly.^{2,67} In general, surface properties have a templating effect and often result in distinct crystalline forms.^{68,69} Isotropic surfaces like silica typically induce crystallization from defined contact planes, thus a uni-axial or fiber texture¹⁰ results, on which the azimuthal direction remains undefined.⁷⁰ This results, for example, in caffeine needles growing along

random directions on silica surfaces⁵¹ or pentacene forming randomly uncorrelated islands.⁶⁴ Furthermore, surfaces are sometimes able to selectively dictate specific polymorph formation and additionally the alteration of the surface chemistry enables further tuning of the crystal growth, as observed for aspirin at polymeric surfaces.^{34,71} Besides the surface chemistry, the order and local morphology at the surface impacts crystal growth and nucleation.⁷² For instance, flat surfaces favor the formation of the bulk phase while rough substrates often lead to appearance of metastable thin film phases.⁷³ The degree of order at the surface is larger if anisotropy is present, which also enables directional growth. A simple approach might be rubbed or drawn polymer films or more advanced techniques such as nanoimprinting in which surface corrugations facilitate the alignment of molecular crystals or liquid-crystalline polymers.^{38,74,75} Employing single crystal surfaces increases the degree of order even further and organic crystalline films might grow fully epitaxial.^{76,77} A few examples are sexiphenyl or caffeine grown on sheet silica^{20,40,78} or sexithiophene and perylene-derivatives on alkali halide surfaces.^{17,79,80} Epitaxial or directed crystal growth of organic crystals is used extensively in organic electronic devices or wave guiding applications,⁸ which both depend on a defined molecular orientation. In any case, grain boundaries and other crystal defects in such crystalline layers or needles are known to have a tremendous impact on the physical properties and performance.^{81,82} Moreover, epitaxial crystal growth has been used successfully in the selection of suitable crystal seeds and single crystalline surfaces to obtain elusive cocrystals or to control the polymorphism of active pharmaceutical ingredients.^{83–85} Epitaxial growth was also demonstrated to assist in the formation of theoretically predicted polymorphs such as carbamazepine form V.^{86,87}

Within this work, we demonstrate the crystal formation of the model drug molecule caffeine on muscovite mica, sodium chloride (NaCl) and potassium chloride (KCl) surfaces. While the requirements on caffeine for pharmaceutical applications are mostly limited to purification and polymorph selection, this study offers interesting insights into the nature of organic crystal growth which are not accessible with frequently studied rod-like molecules.¹⁷ Firstly, in contrast to many rod-like molecules, caffeine is easily soluble in various organic solvents, which allows for a comparison between films grown by solution cast techniques and physical vapor depositions such as hot wall epitaxy. Secondly, caffeine molecules are disk-like but due to their chemical groups have

a highly anisotropic character. This is stereotypical of many pharmaceutically relevant molecules, as especially their amphiphilic-like anisotropy allows for penetrating cellular membranes.⁴⁴ Furthermore, caffeine exists in two polymorphic forms, whereby the stable β -form (CSD code: NIWFEE05) has an intriguingly large monoclinic unit cell which hosts 20 molecules. Moreover, molecules assemble in a slightly disturbed hexagonal motif, meaning the disk-like molecules have some degree of freedom in their orientation with respect to the neighboring molecules.^{57,58,88}

Previous studies have shown that caffeine crystallites grow most often in the polymorphic β -form in the shape of extended needles but sometimes hexagonal structures on the account of the metastable α -form (NIWFEE04) are observed.⁴⁹ It was recently shown that needles align on a mica surface when prepared by solution cast techniques.⁵¹ However, crystal growth during solution casting often takes place under non-equilibrium conditions with large variations in the growth kinetics. Thus, the crystalline alignment is rather undefined, which makes it difficult to draw conclusions. Conversely, using a hot wall epitaxy (HWE) process which operates closer to thermodynamic equilibrium^{53,54} was demonstrated to produce more defined and uniform crystal growth.²⁰ In a typical HWE setup, an independent adjustment of the source, wall and substrate temperature can be set ensuring optimal growth conditions for organic crystals. Moreover, as small molecules tend to evaporate rapidly under vacuum conditions, even at room temperature, depositions under ambient pressure conditions can be easily carried out by exchanging the ambient environment to an inert gas atmosphere.

In this work, we extend our previous investigations to various surfaces and temperatures, including NaCl and KCl providing different constraints for nucleation and crystal growth. Changes in the molecular adsorption geometry, crystal alignment and uniformity are evaluated using microscopy techniques. Differences in the directed crystal growth and epitaxial relations are identified by X-ray diffraction pole figure measurements and are correlated to specific surface properties and temperature effects.

4.2.4 Experimental section

Materials. Muscovite mica (grade V-4), NaCl as well as KCl substrates were purchased at SPI Supplies (West Chester, USA). Clean muscovite mica (001) surfaces were obtained by cleaving 15 × 15 mm mica sheets using adhesive tape. NaCl(001) and KCl(001) surfaces were obtained by cleaving the single crystals using a razor blade. After cleaving, the substrates were immediately transferred into the HWE chamber. A detailed description of the crystallographic properties of the substrate surfaces is provided elsewhere.¹⁷ Anhydrous caffeine of pharmaceutical grade was purchased from Herba Chemosan-AG (Vienna, Austria) and used without any modification.

Sample preparation. A custom-made hot wall epitaxy chamber with independent ovens for the evaporation source (quartz tube), evaporation tube wall and substrate, was used to prepare various samples.⁵³ The ambient atmosphere was exchanged with nitrogen immediately after sample transfer. Prior to deposition, substrates were equilibrated for 30 minutes at either 65 °C, 80 °C and 100 °C, ensuring stable thermal conditions. Subsequently, the evaporation source was heated and a shutter was opened so that the substrate surfaces were exposed to a molecular caffeine flux. The molecular depositions were performed under atmospheric pressure using a nitrogen atmosphere ensuring controlled and steady evaporation of the caffeine powder. The reliable operation temperatures for this study were 125 °C and 130 °C for the source and wall, respectively. An equal deposition time of 15 minutes was chosen for each type of substrate

Morphological investigation. Optical microscope images were obtained using an Axiovert 40 microscope (Zeiss, Germany) equipped with polarizers and a digital camera. The film topographies were investigated with a FlexAFM atomic force microscope equipped with an Easyscan 2 controller (both from Nanosurf, Switzerland). Height images were recorded in non-contact mode using a Tap190 cantilever (Budgetsensors, Bulgaria) with a nominal resonant frequency of 190 kHz. All data were processed using the Gwyddion software package.⁵⁶

Crystallographic investigation. The crystallographic relations of caffeine needles and the substrates were investigated by X-ray diffraction pole figure measurements performed using a Philips X'pert diffractometer equipped with a chromium sealed tube, a secondary side graphite monochromator ($\lambda = 0.229$ nm)

and optical slit systems. Briefly, an X-ray diffraction pole figure contains information about the spatial distribution of one specific net plane distance with respect to the substrate surface. During the measurement, the sample is continuously rotated around its surface normal (azimuthal angle φ) and tilted with respect to the incoming beam (inclination angle ψ of the surface normal) after a full 360° turn in φ . The diffraction intensity of each tuple (φ, ψ) is recorded and presented in polar contour plots using a stereographic projection, ψ being the polar radius and φ the polar angle. Spots of enhanced intensities (poles) correspond to Bragg reflections which are caused by net planes fulfilling the Laue condition, meaning the corresponding net planes are normal to the pole direction defined by φ and ψ . Simulating the recorded pole pattern using the software STEREOPOLE¹⁸ allows for the epitaxial relation to be deduced.

4.2.5 Results

Morphology. Caffeine molecules adsorb at a temperature of 65°C onto all investigated single crystal surfaces (muscovite mica, NaCl, KCl) and form crystalline films with defined morphologies (see Figure 4.10). On mica, needle structures develop, which run several $100\ \mu\text{m}$ along the surface. The length only seems to be limited by other needles interfering so that the extension is limited due to geometrical constraints. A closer inspection of such a film using AFM height imaging reveals that these large needles are often a result of smaller needles packing closely together forming a fiber-like needle bundle. The typical width of such individual needles is approximately $200\ \text{nm}$ and the height is $100\ \text{nm}$. The bundle-like structures have typical widths between 5 and $10\ \mu\text{m}$. Besides these, there are single needles which are thicker and higher compared to the others, suggesting that those are slightly different from those forming the broad bundles. However, for any of these structures there is a preferred alignment along the mica surface evident, i.e. they grow along three directions which are nearly parallel, 60° or 120° inclined to the lower image border. This is also reflected in the Fourier transform of the AFM image which reveals three streaks running along the same directions as observed in the height image (see the Supplementary Information).

Deposition of caffeine onto freshly cleaved NaCl surfaces results again in needle-like structure formation (see Figure 4.10, middle). There is also a certain degree

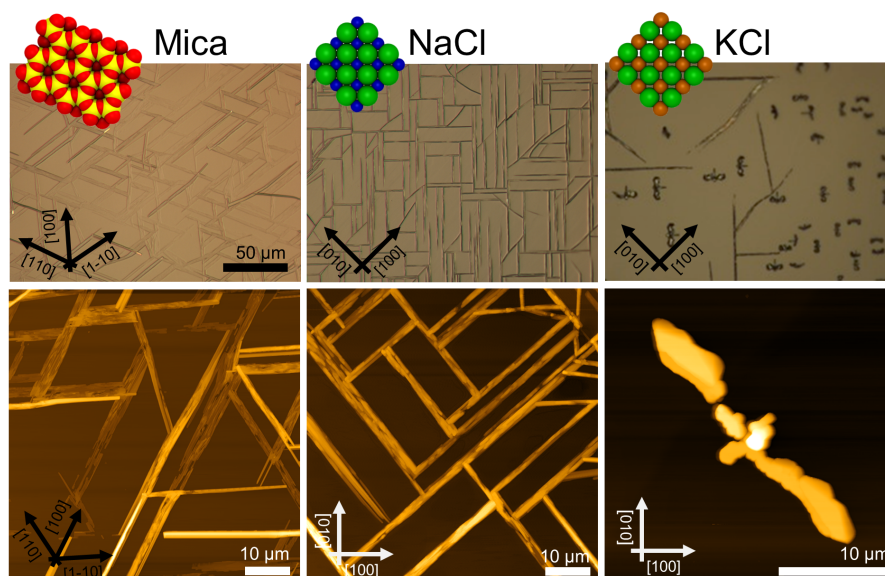


Figure 4.10: Top: Optical micrographs showing caffeine needles on various single crystalline surfaces. The inset illustrates the single crystalline surfaces made up of oxygen (red), silicon (yellow), chlorine (green), sodium (blue) and potassium (orange). Black arrows indicate the real space surface directions. Bottom: Atomic force microscopy height images showing the morphology of individual caffeine crystallites. Please bear in mind that AFM images are rotated with respect to the optical microscopy due to measurement constraints.

of bundle formation, but to a much lower extent. Compared to the mica sample, these structures have a smaller maximal width of 5 μm. The length again seems to be limited by adjacent needles interfering. The majority of needles show an alignment along distinct directions; needles aligning parallel or perpendicular to the lower image border exist, which is also reflected by FFT of the AFM images (see the Supplementary Information Figure 4.16). In addition, there are some needles inclining by about 45°. These needles seem to show a certain curvature, i.e. they deviate from a straight line. Such a curvature is absent in the other needles running 0° or 90° with respect to the image border. Furthermore, the inclined structures form only if the other needles are present, i.e. an independent alignment along this direction was not observed even if the caffeine deposition was significantly shorter (data not shown).

Exchanging the sodium in the surface by potassium, i.e. using a KCl substrate, the caffeine crystal morphology changes drastically. Occasionally, needle-like structures can be observed, which run along the same directions as on the NaCl

surface, but the frequency of these structures is low. The more dominant morphologies are structures in a T-shape, even having similarities with the appearance of birds or bats with open wings, one might conclude. The wing span of the bird depicted in the AFM image (Figure 4.10 right) is 26 μm and it has a head to tail distance of about 5 μm . The highest point is close to the wing ends and reaches nearly 3 μm . The individual birds align so that the tail points towards the same directions as the needles; this results in overall four different directions being noted, with birds looking up, down, left or right, respectively.

X-ray diffraction pole figures. The morphological investigations already suggest that directional defined caffeine crystal growth takes place at various surfaces. To extract the crystallographic information and to establish the epitaxial relations within the various samples, X-ray diffraction in the context of pole figure measurements is one of the best suited methods. Measurements for the various samples for a specific set of net planes are summarized in Figure 4.11.

Starting with the mica sample, seven poles can be identified, all of which can be attributed to net planes with an interplanar d -spacing of approximately 0.75 nm ($|\mathbf{q}| = 8.4 \text{ nm}^{-1}$). One pole is in the center which corresponds to net planes that lie parallel to the mica surface and is typically referred to as the contact plane. The remaining six poles are at inclination or tilt angles of $\psi = 60^\circ$ but vary in their azimuthal positions ($\varphi = 30^\circ, 90^\circ, 150^\circ, 210^\circ, 270^\circ, 330^\circ$). Setting the center of the pole figure to be the 510 reflection results in the poles at $\psi = 30^\circ$ and $\psi = 60^\circ$ being the 020 reflection and the pole at $\psi = 210^\circ$ and $\psi = 60^\circ$ corresponds to the 5-10 reflection. This means that one caffeine needle species is able to explain three poles. To explain the other poles at $\psi = 90^\circ, 150^\circ, 270^\circ$ and 330° , two additional caffeine crystal alignments are required. These needles are identical in their crystallographic properties but their azimuthal alignment is rotated by 60° to another. Having knowledge of the crystallographic unit cell, the net plane orientations allow for the determination of the alignment of the crystal axes with respect to the surface. The orientation of the crystallographic axis of the substrate surface is established by measuring and indexing pole figures of easily accessible net planes of the substrate (data not shown) without changing the sample alignment in the diffractometer to obtain comparable measurements. For the first needle species at $\psi = 30^\circ$, the crystallographic c -axis points toward the [1-10] real space direction of mica.²⁰ This direction coincides also with the long needle axis of one mica needle species.

Hence, the c -axes (or long needle axis) of the remaining two needle species point towards the $[110]_{\text{mica}}$ or $[100]_{\text{mica}}$ direction.

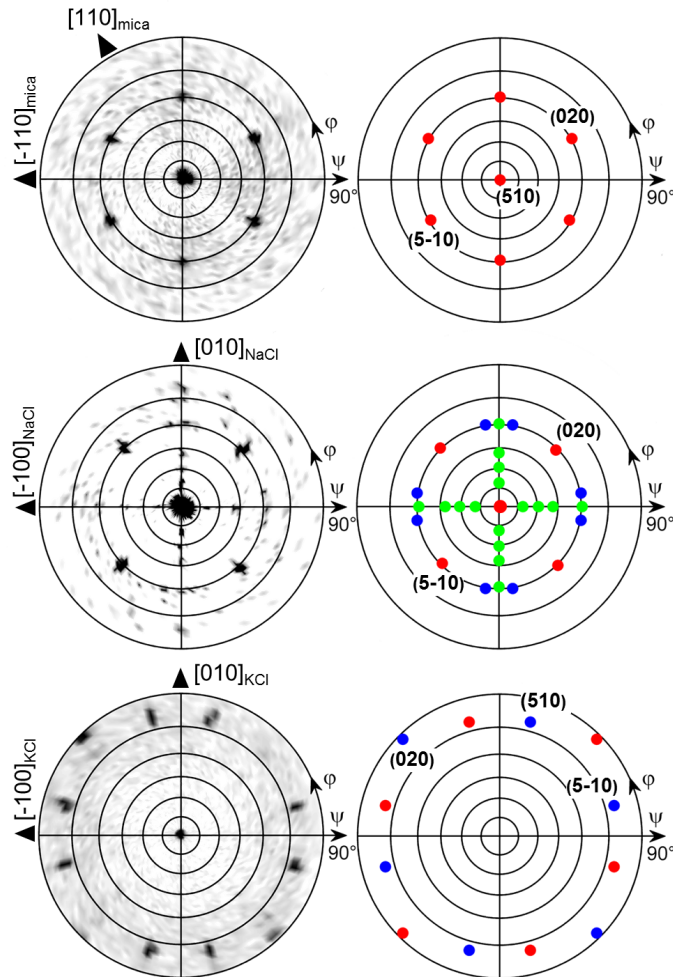


Figure 4.11: Pole figures used for the determination of the crystal alignment on muscovite mica, sodium chloride and potassium chloride single crystal surfaces. The left column shows experimental data and the right column shows the simulation. Black triangles indicate real space directions on the corresponding crystal surface.

This very same measurement was also performed on the NaCl sample (Figure 4.11, middle). Again, the center pole can be attributed to net planes parallel to the surface, i.e. the (510) . There are also poles found at inclination angles of $\psi = 60^\circ$ as on muscovite mica but the number of poles is reduced from six to four dominant peaks (red markers). These poles are found at $\psi = 45^\circ, 135^\circ, 225^\circ$ and 315° . Since the measurement is taken at an identical scattering vector to

that on the mica sample, a similar indexation scheme applies whereby only two needle directions require consideration to explain the dominant peaks. One crystal species is aligned with the c -axis pointing towards $[110]_{\text{NaCl}}$ and the other points towards the $[1-10]_{\text{NaCl}}$ direction. Besides the strong poles, some additional weak poles (green markers) are found along $\psi = 0^\circ, 90^\circ, 180^\circ$ and 270° forming a cross-like shape which are accompanied by even weaker peaks (blue) to the left and right. The indexation reveals that these c -axes of these structures now point toward the $[100]_{\text{NaCl}}$ and the $[010]_{\text{NaCl}}$ directions, which is 45° rotated with respect to the previous. This direction is the same as in the intermediate needle structures observable off the two main directions.

As already expected from the microscopy investigations, the KCl sample shows a remarkably different behavior in the XRD measurements. The most striking difference in the pole figure (see Figure 4.11, bottom) is the lack of a pole in the center (excluding the faint peak in the center due to tails of higher harmonic substrate peaks) and the region of $\psi = 60^\circ$. In the case of KCl, twelve poles are located at inclination angles beyond 75° . They can be grouped into two sets of six poles (shown in red and blue), an indication of two crystalline alignments being present. Furthermore, such high inclination angles suggest that a change of contact plane took place. Since the net planes under investigation in this pole figure are still unchanged from the previous measurements, indexing the poles using 020 and 510 reflections identifies the alignment of the caffeine unit cell with the b -axis being along the $[1-10]$ and $[110]_{\text{KCl}}$ surface directions.

Substrate temperature variations. The deposition of caffeine onto mica held at 80°C allows for adsorbing molecules and needle-like structures that form on the substrate surface (see Figure 4.12a). Other than at lower temperatures, the order of the broader structures decreases significantly, resulting in needles showing some degree of curvature. A more detailed inspection shows that those broad structures consist of smaller needles of straight appearance packing slightly rotated to adjacent needles. Using a substrate temperature of 100°C , caffeine molecules are unable to adsorb at the mica surface and hence a blank substrate surface resulted even after deposition as long as 20 minutes (data not shown). The pole figure measurement of the 80°C sample contains poles identical to those of the 65°C (see Figure 4.13 left) i.e. six poles at inclinations of $\psi = 60^\circ$ are present. However, there are various other peaks which were absent at lower substrate temperatures. The indexation shows that these poles are ex-

plained by caffeine crystals of a different orientation (contact plane) which is very similar to the situation on KCl at 65 °C.

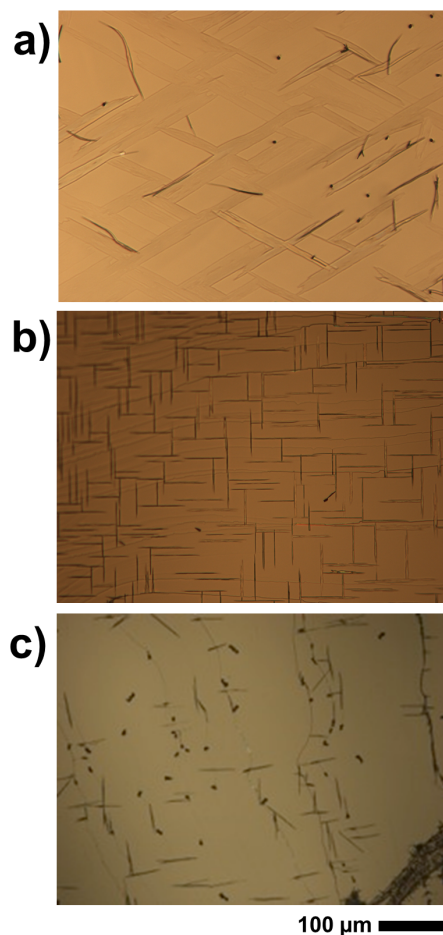


Figure 4.12: Optical micrographs showing the morphology of caffeine deposited at elevated substrate temperatures of 80 °C for muscovite mica (a) and 100 °C for NaCl (b) and KCl (c). The scale is identical for all images. Please bear in mind that the large object in the right bottom corner of (c) is caused by a cleavage step of the KCl crystal and not related to the caffeine deposition.

Moving on to the NaCl surface and using elevated temperatures shows again needle formation even for substrate temperatures as high as 100 °C, as shown in Figure 4.12b. However, the sample differs from the NaCl samples prepared at 65 °C in two aspects. Firstly, the number of needles decreases but with slightly increased widths while leaving the height of the needles very similar at around 240 nm. The second difference is the absence of the intermediate structures which incline 45° to the others. Measurement at 80 °C shows an intermediate situation (see the Supplementary Information Figure 4.17), meaning the

cancellation of the intermediate structures must take place in between 80 °C and 100 °C. The pole figure measurement, for a sample prepared at 100 °C, does show only information from the needles running along the [110] and [1-10] direction while the cross-like diffraction pattern vanished, as is somehow expected from the morphological differences (see Figure 4.13, right).

A KCl surface allows for caffeine adsorption and crystal growth even at 100 °C too. Similar to the NaCl sample, the amount of caffeine on the surface decreases but the overall appearance of the structures remains nearly identical to the 65 °C sample (Figure 4.12c). The pole figure investigation of a KCl sample prepared at 100 °C does not show any difference compared to those prepared at lower temperature (data not shown). Only the overall pole intensities are lower, which results from the lower amount of material present. Reliable conclusions regarding the relative amount of "bird"- and needle-like crystallites are difficult to draw since the intensity of the poles is strongly influenced by the sample roughness and macroscopic cleavage steps.

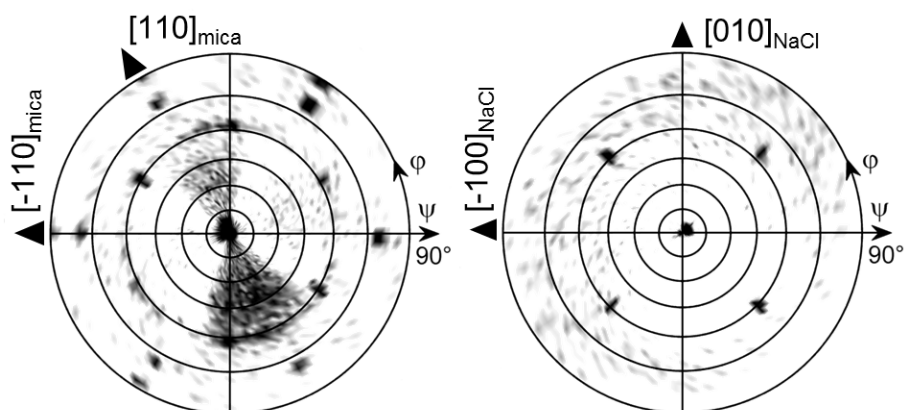


Figure 4.13: Pole figures of caffeine on mica (left) and NaCl (right) deposited at elevated substrate temperatures of 80 °C and 100 °C, respectively.

4.2.6 Discussion

Molecular orientation. Caffeine molecules are of disc-like shape and are highly asymmetric and feature a rather complex packing motif in the solid state. In the literature, there are two anhydrous polymorphs of caffeine described, the α and the β polymorphs, whereby in this study only the stable β -form was identified. In the β -form the molecules show parallel stacking along the crystallo-

graphic c -axis (see Figure 4.13a). In the unit cell a - b plane, the molecules pack in a nearly hexagonal fashion, whereby a slight compression exists, as depicted in Figure 4.13b. This compression means that molecules within the slices of the caffeine crystals incline slightly with respect to an adjacent slice resulting in an ABAB stacking order within the a - b plane. A particular interesting aspect of caffeine is its rotational molecular packing. Unlike in ideal or perfect crystal packings, some disorder disturbs the crystalline packing. While the centroid positions of the molecules are well-defined, the molecules exhibit rotational freedom around the disk plane normal (see Figure 4.13).⁵⁸ While the overall hexagonal-like packing motif remains unaffected, such disorder or plasticity means that molecules are more likely able to adapt to different adsorption sites rather than being constrained by the crystal lattice. This together with the large number of molecules within the unit cell means that likely molecular contacts with the substrate cannot be identified. From the experimental investigations however, the results of the collective caffeine interactions with the interface or substrate can be deduced, which for many applications are of high interest.

The particular characteristics of the caffeine crystal packing leads to the presence of various net planes of rather similar properties within the crystalline caffeine needle. Specifically, this means that crystal contacts with either the (020), (510) or the (5-10) plane are equivalently capable of describing the specific needle growth behavior at surfaces. Usually the crystal shape (morphology) results from low-energy planes (facets) which typically for crystals means that these differ for different contact planes. However, due to their similarity the morphology of individual caffeine needles is not affected by this very consideration of the actual contact plane. In fact, the occurrence of these three particular contact planes is just a result of needles being rotated by $\psi = 60^\circ$ along the long needle axis in accordance with the nearly hexagonal packing. This assumption is also reflected by the pole figure results which show a relative inclination of approximately 60° between the (020) and the (510) or (5-10) plane. Thus, poles with inclination angles of $\psi = 60^\circ$ will be observed regardless of which of the aforementioned contact planes is selected. Moreover, having one of these three contact planes as present on NaCl or some mica samples means that caffeine molecules adapt an edge-on molecular orientation with respect to the surface. This minimizes the interaction area with the underlying substrate.

For caffeine deposited either on KCl or on mica at 80°C , poles in the XRD

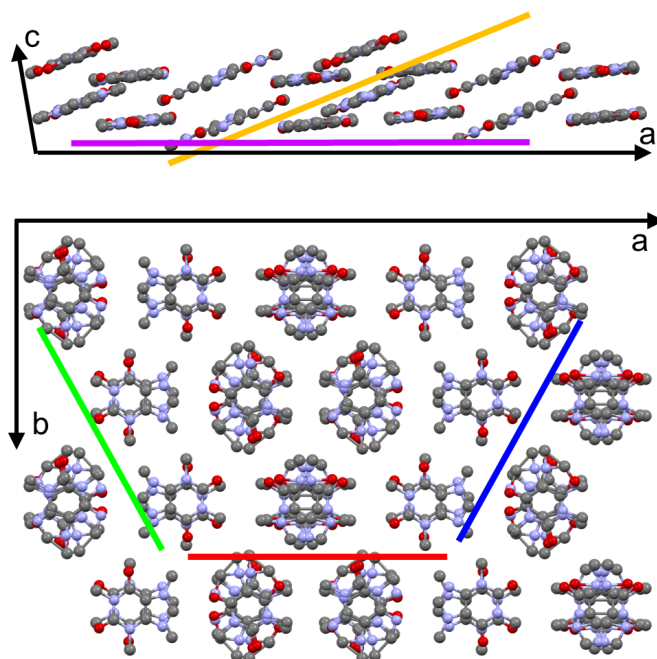


Figure 4.14: View along the crystallographic *b*-axis (top) and *c*-axis (bottom) of caffeine molecules assembling in the β -form. Projection of the (-703) and (001) net planes are shown in orange and magenta. (020), (510) and (5-10) net planes are shown in red, blue and green, respectively, and are arranged to highlight the hexagonal-like packing. Disorder is represented by overlapping molecules; hydrogen atoms are not shown.

investigation appeared at inclination angles ψ beyond 75° . This is significantly higher compared to poles caused by edge-on oriented molecules which were at $\psi = 60^\circ$. This inclination change has to be from crystal orientations in contact with net planes different from (020), (510) or (5-10), respectively; simulations of the data show that either a (001) or a (-703) contact plane results in these particular pole patterns. While the latter seems rather arbitrary, it becomes clearer on closer inspection of the unit cell and the molecular orientation therein (see Figure 4.13). The (001) or (-703) contact planes provide cuts through the crystal with molecules lying parallel to these planes. Since the molecules within the unit cell can be separated into two groups (A or B stack) with different orientations, it seems reasonable that both contact planes provide similar adsorption properties due to their similarity regarding the actual molecule–substrate interaction.

Comparing the pole inclinations resulting from these contact planes shows a theoretical difference of 5° in the inclination ψ , which should be sufficient to

resolve two separate poles in the measurement. However, only one radially (ψ -direction) smeared out peak is observed. Hence, it is very likely that crystals adapt both the aforementioned contact planes, and even intermediate situations might occur, which explains one less defined pole. Despite some uncertainty in the contact plane determination, the overall absorption geometry changed clearly from an edge-on to a flat-on orientation with the change of substrate from NaCl to KCl or with increasing substrate temperature as in the case of muscovite mica.

Now the question arises as to why the caffeine crystals favor one orientation over the other. In general, there are several aspects to take into account. Molecules will adapt a flat-on orientation for the situation of molecule–molecule interaction being less dominant compared to the molecule–substrate interaction. In turn, strong molecule–molecule interaction in sufficiently large molecular clusters allows for a reorientation into an edge-on conformation as the amount of molecules at a surface increases.^{17,62} This mechanism is similar to the nucleation in solution as described by the two-step nucleation theory, where the actual nucleation is preceded by the formation of disordered clusters.^{1,89} Other reports demonstrated that the structure at the very interface region, which in our case is inaccessible, has a strong impact on the crystal formation/growth. For instance, the anisotropic surface properties favor molecular transport along certain directions,⁹⁰ which then assists in nuclei formation consisting of lying molecules. On poor surface definition (or incompatibility), this nuclei formation required a molecule rising, so that molecule–molecule assembling into low energetic states is possible. Furthermore, one needs to keep in mind that caffeine has a plastic phase character too, meaning the molecules might choose their rotational order at some lattice sites. This, for instance, might allow that molecules rearrange to adapt for energetically more favorable adsorption geometries most likely required to adapt for the surface constraints.

Azimuthal alignment. Besides the different molecular orientations with respect to the surface, caffeine also shows distinct azimuthal order on all substrates. For the edge-on caffeine crystals on mica, it follows that the c -axis, which coincides with the long needle axis, points towards the [1-10], [110] or [100] real space direction of mica when the substrate temperature was 65 °C during deposition. This particular alignment is clearly connected to the surface geometry of muscovite mica. Mica is a rather complex material and belongs to

the sheet silicate family featuring a layered structure of two alternating layers.⁶¹ Cleaving separates two (001) planes, leaving this plane as an outer surface for molecule deposition. Such a surface features a regular lattice which is defined by oxygen atoms running along three distinct directions inclining 120° to one another. This would suggest that mica has a 3-fold symmetry. However, intermediate places in the surface are occupied by aluminum atoms. These are ordered differently compared to the oxygen atoms, which causes a slight surface lattice distortion with oxygen atoms being slightly lower along the [1-10] direction. Thus, a corrugation exists in the surface with an approximate depth of 0.08 nm, as determined by AFM investigations.⁹¹ As a consequence, the mica surface features only mirror symmetry along the [1-10] direction.⁴⁰ Depending on the deposit, mica enables order due to its mirror symmetry or via its pseudo 3-fold symmetry.^{20,40} In fact, the caffeine needles in this study align along three directions in accordance with a pseudo 3-fold symmetry. Also the long needle axis coincides with the hexagonal-like packing of the oxygen atoms in the mica surface. As pointed out earlier, the molecules in such a caffeine needle show various orientations with respect to the surface. This suggests that the alignment during the nucleation or growth process likely results from collective adaptation of many molecules simultaneously. This is distinct from systems of strong single molecule–substrate interactions for which the crystal alignment is dominated on a smaller scale, i.e. the molecule rather than the collective nuclei/crystal.⁴⁰

It should be noted, that deposition of caffeine on mica, even just for very short times of 5 minutes (data not shown) always shows three directions being present, i.e. needles growing along a certain direction are always accompanied by other needles which are inclined by 60° . Interestingly, 60° inclination can be observed on NaCl surfaces as well even if it is only obvious when close to other needles. For samples prepared on isotropic silica surfaces, this 60° branching also exists (see the Supplementary Information Figure 4.18) which means that this type of structure is likely an inherent property of caffeine crystals growing at surfaces and is often referred to as ledge directed growth.⁹² Ledge directed growth means that a facet on a crystal is able to host nuclei of different crystal directions, which eventually grows into needles, in the case of caffeine, 60° off the initial direction. While this effect is much less frequent on NaCl, the pseudo 3-fold symmetry which exactly matches the 60° inclination might assist in the ledge directed growth, which in turn means that the other directions are more

likely to form. If the other directions are a consequence of solely ledge directed growth, the initial alignment of the caffeine 'network' might likely occur due to the surface corrugation along the mirror plane direction of mica, i.e. the [1-10] direction, and the others are just coincidentally aligned along the other main mica directions.

On NaCl, caffeine needles align with the *c*-axis along the [110] and [1-10] direction, while the molecules adopted an edge-on orientation which coincides with the surface corrugations on the NaCl surface (c.f. Figure 4.10 and 4.15). The grooves in the surface result from the different ion radii of sodium (0.116 nm) and chlorine (0.167 nm), giving an approximate corrugation depth of 0.05 nm which is slightly smaller than the grooves on muscovite mica (0.08 nm). Besides the obviously altered substrate surface chemistry, this geometrical constraint (corrugation) may also play an important role in the overall needle alignment. A similar behavior was found previously in other systems, where surface corrugations in alkali halide surfaces induced directed growth of sexiphenyl or perylene-derivatives such as PTCDA among others.^{80,93} Nevertheless, *c*-axis alignment along the surface grooves means that the caffeine disks preferably align along rows consisting of either sodium or chlorine rather than with alternating atom species, as schemed in Figure 4.13.

The morphological investigations reveal that for the NaCl sample needles align along [110] and [1-10] direction, and also needles which align partly along the [100] or [010] direction are present. As briefly mentioned before, the growth of such needles is very likely a result from ledge directed growth, i.e. needles start out at a facet of a 'regular' substrate aligned needle and grow with inclinations of 60°, as can be seen in the AFM investigations. On further extension from the facet, the needle direction bends and eventually results in a needle alignment of 45° with respect to the other crystal directions. This behavior might reflect the competing impact of the crystal and the substrate on the needle alignment; the regular needle dictates the initial growth process while the underlying substrate tries bending the needle for more favorable positions and a gradual transition (curvature) results. In addition to the visible morphology, the cross-like feature in the pole figure with various poles along a given ψ angle means (green markers for $\psi < 60^\circ$) that these inclined structures have some degree of freedom in their contact plane, again in agreement with the hexagonal nature of the caffeine packing in the unit cell. This results in many rotations around the long

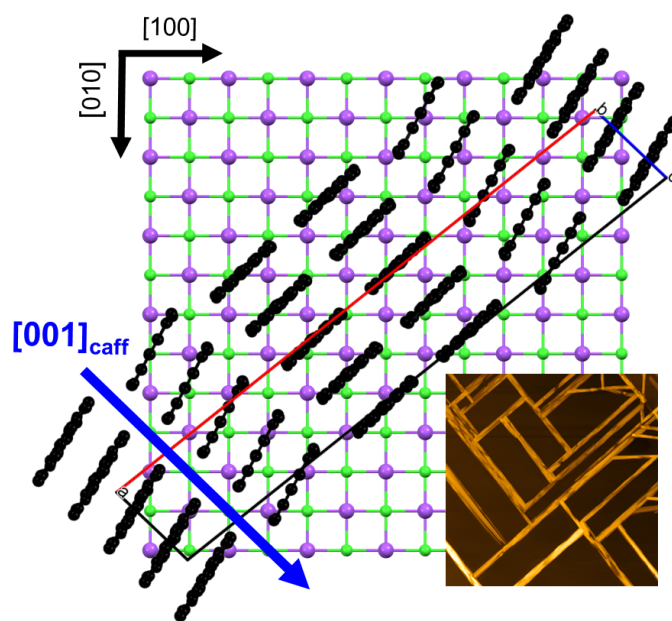


Figure 4.15: Molecular alignment of caffeine with respect to the NaCl(001) surface depicted for caffeine needles growing along the $[110]_{\text{NaCl}}$ direction. The blue arrow indicates the long needle axis of caffeine.

needle axis (c -axis) forming simultaneously on the sample surface.

Further analysis of this complex pole figure regarding the accompanying needles (blue poles) revealed that an a -axis alignment along the $[100]$ or $[010]$ also exists. Such an a -axis alignment can be easily seen because of the monoclinic caffeine unit cell in which the growth directions deviate by $\pm 9^\circ$ with respect to the c -axis aligned needles (a detailed explanation is provided in the Supplementary Information). This means that on NaCl there is also a favorable energetic state (local energetic minimum) which then results in a slight deviation of the interaction with the substrate. Nevertheless, 9° inclination might be just a result of adjacent caffeine sheets being inclined by a certain degree, meaning that a caffeine A-layer is about 9° rotated to a B-layer. A substrate temperature of 100°C during deposition suppresses the growth of any ledge directed needles. Elevated substrate temperatures mean that more energy is present in the system, which allows for escaping the local minima required for ledge directed growth more easily. Thus, molecule arrangements in energetically more favorable positions are solely occurring.

Despite being in the same crystal class (rock salt) and thus providing a sim-

ilar cubic surface geometry the resultant crystal growth on KCl and NaCl is remarkably different. Due to the substitution of sodium with potassium, the cubic lattice constant increases from $a_{\text{NaCl}} = 5.64 \text{ \AA}$ to $a_{\text{KCl}} = 6.29 \text{ \AA}$. Since the ion radius of potassium (0.152 nm) is considerably larger than of sodium (0.116 nm), the surface corrugations along the KCl surface decreased significantly compared to the NaCl surface grooves. Moreover, due to the increased KCl lattice spacing the lateral distance between adjacent surface grooves increases. This is of particular interest if compared to the *c*-axis of the caffeine crystal, which is 6.95 \AA (see Figure 4.13). Similar to lattice matching, as used for inorganic epitaxy, the compatibility of caffeine with the substrate can be estimated; the lateral groove spacing on KCl is $d_{g,\text{KCl}} = 4.45 \text{ \AA}$ and on NaCl this spacing decreases to $d_{g,\text{NaCl}} = 3.97 \text{ \AA}$. Using a simple calculation, it was shown that $7 \cdot d_{g,\text{NaCl}} = 4 \cdot c_{\text{caffeine}} \pm 0.05 \text{ \AA}$, whereby a similar calculation for caffeine on KCl did not provide any similar agreement (the closest match is obtained for $11 \cdot d_{g,\text{KCl}} = 7 \cdot c_{\text{caffeine}} \pm 0.23 \text{ \AA}$ which has a much larger error). From this simple consideration, it can be followed that the NaCl lattice along the considered direction is more compatible with edge-on molecular caffeine packing if compared to the KCl lattice for which the flat-on molecules are favorable.

The consequence of the flat-on molecule orientation on KCl reveals morphologies which deviate strongly from elongated needle shapes. Crystals of a bird-like character, containing wings and a tail, are observed. More detailed inspection might even allow suggesting that the wings of the birds are composed of facets inclined by 120° , corresponding to hexagon formation together with some linear (needle-like) segments forming the bird tails. Pole figure measurements show clearly a defined crystal alignment with respect to the KCl substrate surface where the *b*-axis is in-plane with the surface, aligning either along the $[110]_{\text{KCl}}$ or the $[1-10]_{\text{KCl}}$ direction. The molecular packing in the unit cell *a*-*b* plane is hexagonal, which is similarly oriented to the 120° segments of the bird wings. Remarkably, the individual birds have a similar size on the entire substrate surface meaning a well-defined growth mechanism is responsible for this bird formation. For instance, a single bird wing is not symmetric, and the upper side seems different from the lower side. Likely, this is a result of the crystal *c*-axis being not perfectly perpendicular to the surface, thus also the *b*-axis is slightly inclined with respect to the sample surface. On molecule condensation at the crystal sites, this inclination favors crystal growth along one direction

while simultaneously disfavoring the growth in the other direction simply due to geometrical constraints.

4.2.7 Conclusion

While defined needle-like crystal growth on solid substrates is often observed for organic molecules, disk-like caffeine with its asymmetric molecular conformation shows a particularly complex growth behavior. While elongated needle-like crystallites consisting of edge-on oriented molecules run along characteristic surface directions on NaCl and muscovite mica, smaller 'bird-like' structures are observed on KCl due to flat-on oriented molecules. However, on every single crystal surface investigated in this study an epitaxial relation between the surface and the caffeine structures could be identified. The differences in the various samples in terms of caffeine growth mean that the molecular orientation as well as the azimuthal alignment depends strongly on the substrate surface geometry and chemistry but also on the substrate temperature during deposition. Interestingly, caffeine crystallites align well at the surface whereby the crystals have significantly more freedom compared to other organic crystals, i.e. many different contact planes allow for a very similar macroscopic needle alignment. Many aspects of its intriguing growth behavior are most likely rooted in its crystalline packing which offers some orientational degrees of freedom for the molecules within the crystal unit cell but also for the adsorption sites. This means that the crystal growth and alignment is likely driven by the collective interaction properties of a caffeine crystal with the surface, rather than a result of single molecule–substrate interactions. The results of this study clearly show that the molecular orientation with respect to the surface might change (different contact planes) but the crystalline alignment can be conserved. To some extent it might be possible to find a similar behavior for a variety of disc-like molecules, for which specific growth is of high interest whereby it is very likely that the chemistry of the molecules, the preparation technique and all substrate properties will have a profound effect on the directional growth.

4.2.8 Acknowledgements

The work was funded by the Austrian Science Fund (FWF): P25541, P25154 and P25887. The authors gratefully acknowledge support from NAWI Graz.

4.2.9 Supplementary Information

Atomic Force Microscopy

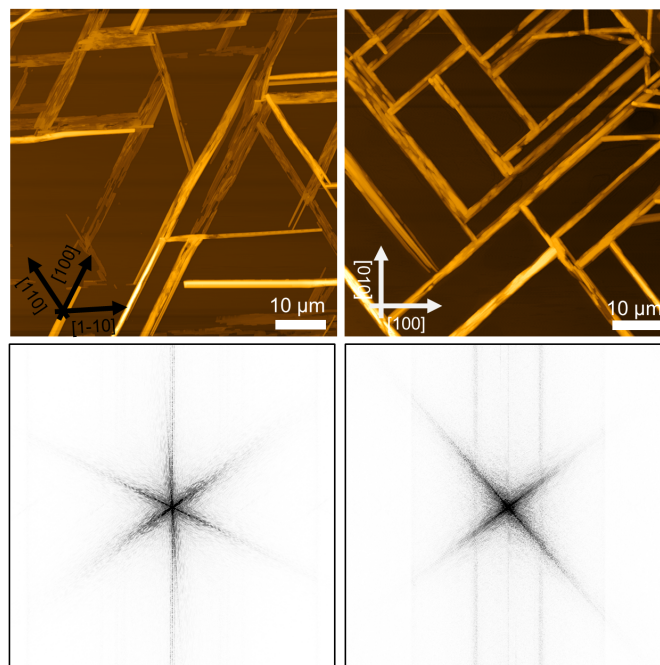


Figure 4.16: Atomic force microscopy height images of caffeine needles on muscovite mica (left) and sodium chloride (right). Bottom row shows the corresponding 2D FFT reflecting the 3-fold and 2-fold symmetry of the needle growth on muscovite mica and NaCl surfaces, respectively.

Caffeine on silica surfaces

Caffeine grown on isotropic silica surfaces results in short needle-like structures, with the size and coverage depending on the substrate temperature (see Figure 4.18). In contrast to caffeine grown on single crystalline surfaces, the needles show no particular azimuthal alignment. While the needles itself are randomly distributed along the surface, contacting needles show a preference for inclination angles of approximately 60° or 120° , respectively.

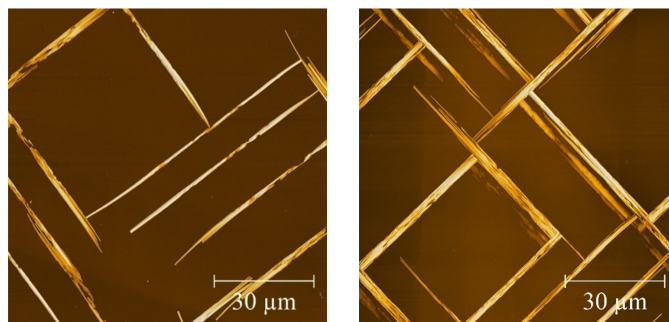


Figure 4.17: Comparison of AFM height images showing caffeine needles deposited on NaCl at 100 °C (left) and 80 °C (right). Intermediate directions along [100] and [010] i.e. rotated by 45° with respect to the depicted needles, are not observed due to the elevated substrate temperatures.

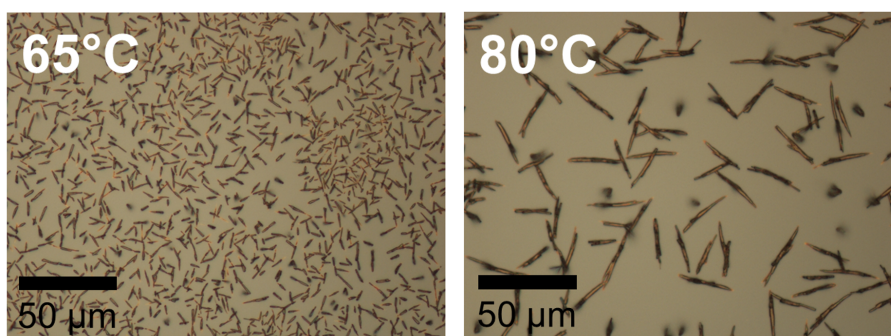


Figure 4.18: Caffeine grown on isotropic silica at 65 °C and 80 °C substrate temperature.

[100] and [010] needle alignment on NaCl

While samples prepared at 100 °C on NaCl show a well-defined crystal growth along the [110] and [-110] direction, the growth at lower temperatures of 65 °C shows a more complex and diverse crystal growth. The corresponding X-ray pole figure and the result is shown in Figure 4.19. Most pronounced are the specular reflection at $\psi = 0^\circ$ and four peaks at $\psi = 60^\circ$ with $\varphi = 45^\circ, 135^\circ, 225^\circ$ and 315° . These are the very same positions as obtained at 100 °C substrate temperature (see Figure 4.13 in the main text), i.e. these correspond to needles grown along the $[110]_{\text{NaCl}}$ and $[1-10]_{\text{NaCl}}$ direction, respectively. In the indexing pattern these are indicated by red dots (see Figure 4.19). Other poles at $\psi = 60^\circ$ are found but with $\varphi = 0^\circ, 90^\circ, 180^\circ$ and 100° (green dots). Their intensities are low, meaning that these are present less frequently. For these azimuthal alignments (φ) also poles at different inclinations ψ are found; low intense poles are located at $\psi = 20^\circ, 31^\circ$ and 42° . While this seems to be a very complex pole figure, the caffeine packing allows understanding this pole figure in detail. Starting with the green pole at $(\psi/\varphi) = (60^\circ/90^\circ)$: It is explained by caffeine having again a (510) contact plane. Other than on the sample prepared at 100 °C, the needle axis is rotated around φ by 45° , which means the long needles axis points towards the $[010]_{\text{NaCl}}$ direction. Poles at $\psi = 20^\circ, 31^\circ$ and 42° are a consequence of caffeine needles with altered contact planes: (520), (530) and (550) contact planes explain these poles. These contact planes share a common axis of rotation (c -axis) known as the zone axis i.e. the needles are rotated along the long needle axis while their azimuthal alignment φ remains unaffected. Nevertheless, there are still some unattended weak residual poles (blue dots) left. Firstly, assuming a (020) contact plane results in the (510) and (-510) being the corresponding poles to index these reflections. The indexing of these poles results in the c -axis inclining by 9° with respect to the $[100]_{\text{NaCl}}$ direction but now with the a -axis matching $[010]_{\text{NaCl}}$ (or equivalent directions). While this might be surprising, the reason for such a splitting on account of the a -axis alignment is due to the monoclinic unit cell angle $\beta = 99^\circ$. Thus, flipping a crystal with a (020) contact plane creates a (0-20) contact plane and the apparent monoclinic angle changes to 81° , meaning the crystal flipping is not invariant.

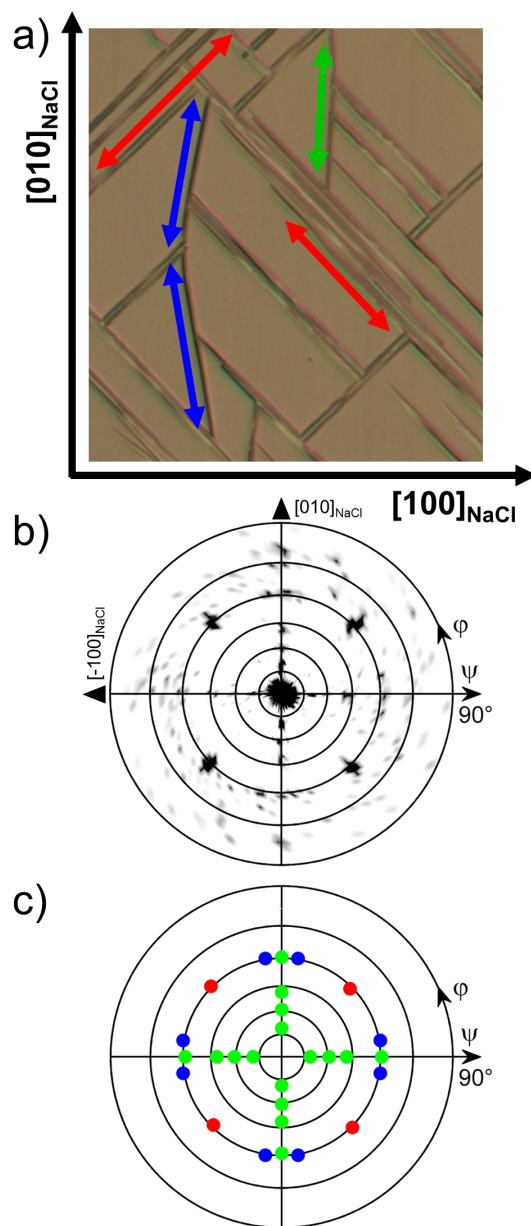


Figure 4.19: a) Optical micrograph of needles grown on NaCl at 65 °C substrate temperature. Black arrows indicate NaCl real space directions and colored arrows indicate the long needle axis (caffeine c -axis) for various needle alignments. Corresponding pole figure measurement taken at $q_z = 8.4 \text{ nm}^{-1}$ (b) with simulation (c). Black triangles in the pole figure indicate NaCl surface directions.

4.3 Continuous crystal lattice tuning by non-stoichiometric intermixing of small organic molecules

Christian Röthel,^{1,2} Paul Christian,² Heike M. A. Ehmman,¹ Hans Riegler¹, Nicola Demitri,³ and Oliver Werzer¹

¹Institute of Pharmaceutical Sciences, Department of Pharmaceutical Technology, University of Graz, Austria

²Institute of Solid State Physics, Graz University of Technology, Austria

³Elettra Sincrotrone Trieste, Area Science Park, Basovizza, Italy

4.3.1 Preface

This work is based on grazing incidence X-ray diffraction (GIXD) thin film measurements performed at the ELETTRA synchrotron applying the measurement strategies as outlined in Section 2.6.3. Sample preparation, optical microscopy, GIXD and specular X-ray measurements and subsequent structural X-ray data evaluation were carried by the first author. Single crystal structure solutions were carried out by the beamline scientist Nicola Demitri. The UV-Vis spectra were recorded by Hans Riegler. Heike Ehmman and Paul Christian assisted during the GIXD measurements. The manuscript was written by the first author with assistance of Oliver Werzer. At the time of writing, this manuscript was submitted to *Crystal Growth & Design* for consideration as a full article.

4.3.2 Abstract

Mixing organic molecules of similar size and shape shows interesting behavior beyond common co-crystallization. In particular crystals containing iminosilbene and phenothiazine, the lattice sites are occupied by different molecular constituents in a random fashion. As a consequence, the crystal lattice constants depend on the mixing ratios of the organic molecules and as such can be tuned between the pristine crystal lattices. In this study, thin films consisting of mixed crystals hosting various amounts of these pharmaceutical drug molecules were grown directly on a solid substrate using drop casting techniques. The resultant

films were investigated by various X-ray diffraction based methods to determine the structural changes (lattice expansion or compression) and molecular packing within the pristine and mixed crystals. The results reveal a lack of a miscibility gap for the phenothiazine/imino stilbene system which allowed for the continuous modulation of the lattice constants within the range of the pure pristine materials. Similarly, the mixing ratio can be facilitated to adjust light absorption properties, which makes it an excellent example of the capabilities of such a non-stoichiometric crystalline system.

4.3.3 Introduction

Physical and chemical properties of solid materials are defined by micro structure at the atomic scale which in turn means controlling or even designing materials on a molecular scale enables many new functionalities.^{24,90,94} This can then satisfy the requirements as demanded by all kind of applications including organic electronics or pharmaceutical science whereby the latter might be even employ more specific targets of individual persons often referred to as personalized medicine.^{95,96} In many cases also the alteration of crystallization and polymorph forming can assist in gaining favorable solid state properties which enables more specific applications and even advanced medicines.^{97,98}

The different solid states of a specific organic molecule show a variety of properties. For instance, an amorphous solid state consists of a random arrangement of its constituents and typically provides enhanced dissolution properties but on account of a lower long time stability. Crystalline materials show a defined long range order of periodically arranged molecules making them more stable compared to amorphous materials. For organic molecules, the driving force for crystal packing is the rather weak intermolecular van der Waals interaction. Thus, different molecular packings often are accessible which is known as polymorphism.^{99,100} Since the molecular packing is decisive for material properties, such as optical, lattice constants, electrical and solubility among others, each polymorphic form has its specific set of distinct properties. Most often, these properties differ drastically between individual polymorphs and a change from one polymorph to another result usually in abrupt and discontinuous changes of properties, i.e. intermediate states of mixed properties do not exist making a fine tuning of solid state parameters difficult. For some molecules, the number of accessible polymorphs (and material properties) might be quite

limited, as in the case of iminostilbene and phenothiazine which both are known to have only one crystal arrangement. Hence, desired material properties cannot be achieved by simple polymorph change.

In order to overcome some of these limitations, a second compound can be added during crystallization which eventually incorporates into or interferes with the crystalline packing. Such co-crystallization techniques yield new solids, which might show improved properties otherwise inaccessible by the crystallization of the pristine compound.^{97,101} Co-crystallization can be utilized in pharmaceutical applications in order to improve the properties such as increased aqueous solubility and bioavailability. A co-crystal assembles with long range order so that only defined stoichiometric ratios of the constituents can result in a well ordered crystal. This again prevents continuous tunability and discontinuous adjustment of material properties remain.

An intriguing approach to obtain continuous tunability or modulation of material properties is based on the addition of atoms or molecules in non-stoichiometric amounts. In inorganics but also organics¹⁰², this is referred to as doping and in metals the addition leads to alloy formation. For certain combinations of organic molecules, the formation of solid solutions rather than co-crystals has been observed.¹⁰³ In such assemblies, the crystal lattice sites are still well defined as in pristine crystals, however the constitutions occupy some of the crystal lattice sites in a random fashion.¹⁰⁴⁻¹⁰⁶ The simultaneous existents of different molecular species alter some of the material properties which might be the electronic structure, solubility, long time stability, amongst others.¹⁰⁷ However, crystallization is generally considered as one of the most effective purification techniques as an arbitrary multicomponent mixture will most likely undergo phase separation on changes in thermodynamic parameters leading to pure single molecular species crystals. Such behavior also applies for co-crystallization where specific packing is only possible at specific conditions. In general, for a crystalline solid state solutions the molecular size and crystalline packing of the individual constituents need to fulfill requirements regarding the similarity in molecular sizes and crystalline packings to obtain crystalline solid solutions.^{104,105} From a thermodynamic point of view this means that the interaction energy between the different constituents is approximately equal to the interaction between equal molecules, thus no energy can be gained by phase separation and a solid solution is obtained. The dominating effect is than

the maximization of entropy.¹⁰⁸ (Similar considerations might also apply for amorphous solid state solutions, but as there is no lattice to be filled, some constraints might be different, i.e. similarity in molecular size might not be necessary). Having identified sufficiently compatible molecules by data base search or educated guessing, the properties of such mixed crystals can be tuned continuously over a wide range simply by changing the relative amount of the constituents. In the ideal case, a linear relation between the mixing ratio and material properties can be achieved which enables precise adjustment of material properties.^{109,110}

In recent years, studies focused on the understanding of the prerequisites for obtaining mixed crystals.¹⁰⁵ Systems with up to three small organic molecular constitutions could be identified, showing the versatility and potential of these systems whereby mostly bulk solution experiments were applied.^{106,111} In this study, we demonstrate a binary model system consisting of small pharmaceutical relevant molecules, namely phenothiazine (PTZ) and iminostilbene (ISB), which are of similar molecular size and share a common crystalline packing (see Figure 4.26). Rather than relying on bulk crystallization or mechanochemical synthesis, application relevant thin film technique such as solution casting (drop casting) were utilized to grow thin crystalline layers directly on solid surfaces increasing the functionality within potential applications. Using such techniques allows for changing of the film thickness and growth kinetics based on choice of solvent and evaporation rate. In order to demonstrate the continuous and non-stoichiometric nature of this system, changes in structural behavior are investigated by a combination of various X-ray diffraction techniques and the effect on the exemplary property of UV-Vis absorption is discussed.

4.3.4 Methods

Materials. Phenothiazine (PTZ, 98%) and Iminostilbene (ISB, 97%) were purchased from Sigma Aldrich (Munich, Germany) and used without further modifications. Solutions of various concentrations (0.65 mg/ml up to 20 mg/ml) of PTZ and ISB were prepared in spectral-grade tetrahydrofuran (THF) (Fluka, Germany) at room temperature using a magnetic stirrer for several hours. The intermixing of the molecules was performed in solution by combining solutions of pristine PTZ and ISB of equal concentration in different ratios of 1:1 up to 1:4 and vice versa. Since the molar mass of PTZ (199.27 g/mol) and ISB

(193.25 g/mol) are much alike, the mixed volume ratios can also be considered approximately molar ratios.

Thin films of the molecules were prepared on conventional microscopy glass slides (Roth, Germany) cut into 10×10 mm or 25×25 mm pieces. Cleaning was performed by ultrasonication for 15 minutes in ethanol and acetone followed by immersing the substrates in NaOH solution (0.4 mol) for 60 minutes to remove organic residuals and to activate the surface facilitating a more hydrophilic surface. Between steps, substrates were rinsed using MilliQ water and dried using a nitrogen stream.

Sample Preparation. Thin films of the pristine and mixed compounds were created by drop casting. Drop casting was carried out by placing a droplet of 25 μ l on a 10×10 mm glass substrate and immediately covered with a petri dish to reduce the evaporation rate. Films were allowed several hours to completely crystallize before the cover was removed.

Structural Investigations. Optical microscope images were taken with an Axiovert 40 microscope (Zeiss, Germany) equipped with polarizers and a digital camera. Specular X-ray diffraction was conducted using a PANalytical EMPYREAN diffractometer fitted with a Cu-sealed tube ($\lambda = 0.154$ nm). The primary side, before the sample, is equipped with a parallel beam collimator, 20 mm beam mask and a $1/8^\circ$ primary slit. On the secondary side, after the sample, a PANalytical PIXcel3D detector is mounted with 0.02° Soller slits and a 7.5 mm anti-scatter slit. The detector was operated in 1D mode. Data was converted into reciprocal space using $q_z = 4\pi/\lambda \sin \theta$, with q_z being the out-of-plane part of the scattering vector (perpendicular to the sample surface) and θ being half of the diffraction angle 2θ . Crystallographic investigations of the in-plane order were conducted at the X-ray diffraction beamline (XRD1) at the ELETTRA Synchrotron, Trieste (Italy)¹¹² employing grazing incidence X-ray diffraction (GIXD). The beamline was setup with a Dectris Pilatus 2M hybrid-pixel area detector. The wavelength was set to 0.154 nm. The incidence angle was set to 0.5° , which is well above the critical angle of approximately 0.15° for organic films. Using higher incidence angles minimizes the beam footprint on the sample significantly and in turn increases the resolution. In order to overcome the poor statistics of the drop casted samples containing large crystals (do not resample proper 2D powders), an azimuthal rotation was applied during the data collection to collect a complete data set containing all diffrac-

tion peaks regardless of the azimuthal orientation of the crystals with respect to surface. The pixel data was converted into reciprocal space and visualized using custom-made MATLAB code.

Singe crystal data collections were performed at the same beamline (XRD1). Samples were obtained by removing individual crystals from the surface with small fragments of adhesive tape. Complete datasets were collected at room temperature and 100 K through the rotating crystal method, using a glass fiber to support the crystals attached to the tape. Data were acquired using a monochromatic wavelength of 0.700 Å on the same Pilatus detector. The diffraction data were indexed and integrated using XDS.¹¹³ Scaling were done using CCP4-Aimless code.^{114,115} As crystals are recovered from a thin film these appear as very thin elongated plates with limited diffracting power (0.9–1.0 Å). The structures were solved by the dual space algorithm implemented in the SHELXT code¹¹⁶. Fourier analysis and refinement were performed by the full-matrix least-squares methods based on F2 implemented in SHELXL-2014¹¹⁷ and the modeling was performed using the Coot program.¹¹⁸

4.3.5 Results

Morphology. The deposition of either ISB or PTZ via drop casting results in the formation of homogenous layers which directly after deposition are crystalline, i.e. a metastable amorphous state is not observed. In Figure 4.20 images of such films are depicted. For the pristine ISB dendritic structures develop. These structures seem to order regularly with respect to others so that a regular pattern of perpendicular forming branches appears. Overall, such regular regions run over large distances which even might exceed the image size.

For PTZ also regular patterns are observed but with the structure size being much larger; the width is about 5–7 times larger compared to those in the ISB sample. Furthermore, only some of these structures have additional branches that are about 90° off the main direction. Mixing ISB and PTZ in a ratio of 1:1 this results in the morphology developing into an intermediate type structure. Regular dendrites run several hundreds of μm over the sample surface and eventually a side branching is noticed. The mixed structure width is reduced significantly compared to the pristine PTZ but is larger compared to those in the pristine ISB sample.

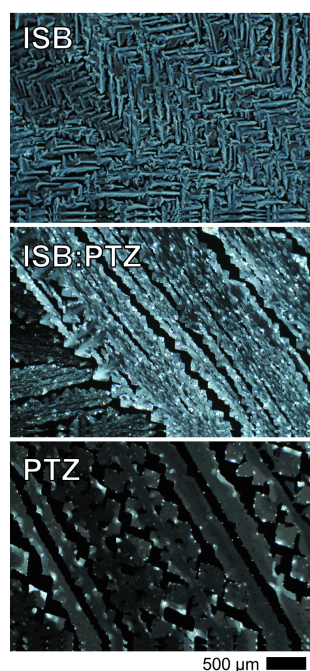


Figure 4.20: Optical micrographs showing the morphology of the pristine drop casted iminostilbene (ISB) and phenothiazine (PTZ) films. Center image shows the ISB:PTZ mixed crystal morphology.

Specular X-ray Diffraction. The information contained in a specular X-ray diffraction scan is limited to net planes parallel to the substrate surface. This information is already a reliable tool to detect even very small crystallographic changes within thin film samples. Hereby one can distinguish PTZ and ISB co-crystal formation, phase separation or combinations thereof. As a baseline for further evaluations the pure/pristine materials were measured and data are depicted in Figure 4.21. Using drop cast samples, the number of measured Bragg peaks for both compounds is low; either two or three peaks, for ISB and PTZ, respectively, in the range up to $q_z = 13 \text{ nm}^{-1}$ were detected. The equidistant occurrence of these peaks and the lack of others means that a strong preferred crystalline orientation with respect to the substrate surface is present.

Comparison with literature (obtained from the Cambridge Structural Database, CSD code: PHESAZ01 and BZAZPO) allows identifying a (010) texture for both films, making the observed peaks at $q_z = 5.99 \text{ nm}^{-1}$ and 6.14 nm^{-1} the 020 peak of the respective material with an interplanar distance of either $d_{\text{PTZ}} = 1.049 \text{ nm}$ or $d_{\text{ISB}} = 1.023 \text{ nm}$. Due to the orthorhombic unit cell, these d -spacings are exactly half of to the respective lattice constants b . Peaks at higher

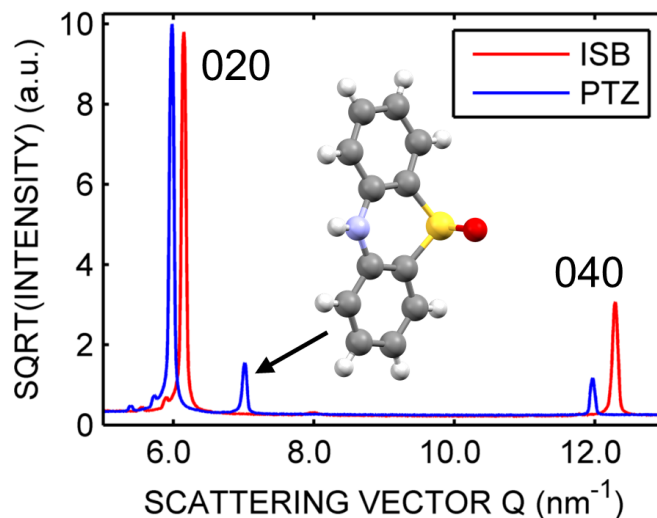


Figure 4.21: Specular X-ray scans of iminostilbene (red) and phenothiazine (blue) samples. Inset shows the molecular structure of phenothiazine-5-oxide.

q_z values are simply higher order of these net planes e.g. (040), (060). Using the specular scan, it can be concluded that the difference in the packing along the surface normal is small but the setup in use is sufficient to achieve a resolution of the individual components if phase separations exist.

The small features on the left tails of the (020) peaks are parasitic lines of the X-ray tube (copper K_β and tungsten L_α radiation) passing through the multi-layer mirror. For PTZ another peak at 7.03 nm^{-1} exists which is not explained by the orthorhombic crystal structure of pure PTZ. In fact, this peak is a result of another chemical compound being present; phenothiazine-5-oxide which formed due to oxidation of phenothiazine in solution (vide infra).

Specular scans of films containing different ratios of PTZ and ISB are shown in Figure 4.22. Regardless of the mixing ratio tested, the diffraction patterns remain similar to the pristine compounds. Each pattern is dominated by an intense peak located in the range of $q_z = 5.99 \text{ nm}^{-1}$ and 6.14 nm^{-1} which is in between the peak position of the pristine materials (higher orders thereof are also measurable but data is skipped for clarity/resolution). For instance, a mixing ratio of PTZ:ISB of 2:1 results in the peak maximum being shifted to slightly larger values compared to the pure PTZ and directly translates into a changed net plane distance of 1.044 nm. Assuming a packing that remains similar to the pristine materials, this suggests the crystal b -axis of the initial

PTZ crystal is changed due to the intermixing even though the PTZ remain the majority species. Adding more ISB result in the peak shifting further towards the pristine ISB peak position at $q_z = 6.14 \text{ nm}^{-1}$. The adjustment of the peak position is hereby only a function of the ratio of the two components. For all of the samples, the peak shape is identical with an FWHM of approximately 0.07° which suggests that there is no significant peak broadening on account of crystalline strain due to the intermixing or crystal size.

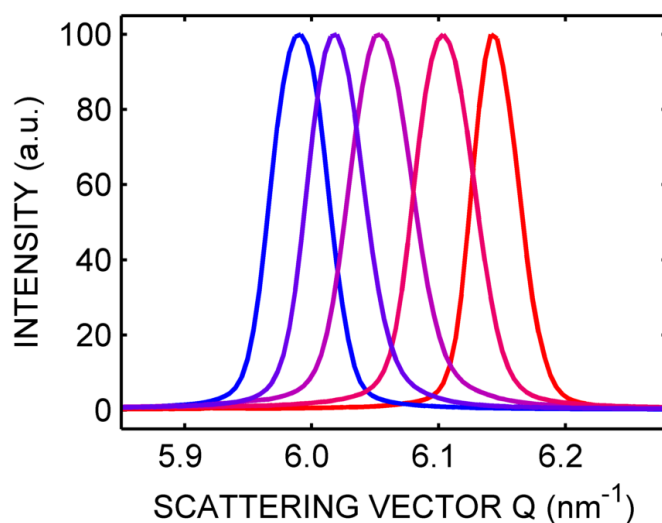


Figure 4.22: High resolution scan of the q -region covering the 020 peak showing peaks for pure and mixed crystals with molecular ratios PTZ:ISB of 2:1, 1:1 and 1:2 (left to right). The intensities are normalized for easier comparison.

Grazing incidence X-ray diffraction. Information obtained by specular scans are limited to net planes which are parallel to the substrate surface. Changes regarding the order along the substrate surface (in-plane) cannot be detected directly. For studying the in-plane order grazing incidence X-ray diffraction is employed. Following the same principle as before, pristine films are investigated first and compared to mixed crystal samples. The reciprocal space maps (RSM) in Figure 4.23 show the diffraction pattern of drop casted ISB and PTZ films. In reciprocal space maps, the scattering vector \mathbf{q} is represented by the x -axis which corresponds to the in-plane part q_{xy} and the y -axis which holds information about the out-of-plane direction and is therefore referred to as q_z . The intensity is represented by black labels with darker areas being of higher diffraction intensity.

The reciprocal space map for ISB shows one strong peak along to the co-planar

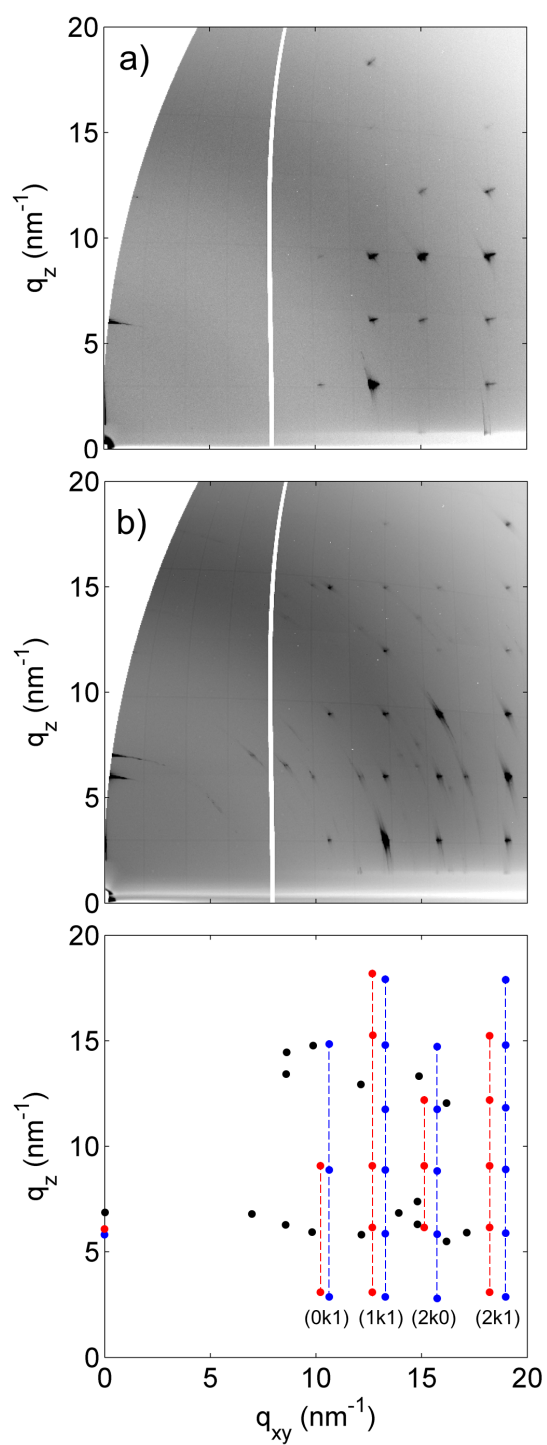


Figure 4.23: Reciprocal space maps of iminostilbene (a) and phenothiazine (b) with corresponding indexation (c) in blue and red. Dots mark the position of individual peaks along various Bragg rods (dashed lines). Black dots mark positions of phenothiazine-5-oxide peaks.

region at $q_{xy} \sim 0 \text{ nm}^{-1}$ which is the Bragg peak tail of the intense (020) reflections as already observed in the specular X-ray scans (a specular scan at $q_{xy} = 0 \text{ nm}^{-1}$ cannot be extracted from such a GIXD measurement). In the in-plane region ($q_z \sim 0 \text{ nm}^{-1}$, $q_{xy} > 0 \text{ nm}^{-1}$) the first peak appears at around 10 nm^{-1} and others follow at $q_{xy} \sim 13, 16$ and 19 nm^{-1} . Having the first value at about 10 nm^{-1} means the d -spacing is about two times smaller than the packing parallel to the surface as identified by specular scans. Such a behavior is prototypical for rod like molecules assembling in a standing orientation, which in case of IBZ means the crystal contact the silica surface with the 010 plane. Inspecting the region out-of plane at positions $q_{xy} \neq 0 \text{ nm}^{-1}$ many other peaks are found; in fact, the RSM for ISB shows four diffraction rods located at $q_{xy} = 10, 13, 16, 19 \text{ nm}^{-1}$ with diffraction peaks being observed up until $q_z = 20 \text{ nm}^{-1}$ (or even beyond). This means that several peaks of distinct d -spacing share a common in-plane component. This simply results from the orthorhombic crystal lattice of IBS. Using the information each peak can be unambiguously attributed to a single Miller index whereby individual rods can be correlated to constant h and l (the Miller indices) and a varying k index. All the peaks appear nearly spot-like indicating very little mosaicity (misalignment) being present. The smeared intensity along the radial direction can be attributed to the size of beam footprint on this very sample.

The RSM of films containing only PTZ reveal a more complex pattern (see Figure 4.23b and 4.23c). Firstly, a diffraction pattern very similar to these of pristine IBS films is noted. This is somehow expected due to the fact that both crystal systems are in the same space group ($Pnma$) and same orientation with respect to the sample surface. However, due to the smaller lattice constants a and c of PTZ, the Bragg rods shift to higher q_{xy} values compared to those of ISB and the peak intensities differs due to the slightly different molecular composition and packing (structure factors). Most prominently the peak located at $(q_{xy}, q_z) = (15, 3) \text{ nm}^{-1}$ is missing, meaning that the structure factor is (nearly) zero. The peaks are slightly more smeared out along the Debye-Scherrer rings, meaning the mosaicity in this PTZ sample seems to be higher compared to ISB.

Besides the peaks arising from the PTZ crystals there are other peaks noted. These peaks are not along rods of constant q_{xy} . As mentioned earlier, PTZ samples reveal crystals of slightly different chemical composition, i.e. the for-

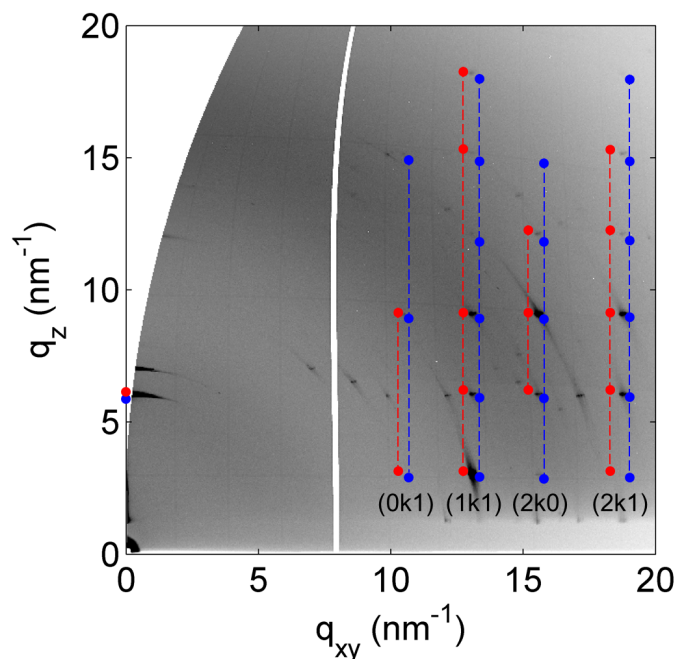


Figure 4.24: Reciprocal space map of a phenothiazine-iminostilbene mixed crystal with 1:1 ratio. Red and blue dots indicate the diffraction positions of the pure iminostilbene and phenothiazine, respectively.

mation of phenothiazine-5-oxide (PTZ-O) crystals takes place which results in these additional peaks which are less intense compared to those of PTZ. Using the structure solution as obtained by single crystal diffraction (vide infra), these peaks can be indexed similar to the others and are indicated by black markers in Figure 4.23c.

The intermixing of PTZ and IBS in the ratio of 1:1 results again in crystals with clear diffraction signal as depicted in Figure 4.24. The mixed samples share the same features as the pristine films with rods emerging at defined q_{xy} values. Putting the peak positions of the pristine materials onto the RSM shows that the position of the mixed samples are at intermediate positions similar to the specular scan which means that the unit cell also changed accordingly. Besides the strong peaks there are several weak diffraction peaks present, which again are a result of the PTZ-O crystals.

Single Crystal Diffraction. By carefully removing the crystals from the supporting substrates it was possible to conduct single crystal diffraction on larger individual crystals of PTZ, ISB and mixtures thereof. In order to verify the

Table 4.1: Crystallographic lattice constants given in Å of iminostilbene (ISB), phenothiazine (PTZ) and mixed crystal with 1:1 ratio (ISB:PTZ) as obtained by single crystal diffraction at room temperature (RT) and 100 K.

	long (Å)		medium (Å)		short (Å)		β (°)	
	RT	100 K	RT	100 K	RT	100 K	RT	100 K
ISB	20.45	20.14	8.24	8.08	6.04	6.03	90	90
ISB:PTZ	20.92	20.59	8.17	7.96	6.05	5.98	90	90
PTZ	20.98	20.78	7.92	7.79	5.90	5.82	90	95

crystalline phase and to take possible temperature effects into account, the pristine crystals were characterized at room temperature and at 100 K to minimize thermal disturbance and to check for possible phase transitions. The lattice constants for the individual compounds and for the 1:1 mixed crystal are summarized in Table 4.1. Structure solutions at room temperature of the pristine materials match those provided in literature (CSD codes BZAZPO and PHE-SAZ01) meaning that the accuracy of our approach even though from thin films can be used to gain knowledge on the full structure. The indexation of the single crystal diffraction data for the mixed crystals reveals again an orthorhombic unit cell and the same space group ($Pnma$). Inspection of the unit cell dimensions reveal that intermixing reduces the ISB unit cell along the a -axis, increases along the b -axis but remains very similar along c .

From this experiments, also crystals of PTZ-O could be removed from the sample surfaces and single crystal X-ray diffraction experiments could be performed. The evaluation of the data reveals a monoclinic unit cell containing phenothiazine-5-oxide, a phenothiazine molecule with an oxygen atom bonded to the sulfur atom (see inset Figure 4.21)

UV-Vis Spectroscopy. To investigate the impact of intermixing on some properties, UV-Vis adsorption spectroscopy was measured (see Figure 4.25). For the pure ISB sample, the UV-Vis spectrum reveals a clear maximum at around 311 nm and a very shallow maximum at around 400 nm. For pristine PTZ the UV-Vis spectrum shows a clear maximum at 332 nm which is shifted by 21 nm with respect of the pristine ISB suggesting that the conjugation length is slightly longer in the PTZ sample.

On the mixed crystal sample (ratio 1:1), the UV-Vis spectrum appears as an

intermediate situation with the maximum being at 324 nm. Other maxima in this region are absent. In a similar manner, the maximum changes as the relative amount of ISB and PTZ changed. In general, it can be said, the maximum of absorption maximum shifts towards larger wavelength as PTZ amount increases. In the limit of accuracy, this behavior can even be described using approximately a linear relation.

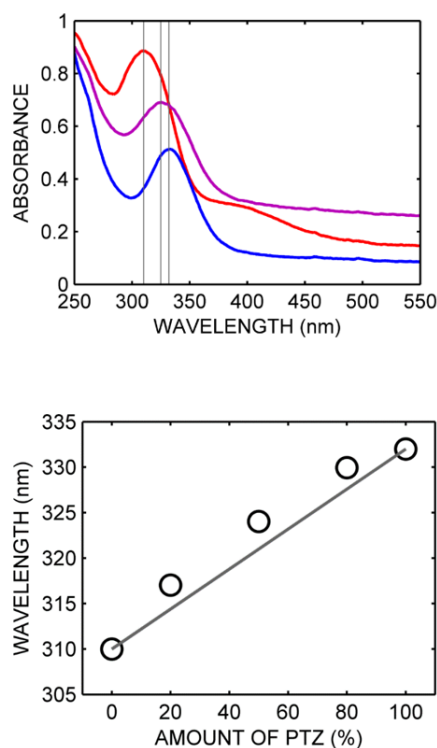


Figure 4.25: Top: Optical absorbance for iminostilbene (red), phenothiazine (blue) and a PTZ:ISB mixed crystal (purple). Vertical lines indicate individual peak positions. Bottom: Optical wavelength shift of an absorption peak for mixed crystals with various mixing ratios. The grey line is a guide to the eye and indicates the linear change between the absorption peak wavelength of the pure materials

4.3.6 Discussion

Structural properties. Iminostilbene and phenothiazine share similar molecular geometries, two benzene rings fused to an azepine group in the case of ISB and to a thiazine for PTZ (see Figure 4.26). Each molecule shows a characteristic bend around the center which is defined by the chemical composition of the

center group; ISB bends approximately 27° and PTZ bends 21° on account of exchanging the two carbons by a sulfur atom in the center unit. Considering the chemical similarities of the molecules it is not surprising that their molecular packing is much alike i.e. they are isomorphous. Both compounds crystallize in an orthorhombic unit cell in space group $Pnma$ hosting four molecules. The lattice constants are given in Table 4.1. The variation of the lattice constants of ISB and PTZ crystals is a direct consequence of the different bending angles, making the ISB molecules shorter but broader with regard to the close-packing principle.¹¹⁹

While these two molecules pack similar their film forming capabilities are different. For instance, the structures in the PTZ films are much larger and the dendritic branching is less frequent. This means PTZ films have a preferred growth direction along one specific facet when samples are prepared similarly to the ISB film. The higher frequency of branching in the ISB means that other directions are only slightly disfavored. In addition, PTZ films have a significant higher mosaicity compared to the ISB films which means that the order with respect to the silica surface is less pronounced. For some samples of higher concentration (>10 mg/ml) even the formation of additionally diffraction rings (Debye-Scherrer rings) are observed indicating some powder-like film characteristics of less preferred orientation. For the ISB such ill-defined directions do not develop even at larger concentration. This might suggest that the PTZ growth is likely already taking place in solution where interaction with the substrate surface are less pronounced so that more random orientations can develop.

Drop casting iminostilbene and phenothiazine on silica surfaces results in either case in the formation of textured polycrystalline crystalline films after solvent removal. This is reflected by the specular X-ray diffraction scans presented in Figure 4.21 which only shows 020 peaks and higher orders thereof. From this follows that for both pristine materials the (010) plane which contains the a and c unit cell axis, is parallel to substrate surface. This orientation is further proven to be correct by the indexation of the RSM obtained from the GIXD measurements. It should be noted, that a specular scan might already provide some evidence for a preferred orientation but as other peaks might be of low diffraction power or textures without the presence of a specular peak might exist error in the interpretation may result on considering only the specular scan.

GIXD is an excellent tool to evaluate preferred orientation in more detail. The preferred 010 crystal orientation means that for both materials the molecules are standing upright with regard to the substrate surface i.e. the long molecular axis is approximately perpendicular to the substrate surface. Such a behavior is often observed for small rod-like molecules of poor or weak surface interactions; in a standing configuration, the contact with the substrate minimizes and the van der Waals forces in between molecules dictate crystal formation.⁷ In case of pure ISB this results in more than one favorable direction of crystallization with many side branches and in the case of PTZ crystal growth preferable along a single direction.

Intermixing or co-crystallization from solution can yield different results depending on the individual compounds.¹⁰³ Most basic consideration is a simple phase separation as exploited in purification processes i.e. the compounds crystallize individually. In such a case, the X-ray diffraction patterns are simple a result of the superposition of the individual compounds and can be easily identified. In contrast a co-crystal, in which the compounds pack in a common well-defined arrangement produce a unique characteristic X-ray diffraction pattern which can be explained by a single unit cell and typically deviates from the pristine compounds. However, crystallizing mixtures of ISB and PTZ showed clearly deviating behavior. First of all, phase separation, regardless of the mixing ratio can be excluded, since the specular X-ray diffractograms and RSM showed diffraction explainable by only a single unit cell. From a thermodynamic point of view interaction energies between the different constituents should be approximately equal to the interaction between equal molecules, thus no energy can be gained by phase separation and a solid solution is obtained, or in other words the entropy is the driving mechanism to for the intermixing.

Another likely more important property of these samples is that the positions of the peaks clearly depends on the relative amount of ISB and PTZ being present (see Figure 4.22 and 4.24). In the specular scan, the 1:1 mixing ratio results in a 020 peak position located clearly in the middle of the pure compound peaks. Using other ratios of 2:1, 3:1 and vice versa causes a shift of the peak position in direction of the majority compound with the pure compound peak position being the limit. The shift of the 020 peak position translates directly into a change in the lattice constant $b = 2 \cdot d_{020} = 4\pi/q_{z,020}$ due to the orthorhombic unit cell which means a d -spacing between 1.023 nm and 1.049 nm can be set.

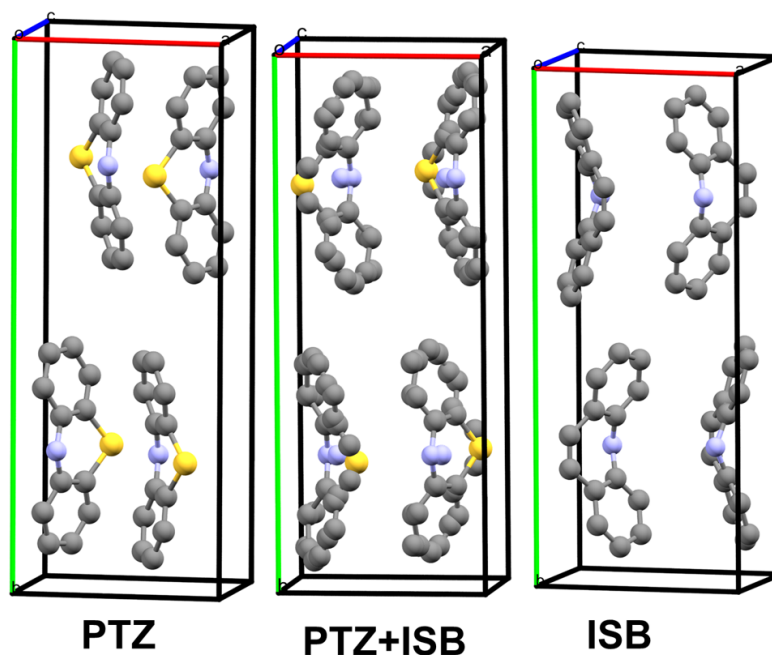


Figure 4.26: Molecular packing of phenothiazine (left) and iminostilbene (right) showing four molecules per unit cell. The center shows the molecular packing of the mixed crystal system with a superposition of the individual molecules.

The shift in the region tested depends even linearly on the molecular mixing ratio. Such behavior is known as Vegard's Law, describing an approximately linear relation between the lattice shift and composition of a compound.¹⁰⁹ In the limit of accuracy, a stoichiometric relation is not necessary to achieve certain cell expansions and thus arbitrary unit cell size can be obtained within the limits of the pristine compounds. One should also note that the mixing ratio is based on the weight ratio in solution, which means that the actual molecular ratios in the mixed crystal might differ slightly, due to some conversion of PTZ in PTZ-O which could be reduced by using other solvent or inert conditions.

Testing the other unit cell directions might be achieved using the GIXD measurement by carefully checking the peak position. But as the setup in use was of low resolution such evaluation might be of larger error. Further, full structure solutions from thin films in GIXD geometry is particularly challenging as the number of accessible peaks is low.¹² Exemplary, the full unit cell of a mixed crystal was determined using another approach. Usually thin films of organic molecules such as the current PTZ and ISB are not suitable for single crystal

diffraction since crystallization was performed directly on a supporting substrate. Nevertheless, as the interaction of the molecules with the silica substrate is weak, individual crystals could be peeled off the substrate. On these the single crystal measurement could be performed. To proof our sample preparation approach single crystal of the pristine materials were measured first at room temperatures and 100 K. The complete structure solutions for pure ISB and PTZ compounds obtained at room temperature compare very well to the reference structures available at the Cambridge Structural Database (PHESA01 and BZAZPO, for PTZ and ISB, respectively). At lower temperatures, a considerable thermal unit cell lattice shift is noted as expected (see Table 4.1). A PTZ phase transition, from an orthorhombic to a monoclinic crystalline form, upon cooling, suggests that interphase mixing efficiency and crystal packing of mixtures can be influenced by temperature.

The structure solution for the mixed crystal yielded an orthorhombic unit cell with space group $Pnma$, thus identical to PTZ and ISB. The lattice constants are an intermediate case of the pure compounds which was already expected from the results of the specular and GIXD measurements. In fact, using the new unit cell parameters enables also to index all peaks in the RSM of the 1:1 mixture (see Figure 4.24). This means that also for the intermixing situation the crystal peel-off (mechanical stress) does not affect the unit cell or in other words the polymorphic form remains unchanged.

Having the opportunity to perform single crystal data analysis, even more insightful information about the molecular packing is obtained by a full structure solution. Similar to the pristine materials, the unit cell of the intermixed sample hosts four individual entities. Other than in the pristine sample case, the well-defined molecules appear as a superposition of PTZ and ISB molecules after structure refinement. This can be understood as a statistical probability of occupation of a specific lattice site by either a PTZ or ISB molecule, with the probability depending on the molecular mixing ratio.

Having a system which can exchange any molecule by another species in an arbitrary amount is in strong contrast to a typical co-crystallization process, where the components (molecules) share a defined unit cell in stoichiometric exact number and excess material usually undergoes a phase separation, i.e. crystallized independently. However, in the case of PTZ:ISB crystals no hints of the pure compounds are noted in the X-ray scans, meaning the minority molecules

get fully incorporated in to the majority compounds lattice. For small amounts, one could think of the minority molecules as defects or dopants¹²⁰, however in the case of a 1:1 mixing a definition of minority/majority molecules becomes meaningless. Furthermore, the width (FWHM) of the specular peaks is comparably similar for different molecular ratios, suggesting that the incorporation does not induce stress on intermixing as it would be the case for a simple defect structure. Such particular behavior is reminiscent of inorganic solid solutions such as metal alloys or intermetallic compounds which feature a continuous crystal lattice depending on the constituent ratio. This particular behavior is due to the completely miscibility of the compounds and in turn enables the continuous modulation of material properties. The lack of a miscibility gap for organic molecules is rarely observed but may provide some additional tuning capabilities interesting for a variety of fields.

Solid solutions of organic systems have been observed previously, and are most prominently described by Kitaigorodsky, who found that isostructurality and isomorphicity are prerequisites for obtaining organic solid solution rather than phase separation.^{104,105} In the example of iminostilbene and carbamazepine Christian et al. showed that iminostilbene (being the chemical precursor in carbamazepine synthesis) can assist in the faster carbamazepine growth and even epitaxial growth was detected, but the formation of co-crystals or solid solutions could not be found.¹²¹ This highlights the importance of isostructurality for miscibility on a molecular level.

As a consequence, on the statistical molecular exchange also some of the solid state properties change. Here the example of the shift in the UV-Vis absorption maximum as function of the relative amount is given. Other than in the liquid mixture the shift in the spectrum does not seem to be a superposition of peaks from PTZ and ISB. Furthermore, such a shift means that the addition of the other molecule actually changes the electronic structure especially those in the solid state. Thus, it seems likely that other solid state properties such as the melting point, mechanical stability is also subject to the molecular mixing ratio. Also, being capable of tuning the *d*-spacing might allow producing very defined Bragg reflectors for special purposed.

In many experiments, the presence of additional peaks is noted which means that either another polymorph or an impurity is present. Chemically, PTZ appears to be less stable due to the presence of sulfur in its structure. The single

crystal diffraction revealed PTZ reacted with oxygen to form phenothiazine-5-oxide (see inset Figure 4.21)¹²². This molecule crystallized during the processing and defined crystals developed. These crystals are of very high stability and in most solvents PTZ-O is insoluble. The amount of converted PTZ to PTZ-O is most likely very low, since the diffracted intensity of the PTZ-O is rather weak and more importantly the unit cell on intermixing seems to be mostly unaffected. However, the additional oxygen atom result in a more bulky structure which is more similar in shape to carbamazepine. Thus, taking Kitaigorodsky's rule regarding the isostructurality into account it is less surprising that PTZ-O did not take part in the solid solution.

4.3.7 Conclusion

Modifying physical or chemical properties of crystalline materials by polymorph selection or co-crystallization allows only for discontinuous or discrete changes in the materials structure and properties. This study demonstrated the use of molecular solid solutions or mixed crystals to overcome some of these limitations. Thin films of pristine phenothiazine (PTZ) and iminostilbene (ISB,) prepared by solution cast techniques (drop casting), show a uni-axially texture with the long molecular axis being perpendicular to the substrate surface. Upon intermixing the molecules in solution prior solution casting, the overall film texture of 010 prevails, however, formation of characteristic mixed crystals occurs. Regardless of the molecular mixing ratio, a mixed crystal thin film is obtained with no indications of phase separation being present. Varying the PTZ:ISB ratio leads to an approximately linear shift of the lattice constants as determined by specular and grazing incidence X-ray diffraction. Moreover, complete structure solution by means of single crystal X-ray diffraction clearly reflects the statistical nature of lattice site occupation for mixed crystals of PTZ and ISB. Because of the complete miscibility of PTZ and ISB, a continuous modulation of the lattice constants was possible. Moreover, continuous modulation of many physical or chemical properties, as exemplary demonstrated for the UV-absorption behavior, can be expected, making the mixed PTZ:ISB compound an intriguing system for further studies and for potential applications of mixed crystals.

4.3.8 Acknowledgement

The work was funded by the Austrian Science Fund (FWF): [P25541-N19]. Elettra Sincrotrone is acknowledged for providing synchrotron radiation at the XRD1 beamline. Luisa Barba we gratefully thank for her excellent support during the GIXD measurements.

4.4 Single step processing for epitaxial growth of a drug on an organic template: Example of carbamazepine on iminostilbene

Hans Riegler,¹ Paul Christian,² Christian Röthel,^{1,2} and Oliver Werzer¹

¹Institute of Pharmaceutical Sciences, Department of Pharmaceutical Technology, University of Graz, Austria

²Institute of Solid State Physics, Graz University of Technology, Austria

4.4.1 Preface

This section is based on preliminary results of crystal alignment investigations using the the method of pole figure reconstruction. The results are part of an ongoing study by Oliver Werzer regarding the crystal growth of carbamazepine in vicinity of iminostilbene. X-ray measurements and X-ray pole figure reconstructions as well as the crystallographic evaluation were conducted by the author of this thesis. Hans Riegler carried out the sample preparation and optical microscopy. The preparation of the final manuscript will be carried out by Oliver Werzer and Hans Riegler.

4.4.2 Introduction

The studies on the carbamazepine/iminostilbene system conducted by Christian et al. revealed a drastically enhanced crystallization rate of carbamazepine if both materials are intermixed in solution and crystallized on solid substrates.¹²¹ Moreover, carbamazepine appears to crystallize in a needle-like crystal habit on top of iminostilbene crystals. The carbamazepine needles are found to grow along distinct directions, an indication that directed crystal growth is taking place. However, the determination of the epitaxial relation during this study was not possible since standard grazing incidence X-ray diffraction does not provide the necessary azimuthal information. In order to improve the understanding of the interaction of carbamazepine with iminostilbene, samples of epitaxially grown carbamazepine on iminostilbene were prepared. An essential part of this study is the determination of the epitaxial relation between the

compounds. The directed growth of carbamazepine is investigated using reconstructed pole figure based on 2D reciprocal space mapping (see Section 3.2).

4.4.3 Methods

Carbamazepine (CBZ) was purchased from Alfa Aesar (Ward Hill, USA). Iminostilbene (ISB) was purchased from Sigma Aldrich (Germany). Both were used without further treatment. Individual single and dual component solutions of varying concentrations were prepared in tetrahydrofuran (THF) of spectroscopic grade (Sigma Aldrich, Germany). Using solution casting techniques, samples of solely CBZ, solely ISB or CBZ-ISB mixtures were prepared either on conventional microscopy glass slides (Roth, Germany) or on single crystalline silicon wafers with native oxide layers and single side polish (Siegert Wafers, Germany). Both substrate types provide isotropic silica surfaces for undirected crystallization whereby no difference in terms of impact on crystallization of the organic crystals could be identified. For sake of measurements (microscopy or X-ray) either glass or silicon wafers were used to minimize measurements artefacts (transparency, amorphous background). The substrates were cut to size ($1 \times 1 \text{ cm}^2$ for drop casting and $2 \times 2 \text{ cm}^2$ for spin coating), sonicated in acetone, subsequently rinsed in ethanol and dried with compressed air. Drop casted samples were prepared by placing a $100 \mu\text{l}$ droplet onto a leveled substrate. To reduce the solvent evaporation rate, the samples were immediately covered with a petri dish. Spin coated samples were prepared by placing $100 \mu\text{l}$ of solution on a stationary substrate (static dispense) and subsequently spun for 60 s at 18 rpm.

Optical microscopy images were taken using a standard digital camera mounted on a Zeiss Axiovert 40 microscope assembled in transmission mode. For better contrast polarizers were used whereby their relative orientation was set for sake of visibility. Grazing incidence X-ray diffraction (GIXD) experiments were performed at the beamline XRD1 hosted at the Elettra Sincrotrone (Trieste, Italy). A wavelength of 0.14 nm was set and a Dectris Pilatus 2M detector was used. The setup was calibrated using a LaB_6 standard, ensuring reliable data transformation from detector pixels into reciprocal space (scattering vector notation). The incidence angle was set to 1° , which is well above the critical angle of organic films (approximately 0.15° at this wavelength). Using such high incidence angles reduce the beam footprint on the sample significantly, thus im-

proving the resolution. Data collection was carried out by azimuthally rotating the samples while taking integrated images every degree, thus probing the entire reciprocal space hemisphere above the substrate surface. Integrated images over the entire 360° turn are presented in a reciprocal space map. Pole figure reconstructions represent the distribution of one specific net plane distance d within the upper reciprocal hemisphere ($d = 2\pi/|\mathbf{q}| = \text{const.}$). The azimuth angle ϕ and inclination ψ are derived and the resulting data are presented in a stereographic projection. Detector calibration and all data evaluation were carried out using custom-made MATLAB scripts.

4.4.4 Results and Discussion

Preparing solutions of both materials, iminostilbene and carbamazepine, in tetrahydrofuran allows for the deposition of thin films. An example of a drop cast film is shown in Figure 4.27. Extended linear structures are found running along the surface, consisting of iminostilbene. Besides these, smaller needles are found superimposed onto those elongated structures. The latter exhibit the characteristic needle-like crystal habit of carbamazepine indicating that carbamazepine crystals are located on top of iminostilbene dendrites. Interestingly, the carbamazepine crystals exhibit specific orientations with respect to the underlying iminostilbene crystals, independent if they grow on top or from the side (see smaller structures attached to vertical needle in the center of Figure 4.27). Such a defined or directed crystal growth means that an epitaxial relation between the materials is present. From the optical micrograph it can be seen that the carbamazepine needles (red) are approximately inclined by 36° and 144° with respect to the iminostilbene needle (blue).

In order to determine the epitaxial relation, pole figures of both materials need to be measured. Having probed sufficient amount of reciprocal space by using azimuthal sample rotations and an area X-ray detector, pole figures for arbitrary net plane distances $d = 2\pi/|\mathbf{q}|$ can be reconstructed from the collected scattering vectors. In this case, pole figures for $|\mathbf{q}| = 1.09, 1.27$ and 1.42 \AA^{-1} were selected and presented in Figure 4.28. While one pole figure for each material should theoretically provide sufficient data to deduce the crystal alignment, it is often beneficial to compare the obtained crystal alignment to pole figures obtained for different sets of net planes for verification. Coincidentally, different materials might feature net planes which are close in the interplanar distance

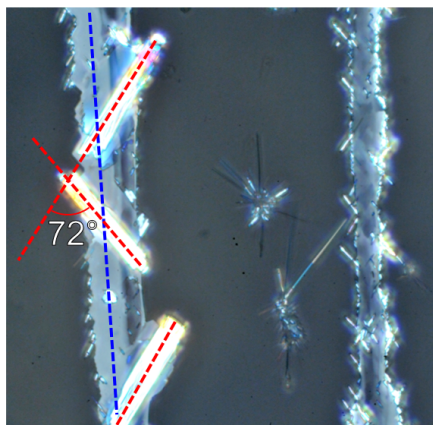


Figure 4.27: Optical micrograph of carbamazepine (red) needles growing on top of iminostilbene (blue) needles. Dashed lines indicate the long needle axes. Crystalline clusters in the center are carbamazepine growing directly on the glass substrate.

d and thus are recorded in the same pole figure. This is the case for carbamazepine and iminostilbene for scattering vectors of $|\mathbf{q}| = 1.09$ and 1.42 \AA (top and middle image in Figure 4.28).

Firstly, the blank area in the center is due to blind region in reciprocal space and is inherent to the fixed incidence angle geometry. Secondly, the blank ring-like regions are caused by the gaps between individual area detector elements. Moving on the actual crystallographic features, the most striking one are obviously the vastly different peak sizes. Starting with the pole figure for $|\mathbf{q}| = 1.09 \text{ \AA}$, six peaks are observable, two broad peaks and four smaller ones. The larger spots can be attributed to iminostilbene needles. Since, the crystalline iminostilbene needles are considerably larger, they also feature more pronounced diffraction peaks. However, one should note, that the actual peak size also depends partly on the intensity scaling since the tails of the iminostilbene peaks have a considerable amount of intensity compared to the smaller carbamazepine needles. In previous experiments iminostilbene has shown a preference for (010) crystal textures. Hence, a (010) contact plane is chosen, meaning the flat facets of the needles are assumed to be (010) net planes. Considering the molecular packing of iminostilbene (CSD code: BZAZPO) the growth habit can be easily understood. The molecules are orientated perpendicular with their long molecular axis with respect to the macroscopic flat facet, meaning the fast crystal growth directions are along the a and c axis, making growth along the surface more

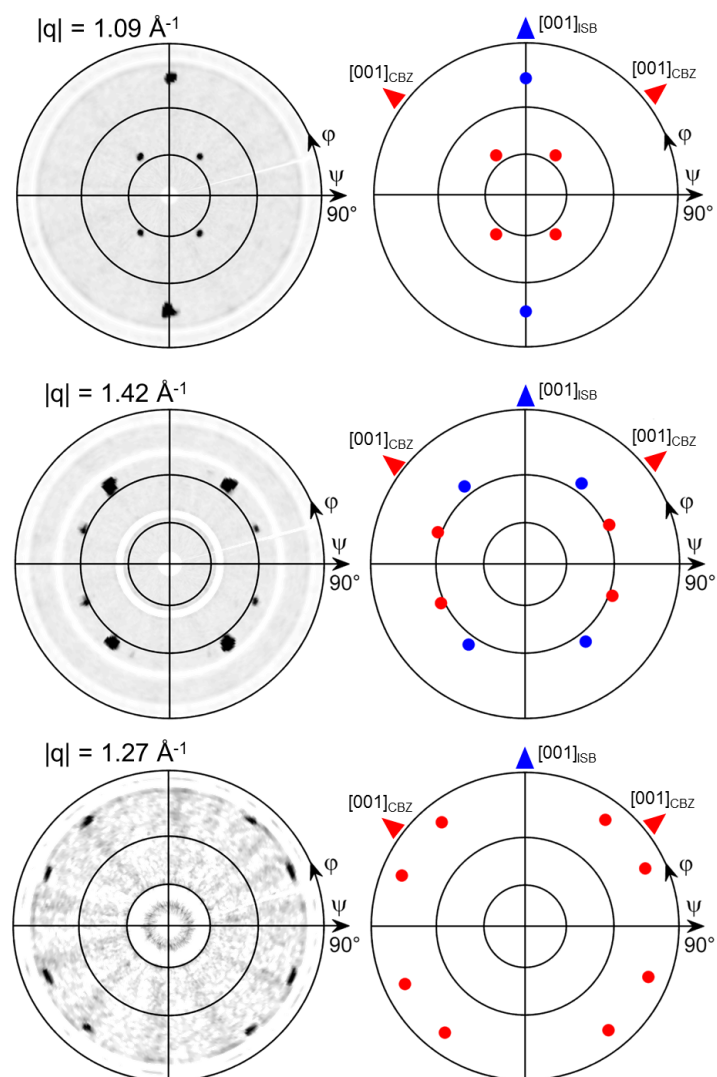


Figure 4.28: Reconstructed pole figures for carbamazepine (red) grown on iminostilbene (blue). Crystallographic real space directions of the compounds are indicated by colored arrows.

likely (see Figure 4.30).

Simulating the pole figure using the (010) contact plane makes the two large spots (blue) at an inclination angle of $\psi = 75^\circ$ the 011 or 01-1 reflection, respectively. The remaining four inner peaks (red) can be attributed to the trigonal carbamazepine form (CBMZPN03) with an (110) contact plane (see Figure 4.29). This means that the c -axis of the carbamazepine unit cell is oriented parallel to the substrate surface. In order to take all four peaks into account, two individual crystals with different alignments are necessary. Having indexed all peaks, the crystallographic or epitaxial relation can be derived. The crystallographic [001] direction (c -axis) of carbamazepine and iminostilbene are indicated by triangles in Figure 4.28. The carbamazepine c -axis is approximately rotated by $\pm 54^\circ$ (taking both crystal alignments into account) with respect to the iminostilbene c -axis. Thus, the relative azimuthal difference between the carbamazepine needles is about 108° (or 72°), which agrees very well with the optical micrographs depicted in Figure 4.27.

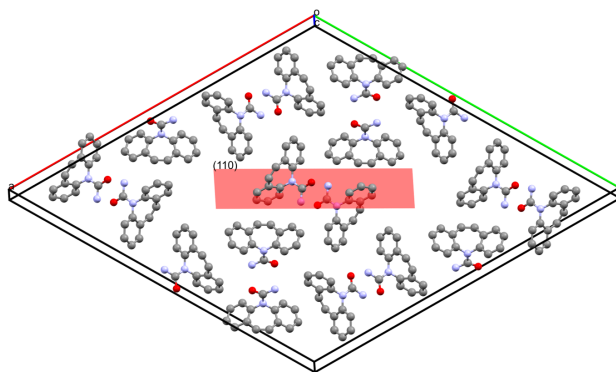


Figure 4.29: View along the c -axis of the carbamazepine unit cell. Red plane indicates the (110) crystal net plane.

Having established the direction of the different crystals, the molecular assembling can be investigated. Iminostilbene has a herringbone packing with the molecules being rotated with respect to adjacent molecules by about 70° (see Figure 4.30). Thus, the surface provides most likely very similar properties along two directions which are inclined by 70° due to herringbone packing. Furthermore, the inclination between the carbamazepine needles is 108° or 72° if one considers the complementary angle. Due to the similarity of the herringbone angle in the iminostilbene crystal packing and the relative inclination of the carbamazepine needles it seems very likely that the carbamazepine needles

align due to the presence of preferred surface directions which are connected to the herringbone packing of iminostilbene.

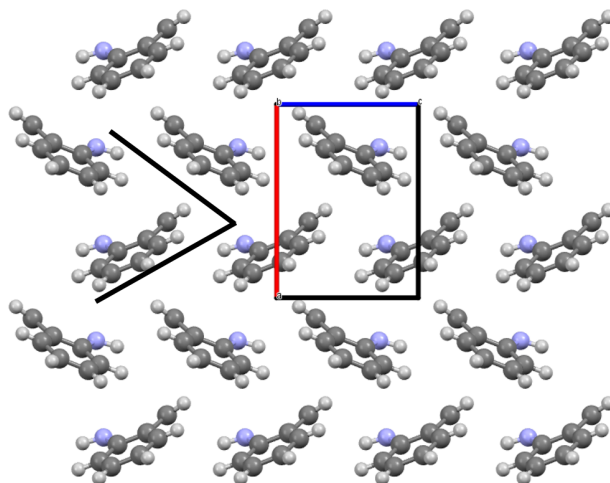


Figure 4.30: Molecular packing in the a - c plane of an iminostilbene crystal. Black lines indicate the herringbone angle of approximately 70° of the crystal packing.

4.4.5 Conclusion

The example of carbamazepine grown on top of iminostilbene crystals demonstrates the capabilities of pole figure reconstructions based on reciprocal space mapping using area X-ray detectors. Moreover, it demonstrates the advantage of reconstructing pole figure from large reciprocal data sets rather than directly measuring pole figures for specific netplane distances. For the data collection in this example, a single crystal diffraction beamline was utilized without modifications to perform the data acquisition. Also, having measured extensive regions of reciprocal space allows for further data evaluation such as screening for new polymorphs or solvate/hydrate formation with unknown crystal lattices. Having established the the epitaxial relation between iminostilbene and carbamazepine revealed an intimate connection between the herringbone packing of iminostilbene and the needle alignment of carbamazepine on top.

5 Conclusion

This thesis presented an approach to perform X-ray diffraction on weakly textured crystalline films which cannot be reliably characterized using standard X-ray diffraction methods. Weakly textured samples show still a defined contact plane with the substrate but lack the typical 2D powder statistic for the azimuthal crystal alignment. Thus, they can be considered an intermediate case of biaxially aligned films and fiber textured samples with proper 2D powder statistics. Unfortunately, static X-ray diffraction measurements like grazing incidence diffraction are not able to detect sufficient Bragg reflection for reliable crystallographic investigations. In contrast, methods for biaxially aligned samples which require extensive rotations around multiple axes, such as the pole figures technique, are often not feasible due to the extensive data acquisition times and rather specific experimental setups. However, the lack of a proper 2D powder statistics in weakly textured samples can be overcome by an additional azimuthal sample rotation during the data collection in combination with an X-ray area detector. Moreover, if individual diffraction images are recorded for each azimuthal step, one obtains most of the accessible diffraction information, which allows for specific data evaluation in reciprocal space depending on the sample texture. While this approach does not provide directly pole figures or reciprocal space maps, it is possible to reconstruct these common representations by means of data analysis in reciprocal space. Also, the demands on the experimental end station at synchrotron facilities are lowered, since extensive sample rotations as performed by a texture goniometer as used for investigating biaxially aligned samples are not required. Thus, grazing incidence diffraction setups, as offered at many synchrotron beamlines, can be used to study thin film samples regardless of their crystalline texture and access to valuable synchrotron experiments is more easily available.

Also technical aspects which arise from using X-ray area detectors were addressed in detail. An area detector calibration routine based on powder sam-

ples or primary beam images was developed based on a simulated annealing optimization. This allows for the determination of essential experimental parameters such as the sample-detector-distance and detector orientation. These parameters are crucial for the transformation of the detector pixel images into scattering vectors for further wavelength-independent data analysis.

The methods presented in this thesis were applied on various sample types ranging from biaxially to weakly aligned samples. While *classic* pole figure measurements can be utilized to study biaxially aligned crystallites with well-known crystallographic properties (lattice constants, contact plane) as used in the case of caffeine on single crystalline surfaces, such standard measurements could not be used to study weakly textured thin films as encountered in the case of phenothiazine-iminostilbene mixed crystals. Using additional azimuthal rotations allowed for the reliable measurement of reciprocal space maps and in turn for the determination of the continuous crystallographic lattice shift due to the molecular intermixing of iminostilbene and phenothiazine. Also, if the crystalline phase can not be determined beforehand or multiple polymorphs (or pseudo-polymorphs such as solvates or hydrates) are likely to form, pole figure investigations become very time consuming. Thus, the presented method of reciprocal space mapping and pole figure reconstruction is well suited for screening large numbers of samples and films containing multiple polymorphs as demonstrated on the example of carbamazepine crystallites growing on top of iminostilbene crystals.

Bibliography

1. Erdemir, D., Lee, A. Y. & Myerson, A. S. Nucleation of crystals from solution: classical and two-step models. *Accounts of Chemical Research* **42**, 621–629 (2009).
2. Vekilov, P. G. Nucleation. *Crystal Growth & Design* **10**, 5007–5019 (2010).
3. Chen, J., Sarma, B., Evans, J. M. B. & Myerson, A. S. Pharmaceutical Crystallization. *Crystal Growth & Design* **11**, 887–895 (2011).
4. Myerson, A. *Handbook of Industrial Crystallization* Google-Books-ID: gJ7KNvbMtREC. 329 pp. (Butterworth-Heinemann, 2002).
5. Dimitrakopoulos, C. & Malenfant, P. Organic Thin Film Transistors for Large Area Electronics. *Advanced Materials* **14**, 99–117 (2002).
6. Peumans, P., Uchida, S. & Forrest, S. R. Efficient bulk heterojunction photovoltaic cells using small-molecular-weight organic thin films. *Nature* **425**, 158–162 (2003).
7. Jones, A. O. F., Chattopadhyay, B., Geerts, Y. H. & Resel, R. Substrate-Induced and Thin-Film Phases: Polymorphism of Organic Materials on Surfaces. *Advanced Functional Materials* **26**, 2233–2255 (2016).
8. Balzer, F., Bordo, V. G., Simonsen, A. C. & Rubahn, H.-G. Optical waveguiding in individual nanometer-scale organic fibers. *Physical Review B* **67**, 115408 (2003).
9. Liu, S., Wang, W. M., Briseno, A. L., Mannsfeld, S. C. B. & Bao, Z. Controlled Deposition of Crystalline Organic Semiconductors for Field-Effect-Transistor Applications. *Advanced Materials* **21**, 1217–1232 (2009).
10. Birkholz, M., Fewster, P. F. & Genzel, C. *Thin film analysis by X-ray scattering* (Wiley-VCH ; John Wiley, distributor], Weinheim; Chichester, 2006).
11. Neuschitzer, M., Moser, A., Neuhold, A., Kraxner, J., Stadlober, B., Oehzelt, M., Salzmann, I., Resel, R. & Novák, J. Grazing-incidence in-plane X-ray diffraction on ultra-thin organic films using standard laboratory equipment. *Journal of Applied Crystallography* **45**, 367–370 (2012).

12. Jones, A. O. F., Röthel, C., Lassnig, R., N. Bedoya-Martínez, O., Christian, P., Salzmänn, I., Kunert, B., Winkler, A. & Resel, R. Solution of an elusive pigment crystal structure from a thin film: a combined X-ray diffraction and computational study. *CrystEngComm* **19**, 1902–1911 (2017).
13. Lercher, C. *et al.* Polymorphism of dioctyl-terthiophene within thin films: The role of the first monolayer. *Chemical Physics Letters* **630**, 12–17 (2015).
14. Moser, A. *et al.* Crystal structure determination from two-dimensional powders: A combined experimental and theoretical approach. *The European Physical Journal Special Topics* **167**, 59–65 (2009).
15. Bennett, D. W. *Understanding single-crystal x-ray crystallography* (Wiley-VCH, Weinheim, 2010).
16. Warren, B. E. *X-Ray Diffraction* 381 pp. (Dover Publications, 2012).
17. Simbrunner, C. Epitaxial growth of sexi-thiophene and para-hexaphenyl and its implications for the fabrication of self-assembled lasing nano-fibres. *Semiconductor Science and Technology* **28**, 053001 (2013).
18. Salzmänn, I. & Resel, R. STEREOPOLE : software for the analysis of X-ray diffraction pole figures with IDL. *Journal of Applied Crystallography* **37**, 1029–1033 (2004).
19. Kriegner, D., Wintersberger, E. & Stangl, J. xrayutilities: A versatile tool for reciprocal space conversion of scattering data recorded with linear and area detectors. *Journal of Applied Crystallography* **46**, 1162–1170 (2013).
20. Röthel, C., Radziown, M., Resel, R., Zimmer, A., Simbrunner, C. & Werzer, O. Complex Behavior of Caffeine Crystallites on Muscovite Mica Surfaces. *Crystal Growth & Design* **15**, 4563–4570 (2015).
21. Kim, H., Gilmore, C. M., Piqué, A., Horwitz, J. S., Mattoussi, H., Murata, H., Kafafi, Z. H. & Chrisey, D. B. Electrical, optical, and structural properties of indium–tin–oxide thin films for organic light-emitting devices. *Journal of Applied Physics* **86**, 6451–6461 (1999).
22. Lassnig, R., Striedinger, B., Hollerer, M., Fian, A., Stadlober, B. & Winkler, A. In situ preparation, electrical and surface analytical characterization of pentacene thin film transistors. *Journal of Applied Physics* **116**, 114508 (2014).
23. Ehmann, H. M. A., Zimmer, A., Roblegg, E. & Werzer, O. Morphologies in Solvent-Annealed Clotrimazole Thin Films Explained by Hansen-Solubility Parameters. *Crystal Growth & Design* **14**, 1386–1391 (2014).
24. Virkar, A. A., Mannsfeld, S., Bao, Z. & Stingelin, N. Organic Semiconductor Growth and Morphology Considerations for Organic Thin-Film Transistors. *Advanced Materials* **22**, 3857–3875 (2010).

25. Simbrunner, C. *et al.* Organic–Organic Heteroepitaxy of Red-, Green-, and Blue-Emitting Nanofibers. *ACS Nano* **4**, 6244–6250 (2010).
26. Simbrunner, C. *et al.* Color Tuning of Nanofibers by Periodic Organic–Organic Hetero-Epitaxy. *ACS Nano* **6**, 4629–4638 (2012).
27. Musumeci, C., Salzmann, I., Bonacchi, S., Röthel, C., Duhm, S., Koch, N. & Samorì, P. The Relationship between Structural and Electrical Characteristics in Perylenecarboxydiimide-Based Nanoarchitectures. *Advanced Functional Materials* **25**, 2501–2510 (2015).
28. Tsoi, W. C. *et al.* Effect of Crystallization on the Electronic Energy Levels and Thin Film Morphology of P3HT:PCBM Blends. *Macromolecules* **44**, 2944–2952 (2011).
29. Hilfiker, R. *Polymorphism: In the Pharmaceutical Industry* 436 pp. (John Wiley & Sons, 2006).
30. Rodriguez-Spong, B., Price, C. P., Jayasankar, A., Matzger, A. J. & Rodriguez-Hornedo, N. General principles of pharmaceutical solid polymorphism: A supramolecular perspective. *Advanced Drug Delivery Reviews. Pharmaceutical solid polymorphism in drug development and regulation* **56**, 241–274 (2004).
31. Singhal, D. & Curatolo, W. Drug polymorphism and dosage form design: a practical perspective. *Advanced Drug Delivery Reviews. Pharmaceutical solid polymorphism in drug development and regulation* **56**, 335–347 (2004).
32. Baptiste, L., Landschoot, N. v., Gleijm, G., Priede, J., Schade van Westrum, J., Velthuis, H. & Kim, T.-Y. Electromagnetic levitation: A new technology for high rate physical vapour deposition of coatings onto metallic strip. *Surface and Coatings Technology. ICMCTF 2007 34th International Conference and Metallurgical Coatings and Thin Films (ICMCTF 2007)* **202**, 1189–1193 (2007).
33. *Springer Handbook of Nanotechnology* (ed Bhushan, B.) (Springer Berlin Heidelberg, Berlin, Heidelberg, 2010).
34. Jones, A. O. F., Geerts, Y. H., Karpinska, J., Kennedy, A. R., Resel, R., Röthel, C., Ruzié, C., Werzer, O. & Sferrazza, M. Substrate-Induced Phase of a [1]Benzothieno[3,2-b]benzothiophene Derivative and Phase Evolution by Aging and Solvent Vapor Annealing. *ACS Applied Materials & Interfaces* **7**, 1868–1873 (2015).
35. Simbrunner, C. *et al.* Epitaxial growth of sexithiophene on mica surfaces. *Physical Review B* **83**, 115443 (2011).

36. Ehmann, H. M. A. & Werzer, O. Surface Mediated Structures: Stabilization of Metastable Polymorphs on the Example of Paracetamol. *Crystal Growth & Design* **14**, 3680–3684 (2014).
37. Schiefer, S., Huth, M., Dobrinevski, A. & Nickel, B. Determination of the crystal structure of substrate-induced pentacene polymorphs in fiber structured thin films. *Journal of the American Chemical Society* **129**, 10316–10317 (2007).
38. Werzer, O., Matoy, K., Smilgies, D.-M., Rothmann, M. M., Strohrriegl, P. & Resel, R. Uniaxially aligned poly[(9,9-dioctylfluorenyl-2,7-diyl)-co-bithiophene] thin films characterized by the X-ray diffraction pole figure technique. *Journal of Applied Polymer Science* **107**, 1817–1821 (2008).
39. Giling, L. J. & Van Enckevort, W. J. P. On the influence of surface reconstruction on crystal growth processes. *Surface Science* **161**, 567–583 (1985).
40. Simbrunner, C. *et al.* Epitaxy of Rodlike Organic Molecules on Sheet Silicates - A Growth Model Based on Experiments and Simulations. *Journal of the American Chemical Society* **133**, 3056–3062 (2011).
41. Salzmann, I., Duhm, S., Opitz, R., Johnson, R. L., Rabe, J. P. & Koch, N. Structural and electronic properties of pentacene-fullerene heterojunctions. *Journal of Applied Physics* **104**, 114518 (2008).
42. Koch, N. Organic Electronic Devices and Their Functional Interfaces. *ChemPhysChem* **8**, 1438–1455 (2007).
43. Radziwon, M., Madsen, M., Balzer, F., Resel, R. & Rubahn, H.-G. Growth of alpha-sexithiophene nanostructures on C60 thin film layers. *Thin Solid Films* **558**, 165–169 (2014).
44. Gibson, M. *Pharmaceutical Preformulation and Formulation: A Practical Guide from Candidate Drug Selection to Commercial Dosage Form* 612 pp. (Taylor & Francis, 2001).
45. Trask, A. V. & Jones, W. in *Organic Solid State Reactions* (ed Toda, F.) *Topics in Current Chemistry* 254, 41–70 (Springer Berlin Heidelberg, 2005).
46. Cronstein, B. N. Caffeine, a drug for all seasons. *Journal of Hepatology* **53**, 207–208 (2010).
47. Sawynok, J. & Yaksh, T. L. Caffeine as an analgesic adjuvant: a review of pharmacology and mechanisms of action. *Pharmacological Reviews* **45**, 43–85 (1993).

48. Descamps, M., Correia, N. T., Derollez, P., Danede, F. & Capet, F. Plastic and glassy crystal states of caffeine. *The Journal of Physical Chemistry B* **109**, 16092–16098 (2005).
49. Sarfraz, A., Simo, A., Fenger, R., Christen, W., Rademann, K., Panne, U. & Emmerling, F. Morphological Diversity of Caffeine on Surfaces: Needles and Hexagons. *Crystal Growth & Design* **12**, 583–588 (2012).
50. Leiterer, J., Emmerling, F., Panne, U., Christen, W. & Rademann, K. Tracing Coffee Tabletop Traces. *Langmuir* **24**, 7970–7978 (2008).
51. Werzer, O., Kunert, B., Roblegg, E., Zimmer, A., Oehzelt, M. & Resel, R. Surface Induced Order of Solution Processed Caffeine Needles on Silica and Muscovite Mica. *Crystal Growth & Design* **13**, 1322–1328 (2013).
52. Mattox, D. M. *Handbook of Physical Vapor Deposition (PVD) Processing* 793 pp. (William Andrew, 2010).
53. Lopez-Otero, A. Hot wall epitaxy. *Thin Solid Films* **49**, 3–57 (1978).
54. Sitter, H., Andreev, A., Matt, G. & Sariciftci, N. S. Hot-wall-epitaxy-the method of choice for the growth of highly ordered organic epilayers. *Molecular Crystals and Liquid Crystals* **385**, 51–60 (2002).
55. Schulz, L. G. A Direct Method of Determining Preferred Orientation of a Flat Reflection Sample Using a Geiger Counter X-Ray Spectrometer. *Journal of Applied Physics* **20**, 1030–1033 (1949).
56. Nečas, D. & Klapetek, P. Gwyddion: an open-source software for SPM data analysis. *Central European Journal of Physics* **10**, 181–188 (2011).
57. Lehmann, C. W. & Stowasser, F. The Crystal Structure of Anhydrous beta-Caffeine as Determined from X-ray Powder-Diffraction Data. *Chemistry – A European Journal* **13**, 2908–2911 (2007).
58. Enright, G. D., Terskikh, V. V., Brouwer, D. H. & Ripmeester, J. A. The Structure of Two Anhydrous Polymorphs of Caffeine from Single-Crystal Diffraction and Ultrahigh-Field Solid-State ¹³C NMR Spectroscopy. *Crystal Growth & Design* **7**, 1406–1410 (2007).
59. Hedoux, A., Decroix, A.-A., Guinet, Y., Paccou, L., Derollez, P. & Descamps, M. Low- and High-Frequency Raman Investigations on Caffeine: Polymorphism, Disorder and Phase Transformation. *The Journal of Physical Chemistry B* **115**, 5746–5753 (2011).
60. Hedoux, A., Guinet, Y., Paccou, L., Danede, F. & Derollez, P. Polymorphic transformation of anhydrous caffeine upon grinding and hydrostatic pressurizing analyzed by low-frequency raman spectroscopy. *Journal of Pharmaceutical Sciences* **102**, 162–170 (2013).

61. Kuwahara, Y. Comparison of the surface structure of the tetrahedral sheets of muscovite and phlogopite by AFM. *Physics and Chemistry of Minerals* **28**, 1–8 (2001).
62. Potocar, T. *et al.* Initial stages of a para-hexaphenyl film growth on amorphous mica. *Physical Review B* **83**, 075423 (2011).
63. Röthel, C., Radziown, M., Resel, R., Grois, A., Simbrunner, C. & Werzer, O. Crystal alignment of caffeine deposited onto single crystal surfaces via hot-wall epitaxy. *CrystEngComm*. doi:10.1039/C7CE00515F (2017).
64. Mannsfeld, S. C. B., Virkar, A., Reese, C., Toney, M. F. & Bao, Z. Precise Structure of Pentacene Monolayers on Amorphous Silicon Oxide and Relation to Charge Transport. *Advanced Materials* **21**, 2294–2298 (2009).
65. Briseno, A. L. *et al.* Patterning organic single-crystal transistor arrays. *Nature* **444**, 913–917 (2006).
66. Yanagi, H., Morikawa, T., Hotta, S. & Yase, K. Epitaxial Growth of Thiophene/p-Phenylene Co-oligomers for Highly Polarized Light-Emitting Crystals. *Advanced Materials* **13**, 313–317 (2001).
67. Curcio, E., Curcio, V., Profio, G. D., Fontananova, E. & Drioli, E. Energetics of Protein Nucleation on Rough Polymeric Surfaces. *The Journal of Physical Chemistry B* **114**, 13650–13655 (2010).
68. Ward, M. D. Bulk Crystals to Surfaces: Combining X-ray Diffraction and Atomic Force Microscopy to Probe the Structure and Formation of Crystal Interfaces. *Chemical Reviews* **101**, 1697–1726 (2001).
69. Beiner, M., Rengarajan, G. T., Pankaj, S., Enke, D. & Steinhart, M. Manipulating the Crystalline State of Pharmaceuticals by Nanoconfinement. *Nano Letters* **7**, 1381–1385 (2007).
70. Resel, R., Ottmar, M., Hanack, M., Keckes, J. & Leising, G. Preferred Orientation of Copper Phthalocyanine Thin Films Evaporated on Amorphous Substrates. *Journal of Materials Research* **15**, 934–939 (2000).
71. Diao, Y., Myerson, A. S., Hatton, T. A. & Trout, B. L. Surface Design for Controlled Crystallization: The Role of Surface Chemistry and Nanoscale Pores in Heterogeneous Nucleation. *Langmuir* **27**, 5324–5334 (2011).
72. Diao, Y., Harada, T., Myerson, A. S., Hatton, T. A. & Trout, B. L. The role of nanopore shape in surface-induced crystallization. *Nature Materials* **10**, 867–871 (2011).
73. Fritz, S. E., Kelley, T. W. & Frisbie, C. D. Effect of Dielectric Roughness on Performance of Pentacene TFTs and Restoration of Performance with a Polymeric Smoothing Layer. *The Journal of Physical Chemistry B* **109**, 10574–10577 (2005).

74. Zheng, Z., Yim, K.-H., Saifullah, M. S. M., Welland, M. E., Friend, R. H., Kim, J.-S. & Huck, W. T. S. Uniaxial Alignment of Liquid-Crystalline Conjugated Polymers by Nanoconfinement. *Nano Letters* **7**, 987–992 (2007).
75. Cavallini, M. *et al.* Field-Effect Transistors Based on Self-Organized Molecular Nanostripes. *Nano Letters* **5**, 2422–2425 (2005).
76. Hooks, D. E., Fritz, T. & Ward, M. D. Epitaxy and Molecular Organization on Solid Substrates. *Advanced Materials* **13**, 227–241 (2001).
77. Mizuno, H., Ohnishi, I., Yanagi, H., Sasaki, F. & Hotta, S. Lasing from Epitaxially Oriented Needle Crystals of a Thiophene/Phenylene Co-Oligomer. *Advanced Materials* **24**, 2404–2408 (2012).
78. Balzer, F. & Rubahn, H.-G. Growth Control and Optics of Organic Nanoaggregates. *Advanced Functional Materials* **15**, 17–24 (2005).
79. Schwabegger, G., Djuric, T., Sitter, H., Resel, R. & Simbrunner, C. Morphological and Structural Investigation of Sexithiophene Growth on KCl (100). *Crystal Growth & Design* **13**, 536–542 (2013).
80. Möbus, M., Karl, N. & Kobayashi, T. Structure of perylene-tetracarboxylic-dianhydride thin films on alkali halide crystal substrates. *Journal of Crystal Growth* **116**, 495–504 (1992).
81. Karl, N. Charge carrier transport in organic semiconductors. *Synthetic Metals. Proceedings of the Yamada Conference LVI. The Fourth International Symposium on Crystalline Organic Metals, Superconductors and Ferromagnets (ISCOM 2001)*. **133–134**, 649–657 (2003).
82. Joseph Kline, R., McGehee, M. D. & Toney, M. F. Highly oriented crystals at the buried interface in polythiophene thin-film transistors. *Nature Materials* **5**, 222–228 (2006).
83. Bučar, D.-K., Day, G. M., Halasz, I., Zhang, G. G. Z., Sander, J. R. G., Reid, D. G., MacGillivray, L. R., Duer, M. J. & Jones, W. The curious case of (caffeine)·(benzoic acid): how heteronuclear seeding allowed the formation of an elusive cocrystal. *Chemical Science* **4**, 4417–4425 (2013).
84. Mitchell, C. A., Yu, L. & Ward, M. D. Selective Nucleation and Discovery of Organic Polymorphs through Epitaxy with Single Crystal Substrates. *Journal of the American Chemical Society* **123**, 10830–10839 (2001).
85. Chadwick, K., Myerson, A. & Trout, B. Polymorphic control by heterogeneous nucleation - A new method for selecting crystalline substrates. *CrystEngComm* **13**, 6625–6627 (2011).
86. Arlin, J.-B., Price, L. S., Price, S. L. & Florence, A. J. A strategy for producing predicted polymorphs: catemeric carbamazepine form V. *Chemical Communications* **47**, 7074–7076 (2011).

87. Srirambhatla, V. K., Guo, R., Price, S. L. & Florence, A. J. Isomorphous template induced crystallisation: a robust method for the targeted crystallisation of computationally predicted metastable polymorphs. *Chemical Communications (Cambridge, England)* **52**, 7384–7386 (2016).
88. Seliger, J., Žagar, V., Apih, T., Gregorovič, A., Latosińska, M., Olejniczak, G. A. & Latosińska, J. N. Polymorphism and disorder in natural active ingredients. Low and high-temperature phases of anhydrous caffeine: Spectroscopic (^1H – ^{14}N NMR–NQR/ ^{14}N NQR) and solid-state computational modelling (DFT/QTAIM/RDS) study. *European Journal of Pharmaceutical Sciences* **85**, 18–30 (2016).
89. Muccioli, L., D’Avino, G. & Zannoni, C. Simulation of Vapor-Phase Deposition and Growth of a Pentacene Thin Film on C60 (001). *Advanced Materials* **23**, 4532–4536 (2011).
90. Barth, J. V., Costantini, G. & Kern, K. Engineering atomic and molecular nanostructures at surfaces. *Nature* **437**, 671–679 (2005).
91. Resel, R., Haber, T., Lengyel, O., Sitter, H., Balzer, F. & Rubahn, H.-G. Origins for epitaxial order of sexiphenyl crystals on muscovite(001). *Surface and Interface Analysis* **41**, 764–770 (2009).
92. Bonafede, S. J. & Ward, M. D. Selective Nucleation and Growth of an Organic Polymorph by Ledge-Directed Epitaxy on a Molecular Crystal Substrate. *Journal of the American Chemical Society* **117**, 7853–7861 (1995).
93. Haber, T. *et al.* Single Crystalline Nature of para-Sexiphenyl Crystallites Grown on KCl(100). *Journal of Nanoscience and Nanotechnology* **6**, 698–703 (2006).
94. Hulliger, J., Roth, S. W., Quintel, A. & Bebie, H. Polarity of Organic Supramolecular Materials: A Tunable Crystal Property. *Journal of Solid State Chemistry* **152**, 49–56 (2000).
95. Ginsburg, G. S. & McCarthy, J. J. Personalized medicine: revolutionizing drug discovery and patient care. *Trends in Biotechnology* **19**, 491–496 (2001).
96. Lin, Z.-G., Tang, L.-C. & Chou, C.-P. Characterization and Properties of Novel Infrared Nonlinear Optical Crystal CsGe(BrxCl $_{1-x}$) $_3$. *Inorganic Chemistry* **47**, 2362–2367 (2008).
97. Blagden, N., de Matas, M., Gavan, P. T. & York, P. Crystal engineering of active pharmaceutical ingredients to improve solubility and dissolution rates. *Advanced Drug Delivery Reviews. Drug Solubility: How to Measure it, How to Improve it* **59**, 617–630 (2007).

98. Hiszpanski, A. M., Baur, R. M., Kim, B., Tremblay, N. J., Nuckolls, C., Woll, A. R. & Loo, Y.-L. Tuning Polymorphism and Orientation in Organic Semiconductor Thin Films via Post-deposition Processing. *Journal of the American Chemical Society* **136**, 15749–15756 (2014).
99. Price, S. L. Computed Crystal Energy Landscapes for Understanding and Predicting Organic Crystal Structures and Polymorphism. *Accounts of Chemical Research* **42**, 117–126 (2009).
100. Blagden, N. & Davey, R. J. Polymorph Selection: Challenges for the Future? *Crystal Growth & Design* **3**, 873–885 (2003).
101. Schultheiss, N. & Newman, A. Pharmaceutical Cocrystals and Their Physicochemical Properties. *Crystal Growth & Design* **9**, 2950–2967 (2009).
102. Méndez, H. *et al.* Doping of Organic Semiconductors: Impact of Dopant Strength and Electronic Coupling. *Angewandte Chemie International Edition* **52**, 7751–7755 (2013).
103. Vogel, J.-O., Salzmann, I., Duhm, S., Oehzelt, M., P. Rabe, J. & Koch, N. Phase -separation and mixing in thin films of co-deposited rod-like conjugated molecules. *Journal of Materials Chemistry* **20**, 4055–4066 (2010).
104. Kitaigorodsky, A. I. *Mixed Crystals* Google-Books-ID: LmDsCAAAQBAJ. 403 pp. (Springer Science & Business Media, 2012).
105. Schur, E., Nauha, E., Lusi, M. & Bernstein, J. Kitaigorodsky revisited: polymorphism and mixed crystals of acridine/phenazine. *Chemistry (Weinheim an Der Bergstrasse, Germany)* **21**, 1735–1742 (2015).
106. Lusi, M., Vitorica-Yrezabal, I. J. & Zaworotko, M. J. Expanding the Scope of Molecular Mixed Crystals Enabled by Three Component Solid Solutions. *Crystal Growth & Design* **15**, 4098–4103 (2015).
107. Nie, Q., Gong, J. B., Wang, J. K. & Wang, S. Formation of Mixed Crystals in Crystallization of 11 α -Hydroxy-16 α ,17 α -epoxyprogesterone and 16 α ,17 α -Epoxyprogesterone. *Industrial & Engineering Chemistry Research* **45**, 432–437 (2006).
108. Hinderhofer, A. & Schreiber, F. Organic–Organic Heterostructures: Concepts and Applications. *ChemPhysChem* **13**, 628–643 (2012).
109. Denton, A. R. & Ashcroft, N. W. Vegard’s law. *Physical Review A* **43**, 3161–3164 (1991).
110. Ward, M. D. Linear chain organometallic donor-acceptor complexes and one-dimensional alloys. *Organometallics* **6**, 754–762 (1987).

111. Morimoto, M., Kobatake, S. & Irie, M. Multicolor Photochromism of Two- and Three-Component Diarylethene Crystals. *Journal of the American Chemical Society* **125**, 11080–11087 (2003).
112. Lausi, A. *et al.* Status of the crystallography beamlines at Elettra. *The European Physical Journal Plus* **130**, 43 (2015).
113. Kabsch, W. XDS. *Acta Crystallographica Section D: Biological Crystallography* **66**, 125–132 (2010).
114. Winn, M. D. *et al.* Overview of the CCP4 suite and current developments. *Acta Crystallographica. Section D, Biological Crystallography* **67**, 235–242 (Pt 4 2011).
115. Evans, P. R. & Murshudov, G. N. How good are my data and what is the resolution? *Acta Crystallographica Section D: Biological Crystallography* **69**, 1204–1214 (Pt 7 2013).
116. Sheldrick, G. M. SHELXT – Integrated space-group and crystal-structure determination. *Acta Crystallographica Section A: Foundations and Advances* **71**, 3–8 (2015).
117. Sheldrick, G. M. Crystal structure refinement with SHELXL. *Acta Crystallographica. Section C, Structural Chemistry* **71**, 3–8 (Pt 1 2015).
118. Emsley, P. & Cowtan, K. Coot: model-building tools for molecular graphics. *Acta Crystallographica. Section D, Biological Crystallography* **60**, 2126–2132 (Pt 12 Pt 1 2004).
119. Kitaigorodskii, A. I. The principle of close packing and the condition of thermodynamic stability of organic crystals. *Acta Crystallographica* **18**, 585–590 (1965).
120. Méndez, H. *et al.* Charge-transfer crystallites as molecular electrical dopants. *Nature Communications* **6**, ncomms9560 (2015).
121. Christian, P., Röthel, C., Tazreiter, M., Zimmer, A., Salzmann, I., Resel, R. & Werzer, O. Crystallization of Carbamazepine in Proximity to Its Precursor Iminostilbene and a Silica Surface. *Crystal Growth & Design* **16**, 2771–2778 (2016).
122. Roseboom, H. & Perrin, J. H. Mechanism for Phenothiazine Oxidation. *Journal of Pharmaceutical Sciences* **66**, 1395–1398 (1977).

Place and Date of Birth: Graz, December 1987

Address: Birkengasse 14, 8190 Birkfeld, Austria

Email: ch.roethel@gmail.com

Phone: +43 664 4239046

EDUCATION

Doctoral Programme Technical Physics (since Oct 2014 – 2017 expected)

Institute of Solid State Physics, Graz University of Technology, Austria

Institute of Pharmaceutical Sciences, University of Graz, Austria

Topic: **Surface crystallization and structural analysis of pharmaceutical drug molecules**

Supervisor: Dr. Oliver Werzer and Prof. Roland Resel

Master of Science in Technical Physics (with distinction) (Oct 2011 – May 2014)

Graz University of Technology, Austria

Master's Thesis: **"Thin Film Crystal Structure Solution by Combining Molecular Dynamics and X-ray Diffraction"** (Institute of Solid State Physics)

Supervisor: Prof. Roland Resel

Bachelor of Science in Technical Physics (Oct 2008 – Aug 2011)

Graz University of Technology, Austria

Bachelor's Thesis: **"Fitting Line Shapes of X-ray Powder Diffraction Peaks"**

Supervisor: Prof. Roland Resel

Computer Science (Mar 2008 – Jan 2009)

Graz University of Technology, Austria

Military Service (Jul 2007 – Jan 2008)

Austrian Armed Forces, Von-der-Groeben-Kaserne, Feldbach, Austria

Reife- und Diplomprüfung (with distinction) (Jun 2007)

Höhere Technische Bundeslehranstalt (Federal Higher Technical Institute), Weiz

Specialisation: Electrical Engineering and Information Technology

Final Year Project: Process Monitoring Tool for Windows XP

RESEARCH EXPERIENCE

- X-ray diffraction with focus on surface diffraction of organic thin films (grazing incidence, reflectivity, pole figures)
- Crystal growth of organic molecules on surfaces and crystal structure solution of thin films
- Several synchrotron experiments at ESRF (Grenoble, France), BESSY (Berlin, Germany), ELETTRA (Trieste, Italy) and DIAMOND (Harwell, UK).
- Molecular dynamics simulations and density functional theory (DFT) calculations of organic molecules

TECHNICAL SKILLS

- Highly experienced in the evaluation of X-ray diffraction data, especially of synchrotron experiments (2D detector calibration, reciprocal space conversion)
- Proficient in MATLAB (data evaluation, visualization and simulation)
- Extensive knowledge in programming (C/C++, C# and similar languages)
- Comprehensive understanding of computer hardware and electronics

PROFESSIONAL EXPERIENCE

University of Graz (since Oct 2014 – Jul 2017)

Institute of Pharmaceutical Sciences - Department of Pharmaceutical Technology
Doctoral research assistant - FWF project: Surface induced phases of pharmaceutical molecules

Graz University of Technology (Jul 2014 – Oct 2014)

Institute of Solid State Physics - Research assistant

Graz University of Technology (Oct 2011 – Jan 2014)

Teaching Assistant – Physics Lab Course
Supervising and grading first and second year undergraduate students in a physics lab course containing experiments on optics, mechanics, heat and electricity

Siemens Transformers Austria Weiz (summer job, 2006, 2010, 2011)

Hands-on experience in wiring and installation of control units for large-scale power transformers

PUBLICATIONS/TALKS/POSTER

Publications:

- C. Röthel, M. Radziwon, R. Resel, A. Zimmer, C. Simbrunner, and O. Werzer, **‘Complex Behavior of Caffeine Crystallites on Muscovite Mica Surfaces’**, Crystal Growth & Design, 2015.
- C. Röthel, M. Radziwon, R. Resel, A. Grois, C. Simbrunner, and O. Werzer. **‘Crystal alignment of caffeine deposited onto single crystal surfaces via hot-wall epitaxy’**, CrystEngComm, 2017.
- H. Méndez, G. Heimel, S. Winkler, J. Frisch, A. Opitz, K. Sauer, B. Wegner, M. Oehzelt, C. Röthel, S. Duhm, D. Többens, N. Koch, and I. Salzmann, **‘Charge-transfer crystallites as molecular electrical dopants’**, Nature communications, 2015.
- C. Röthel, H. M. A. Ehmann, R. Baumgartner, D. Reischl, and Oliver Werzer, **‘Alteration of Texture and Polymorph of Phenytoin within Thin Films and its Impact on Dissolution’**, CrystEngComm, 2016.

- A. O. F. Jones, C. Röthel, R. Lassnig, O. N. Bedoya-Martínez, P. Christian, I. Salzmänn, B. Kunert, A. Winkler, and R. Resel, **‘Solution of an elusive pigment crystal structure from a thin film: a combined X-ray diffraction and computational study’**, CrystEngComm, 2017.
- P. Christian, C. Röthel, M. Tazreiter, A. Zimmer, I. Salzmänn, R. Resel, and O. Werzer, **‘Crystallization of Carbamazepine in Proximity to Its Precursor Iminostilbene and a Silica Surface’**, Crystal Growth & Design, 2016.
- S. Pachmajer, A. O. F. Jones, M. Truger, C. Röthel, I. Salzmänn, O. Werzer, and R. Resel, **‘Self-Limited Growth in Pentacene Thin Films’**, ACS Applied Materials & Interfaces, 2017.
- D. Reischl, C. Röthel, P. Christian, E. Roblegg, H. M. A. Ehmann, I. Salzmänn, and O. Werzer, **‘Surface-Induced Polymorphism as a Tool for Enhanced Dissolution: The Example of Phenytoin’**, Crystal Growth & Design, 2015.
- A. O. Jones, Y. H. Geerts, J. Karpinska, A. R. Kennedy, R. Resel, C. Röthel, C. Ruzié, O. Werzer, and M. Sferrazza, **‘Substrate-Induced Phase of a [1] Benzothieno [3, 2-b] benzothiophene Derivative and Phase Evolution by Aging and Solvent Vapor Annealing’**, ACS Applied Materials & Interfaces, 2015.
- F. Balzer, C. Röthel, H.-G. Rubahn, A. Lützen, J. Parisi, R. Resel, and M. Schiek, **‘Thin Film Phase and Local Chirality of Surface-Bound MOP4 Nanofibers’**, The Journal of Physical Chemistry C, 2016.
- M. Truger, O. M. Roscioni, C. Röthel, D. Kriegner, C. Simbrunner, R. Ahmed, E. D. Glowacki, J. Simbrunner, I. Salzmänn, A. M. Coclite, A. O. F. Jones, and R. Resel, **‘Surface-Induced Phase of Tyrian Purple (6, 6'-Dibromoindigo): Thin Film Formation and Stability’**, Crystal Growth & Design, 2016.
- M. Truger, A. O. F. Jones, A. M. Coclite, S. Pachmajer, D. Kriegner, C. Röthel, J. Simbrunner, I. Salzmänn, R. Resel, **‘Crystallization of Tyrian purple (6, 6'-dibromoindigo) thin films: The impact of substrate surface modifications’**, Journal of Crystal Growth, 2016.
- C. Musumeci, I. Salzmänn, S. Bonacchi, C. Röthel, S. Duhm, N. Koch, and P. Samorì, **‘The Relationship between Structural and Electrical Characteristics in Perylenecarboxydiimide-Based Nanoarchitectures’**, Advanced Functional Materials, 2015.
- B. R. Scherwitzl, C. Röthel, A. O. F. Jones, B. Kunert, I. Salzmänn, R. Resel, G. Leising, and A. Winkler, **‘Idiosyncrasies of Physical Vapor Deposition Processes from Various Knudsen Cells for Quinacridone Thin Film Growth on Silicon Dioxide’**, Journal of Physical Chemistry C, 2015.
- O. Kettner, A. Pein, G. Trimmel, P. Christian, C. Röthel, I. Salzmänn, R. Resel, G. Lakhwani, F. Lombeck, M. Sommer, and B. Friedel, **‘Mixed side-chain geometries for aggregation control of poly (fluorene-alt-bithiophene) and their effects on photophysics and charge transport’**, Synthetic Metals, 2016.

- C. Lercher, C. Röthel, O. M. Roscioni, Y. H. Geerts, Q. Shen, C. Teichert, R. Fischer, G. Leising, M. Sferrazza, G. Gbabode, and R. Resel, , **'Polymorphism of Dioctyl-Terthiophene within Thin Films: The Role of the First Monolayer'**, Chemical Physics Letters, 2015.

Talks:

- **Solution of Unknown Crystal Structures (from Thin Films).** XRM Workshop 2016, University Twente, The Netherlands, (Sept 2016)
- **Complex Behaviour of Caffeine Crystallites on Muscovite Mica Surfaces,** Solid State Institute Seminar, Graz University of Technology, Austria, (Nov 2015)
- **Crystal Structure Solution of Thin Films,** Nanoforum 2014, Johannes Kepler University Linz, Austria, (Jun 2014)
- **Thin Film Crystal Structure Solution Using Molecular Dynamics,** VIth Workshop on Substrate-induced Crystal Structures, Université de Rouen, France, (May 2014)

Posters:

- **Mixing Organic Molecules: From Epitaxy to Tuneable Crystal Lattices.** XRM Workshop 2016, University Twente, The Netherlands, (Sept 2016)
- **Complex Behaviour of Caffeine on Solid Surfaces.** 7th School on Organic Electronics, Lake Como School of Advanced Studies, Como, Italy, (Sept 2015)
- **Oriented crystal growth from solution: Iminostilbene and its derivative Carbamazepine.** Solvay Workshop on Directional Nucleation and Growth of Molecular Crystals, Université libre de Bruxelles, Belgium, (Dec 2014)

GRANTS

- Research grant for Master's Thesis: Graz University of Technology (2013)
- Scholarship for Excellence: Graz University of Technology (2009)
- Magna Scholarship for Excellence (2007)